

**Higgs Boson Discovery and First Property Measurements
using the ATLAS Detector**

by

Sven Kreiss

A dissertation submitted in partial fulfillment
of the requirements for the degree of

Doctor of Philosophy

Department of Physics

New York University

May 2014

Professor Kyle Cranmer

Acknowledgements

Thanks Kyle.

I would also like to thank the members of my thesis committee Andy Haas, David Hogg, Allen Mincer and Neal Weiner.

Abstract

Details of the discovery of a Higgs boson and its mass and coupling measurements using up to 25 fb^{-1} of collision data collected with the ATLAS detector at the LHC are presented. The measured mass is $m_H = 125.5 \pm 0.2(\text{stat})^{+0.5}_{-0.6}(\text{sys})$ using the $H \rightarrow \gamma\gamma$ and $H \rightarrow ZZ^* \rightarrow 4\ell$ channels. A combination of $H \rightarrow \gamma\gamma$, $H \rightarrow ZZ^* \rightarrow 4\ell$, $H \rightarrow WW^* \rightarrow \ell\nu\ell\nu$, $H \rightarrow \tau\tau$ and $H \rightarrow b\bar{b}$ yields an observed signal strength with respect to the Standard Model prediction of $\mu = 1.30 \pm 0.12(\text{stat})^{+0.14}_{-0.11}(\text{sys})$ at a Higgs boson mass of 125.5 GeV. The evidence for Higgs boson production through Vector Boson Fusion is confirmed at the 4.1σ level. The coupling to fermions is established at the 3.7σ level with a fermionic signal strength $\mu^{\tau\tau,bb} = 1.09 \pm 0.24(\text{stat})^{+0.27}_{-0.21}(\text{sys})$. Couplings of the Higgs boson to other particles are explored under a set of benchmark scenarios where no deviation from the Standard Model was found.

Modeling and statistics techniques are discussed thoroughly throughout. The channel $H \rightarrow ZZ^* \rightarrow 4\ell$ is described in detail with special attention on contributions to background estimates from objects that are falsely identified as leptons. A novel technique for the interpolation of outputs from large simulations using k-d trees, B-splines and kernel density estimates for the mass measurement in high resolution channels is presented. For the presentation of future results, it is desirable to factor out theoretical uncertainties. A framework for the construction of effective likelihoods without theoretical uncertainties and for deriving physics results from those is explained in detail.

Contents

Acknowledgements	iii
Abstract	iv
List of Figures	vii
List of Tables	xiii
1 Introduction	1
1.1 Higgs bosons at the LHC	4
1.2 The ATLAS Detector	7
1.3 The Trigger and Data Acquisition	16
1.4 Data Sample	20
1.5 Statistical Modeling	20
2 $H \rightarrow ZZ^* \rightarrow 4\ell$ Analysis	25
2.1 Simulation	26
2.2 Analysis Overview	30
2.3 Estimating Fake Rates	40
2.4 Systematic Uncertainties	48
2.5 $H \rightarrow ZZ^* \rightarrow 4\ell$ Signal Modeling	51

3 Discovery	61
3.1 Statistical Methods	61
3.2 $H \rightarrow \gamma\gamma$	63
3.3 $H \rightarrow WW^* \rightarrow \ell\nu\ell\nu$	70
3.4 Combination	76
3.5 Bayesian Checks on Limits	80
3.6 Latest Results from $H \rightarrow ZZ^* \rightarrow 4\ell$	83
4 Mass Measurement	85
4.1 Combined Mass	87
4.2 $H \rightarrow ZZ^* \rightarrow 4\ell$ and $H \rightarrow \gamma\gamma$ Mass Compatibility	90
5 Coupling Measurements	95
5.1 Cross Sections and Branching Ratios	97
5.2 Testing the Standard Model Hypothesis: Benchmark Models	103
5.3 Studies using Bayesian Techniques	107
5.4 Factorizing Theory Uncertainties	111
6 Conclusion	118
Bibliography	120

List of Figures

1.1	Higgs boson production modes at the LHC. Panel (a) shows the leading order Feynman diagram for gluon-fusion (ggF), (b) for vector boson fusion (VBF), (c) for associated production with a weak boson (VH) and (d) for associated production with top quarks ($t\bar{t}H$).	5
1.2	Higgs cross sections (a) and branching ratios (b) for various production modes and final states [1].	6
1.3	Theoretical calculations for $\sigma \times BR$ are shown in (a) and expected upper limits representing the statistical power of the analysis are shown in (b).	7
1.4	Overview of the ATLAS detector [2].	8
1.5	Inner detector perspective layout [3].	10
1.6	Inner detector: Pixel [4].	12
1.7	Liquid argon pulse shape [5].	13
1.8	Barrel toroid magnets [6].	15
1.9	Muon system schematic [7].	17
1.10	Particle identification [8].	18
1.11	ATLAS Trigger and data acquisition schematic [9].	19

1.12 Integrated luminosity for 2011 and 2012 data taking is shown in (a)
next to the mean number of interaction per bunch crossing in (b).
The data taking efficiency for the two years is shown in (c) and (d). 21

2.1	$H \rightarrow ZZ^* \rightarrow 4\ell$ control region (1). (a) shows the 4μ and (b) the $2e2\mu$ final state. The functional form that is fitted is a second order Chebyshev polynomial for the flat $t\bar{t}$ background and a Breit-Wigner for the peaked $Z + jets$ component convoluted with a Crystal-Ball function [10].	38
2.2	Invariant mass distributions for leading and sub-leading leptons pairs in the control region defined by a lepton pair forming a Z boson and a same-flavor lepton pair that can be both same-sign or opposite-sign.	39
2.3	Event selection results for $H \rightarrow ZZ^* \rightarrow 4\ell$ [10].	42
2.4	Estimated fake factors FR.	45
2.5	Monte Carlo estimates of $m_{3\text{-lepton}}$ spectrum.	47
2.6	Data-driven estimates of $m_{3\text{-lepton}}$ spectrum.	47
2.7	Monte Carlo (left) and data-driven (right) estimates of $m_{4\text{-lepton}}$ spectrum.	48
2.8	Comparison of (a) vertical and (b) horizontal interpolation for peaked shapes using a toy model. The dotted graphs are inputs and the solid graphs are outputs of the interpolation. The shapes are normalized to one.	51
2.9	B-spline interpolations for (a) the expected number of events and (b) systematic uncertainties in m_H . Input values were determined from MC samples with full detector simulations at fixed values of m_H	54

2.10	Effect of changing an energy scale on the shape of the $4e$ distribution in m_{4l} in arbitrary units.	55
2.11	Third order B-spline basis functions that are used as weights.	56
2.12	(a) Verification of the method. (b) Scan across m_H . Both plots are in arbitrary units.	57
2.13	Improvements in the final result due to the new signal model (red) over the old signal model (blue) for (a) the mass measurement, (b) the confidence intervals in the (μ, m_H) plane and (c) the lo- cal p_0 values.	60
3.1	MC studies for $H \rightarrow \gamma\gamma$ at (a) $\sqrt{s} = 7$ TeV and (b) $\sqrt{s} = 8$ TeV. . .	64
3.2	Invariant mass spectrum of $m_{\gamma\gamma}$ in $H \rightarrow \gamma\gamma$ decays.	69
3.3	Transverse mass spectrum for $H \rightarrow WW^* \rightarrow e\nu\mu\nu$ and $H \rightarrow WW^* \rightarrow \mu\nu e\nu$ decays for the 0-jet and 1-jet category.	75
3.4	Exclusion ranges from the combination in July 2012. (a) shows the excluded signal strength at 95% CL as a function of m_H and (b) shows the CL to exclude a signal strength of $\mu = 1$ as a function of m_H	78
3.5	Local p_0 values for the channels (a) $H \rightarrow ZZ^* \rightarrow 4\ell$, (b) $H \rightarrow \gamma\gamma$ and (c) $H \rightarrow WW^* \rightarrow \ell\nu\ell\nu$	79
3.6	Combination results.	80
3.7	Local p_0 values for an earlier combination that shows the explicit tests of the asymptotic equations with pseudo-experiments on a model with uncertainties on energy scale systematics.	81
3.8	Signal strengths measurements in the combination (a) across the full parameter range and (b) broken down by channel.	81

3.9	MULTINEST checks on upper limits with $1.1 - 4.9 \text{ fb}^{-1}$ of integrated luminosity at $\sqrt{s} = 7 \text{ TeV}$ for (a) individual decay channels and (b) the combination of those channels. The MULTINEST results and the results from asymptotic calculations are shown.	82
3.10	Checks using MCMC on the combined upper limit from asymptotic calculations.	83
3.11	Scan of the (a) p_0 values and (b) upper limits across m_H hypotheses.	84
4.1	Likelihood contours in the (μ, m_H) plane.	86
4.2	Comparison of likelihood contours in the (μ, m_H) plane with and without ESS uncertainties [11].	87
4.3	Likelihood contours in (μ, m_H) for (a) $H \rightarrow ZZ^* \rightarrow 4\ell$ and (b) $H \rightarrow \gamma\gamma$ with and without ESS uncertainties.	88
4.4	Likelihood curves in m_H for (a) $H \rightarrow ZZ^* \rightarrow 4\ell$ and (b) $H \rightarrow \gamma\gamma$	89
4.5	First likelihood curves $-2 \ln \lambda(m_H)$ for channels with μ profiled with (solid) and without (dashed) ESS uncertainties [11].	89
4.6	$H \rightarrow ZZ^* \rightarrow 4\ell$ mass measurement [10].	91
4.7	Latest combined Higgs boson mass measurement.	91
4.8	Illustrating the model to test the Higgs mass compatibility between the $H \rightarrow \gamma\gamma$ and $H \rightarrow ZZ^* \rightarrow 4\ell$ measurements. The best fit points in $(m_H^{4\ell}, m_H^{\gamma\gamma})$ are shown for the scenarios with a common signal strength (gray solid, star) and separate signal strengths $\mu^{\gamma\gamma}$ and $\mu^{4\ell}$ (gray dashed, triangle) [11].	92
4.9	Scans of likelihoods along the dashed diagonal in figure 4.8.	93
4.10	Latest results of the mass compatibility between the $H \rightarrow ZZ^* \rightarrow 4\ell$ channel and the $H \rightarrow \gamma\gamma$ channel.	94

5.1	Likelihood contours for $H \rightarrow \gamma\gamma$, $H \rightarrow ZZ^* \rightarrow 4\ell$, $H \rightarrow WW^* \rightarrow \ell\nu\ell\nu$ and $H \rightarrow \tau\tau$ in the production times branching ratio planes ($\mu_{ggF+ttH} \times B/B_{SM}$, $\mu_{VBF+VH} \times B/B_{SM}$)	98
5.2	The ratio of the signal strength for processes dominated by gauge boson couplings, VBF and VH, over the signal strength for processes dominated by the top coupling, ggF and $t\bar{t}H$	99
5.3	The ratio of the signal strength for the VBF process over the signal strength for ggF and $t\bar{t}H$ while profiling the signal strength for VH. It shows evidence for VBF production.	101
5.4	Measurements of the ratios of branching ratios ρ	102
5.5	The (κ_V, κ_F) benchmark model. (a) shows likelihood contours for the combination of all channels and (b) shows contours for the individual decay channels.	105
5.6	The $(\kappa_\gamma, \kappa_g)$ benchmark model.	106
5.7	The histograms show the density of samples drawn from the posterior. Contours of the highest probability density intervals with 68% and 95% of posterior probability are also shown in solid black. . . .	109
5.8	Convergence checks.	109
5.9	Direct comparison of confidence and credibility intervals. The distributions obtained by sampling from the posterior are shown in blue and the profile likelihoods are shown in black.	110
5.10	Profile likelihood scans for $H \rightarrow \gamma\gamma$, $H \rightarrow ZZ^* \rightarrow 4\ell$ and $H \rightarrow WW^* \rightarrow \ell\nu\ell\nu$ in the plane $(\sigma_{ggF+ttH} \cdot BR, \sigma_{VBF+VH} \cdot BR)$	112

5.11 Simple models. (a) shows the full profile likelihood scan and compares it to a contour with fixed theory uncertainties. (b) shows how this fixed theory uncertainty contour moves and stretches when that uncertainty is fixed to a different value.	113
5.12 Response to variations of nuisance parameters in $H \rightarrow \gamma\gamma$, $H \rightarrow ZZ^* \rightarrow 4\ell$ and $H \rightarrow WW^* \rightarrow \ell\nu\ell\nu$	114
5.13 Example coupling combinations with nominal and $\times 1.3$ inflated theory uncertainties for (a) a $(\kappa_\gamma, \kappa_g)$ model and (b) a (κ_V, κ_F) model. The dashed lines are contours of a true full likelihood combination for comparison.	117

List of Tables

2.1	Production cross sections and decay branching ratios. Uncertainties correspond to total theoretical systematic uncertainty where QCD scale and PDF+ α_S uncertainties are summed linearly. Negligible cross ections are denoted with “-” [10].	28
2.2	Expected number of events for $m_H = 125\text{GeV}$ and applying the requirement $m_{4l} > 100\text{GeV}$ for the full Run I dataset of 20.7 fb^{-1} at $\sqrt{s} = 8 \text{ TeV}$ and 4.6 fb^{-1} at $\sqrt{s} = 7 \text{ TeV}$ [10].	36
2.3	Estimated number of $Z+jets$ and $t\bar{t}$ events. When two uncertainties are given, the first uncertainty is the statistical component and the second one the systematic component [10].	41
2.4	Effect of $\pm 1\sigma$ systematic uncertainty variations on signal yields for +2 jets and +1 lepton categories [10].	50
3.1	Overview of channels entering the combination during the discovery in July 2012 [12]. Some m_H ranges are split due to different optimization applied in each range.	77

5.1 Overview of channels entering the latest ATLAS combination. All analyses are updated to the full 2011 and 2012 data set. Analysis strategies were also updated to increase sensitivity to individual production modes.	96
6.1 Expected precision for benchmark coupling parameters per experiment at the LHC for integrated luminosities of 300 fb^{-1} and 3000 fb^{-1} . The range is obtained from two assumptions on the systematic and theory uncertainties [13].	119

Chapter 1

Introduction

The Standard Model (SM) of particle physics [14, 15, 16, 17] has been tested by many experiments and has been shown to successfully describe high energy particle interactions. It is a gauge theory invariant under $SU(3)_C \times SU(2)_L \times U(1)_Y$ gauge transformations, where the $SU(2)_L \times U(1)_Y$ group is associated to the electroweak interactions. The vacuum state breaks this symmetry leading to the physical electroweak bosons: a massless γ , and the massive Z , W^+ and W^- . The mechanism for electroweak symmetry breaking (EWSB) that is realized in nature was unknown at the beginning of the work for this thesis.

The Higgs mechanism (or Brout-Englert-Higgs mechanism) [18, 19] is a mechanism for EWSB but also implies the existence of a new particle, the SM Higgs boson [20, 21, 22, 23]. It is the only elementary particle of the SM that had not been observed and was one of the highlights of the LHC [24] physics program. The mechanism predicts charged and neutral Goldstone bosons and an additional scalar boson – the Higgs boson – which form a weak doublet. The three Goldstone bosons become the longitudinal components of the W^+ , W^- and Z^0 bosons to give

them mass.

The terms in the SM Lagrangian related to the Higgs field are

$$\mathcal{L}_{\text{Higgs}} = (D_\mu \Phi)^\dagger (D^\mu \Phi) - V(\Phi) \quad (1.1)$$

$$V(\Phi) = \mu^2 \Phi^\dagger \Phi + \lambda (\Phi^\dagger \Phi)^2 \quad (1.2)$$

where Φ is the new weak doublet and $V(\Phi)$ is the potential term. A finite vacuum expectation value is created by choosing $\mu^2 < 0$ and $\lambda > 0$. The gauge boson masses are generated by expanding the complex doublet Φ with four real degrees of freedom in terms of small perturbations around the vacuum state giving

$$\Phi \approx \frac{1}{\sqrt{2}} \begin{pmatrix} \theta_2 + i\theta_1 \\ v + h - i\theta_3 \end{pmatrix} \quad (1.3)$$

where v is the vacuum expectation value, $\theta_{1,2,3}$ are the three Goldstone fields and h is the Higgs field. The Goldstone fields are coupled to the gauge boson fields through the covariant derivative in the kinetic term for Φ ; see [25] for a pedagogic derivation.

Φ also couples to the SM fermions through Yukawa interactions and can provide mass terms for them:

$$\mathcal{L}_{\text{Yukawa}} = y_{ij}^l \bar{L}^i \Phi e_R^j + y_{ij}^d \bar{Q}^i \Phi d_R^j + y_{ij}^u \bar{Q}^i \Phi u_R^j + h.c. \quad (1.4)$$

where L^i and Q^i are the i^{th} generation of left-handed lepton and quark SU(2) doublets and e_R^j , d_R^j and u_R^j are the j^{th} generation of right-handed leptons, down-type and up-type quarks. The interaction strengths y_{ij}^l , y_{ij}^d and y_{ij}^u are directly

related to the observed masses of the fermions and are fundamental parameters of the theory.

Before the start of the LHC, precision electroweak results had put on upper bound on the Higgs boson mass at $m_H < 158$ GeV at 95% confidence level (CL) [26]. LEP, the previous collider in the LHC tunnel, had put a lower bound on the Higgs mass of $m_H > 114.4$ GeV using a direct search [27]. The Tevatron [28, 29, 30, 31] had also excluded the range 162 to 166 GeV with $H \rightarrow WW^*$ alone. The Higgs boson mass was the last unknown fundamental parameter of the SM of particle physics.

The naturalness problem – also called hierarchy problem – refers to the sensitivity of the Higgs boson mass to possible heavy states through higher order effects [32]. The Higgs boson mass at an energy scale Q depends on the mass parameter of the scalar potential μ and higher corrections

$$m_H^2(Q) = m_H^2(\mu) + \delta m_H^2 \quad (1.5)$$

where the corrections are

$$\delta m_H^2 = \sum_{F,B} \frac{3m_{F,B}^2}{8\pi^2} \lambda_{F,B}^2 (-1)^{2S} \ln(\mu^2/Q^2) \quad (1.6)$$

and depend on all fermions and bosons with masses $m_{F,B}$ and intrinsic spin S that have a coupling $\lambda_{F,B}$ to the Higgs boson.

There are two types of theories, weakly coupled and strongly coupled theories, that try to address this problem. Supersymmetry (SUSY) is a weakly coupled approach to the naturalness problem. It introduces a new fermion-boson symmetry and exploits the sign difference in fermionic and bosonic contributions to δm_H^2 . If

all particles in nature come in fermion-boson pairs with approximately the same mass, then their contributions cancel.

Addressing the naturalness problem is an important task at the LHC now. It is important to measure the properties of the newly found particle precisely. Besides looking for other new particles predicted by theories beyond the Standard Model, the ATLAS and CMS Higgs groups are looking for deviations in coupling strengths of the Higgs boson to other particles predicted by the SM and are testing the spin and C/P structure.

1.1 Higgs bosons at the LHC

At the LHC, Higgs bosons are produced predominantly by the four production modes shown in figure 1.1 in decreasing order in cross section. The gluon-fusion (ggF) production mode has the largest cross section at the proton-proton collider. The hard process does not produce any additional final states apart from the Higgs boson itself. The theoretical uncertainties in the cross section are large, partly due to missing calculations for higher orders in QCD. The process is particularly interesting to study in detail as the cross section for this loop process is sensitive to new particles predicted by theories beyond the Standard Model.

The second production mode is vector boson fusion (VBF). Two weak bosons radiate off two initial state quarks and fuse to a Higgs boson. The final state contains additional quarks that are mostly in the forward regions of the detector.

The LHC also produces a large number of W and Z bosons that can radiate a Higgs boson if they are created with enough energy. Associated production with a weak boson (VH) is the third largest production mode and can be identified by

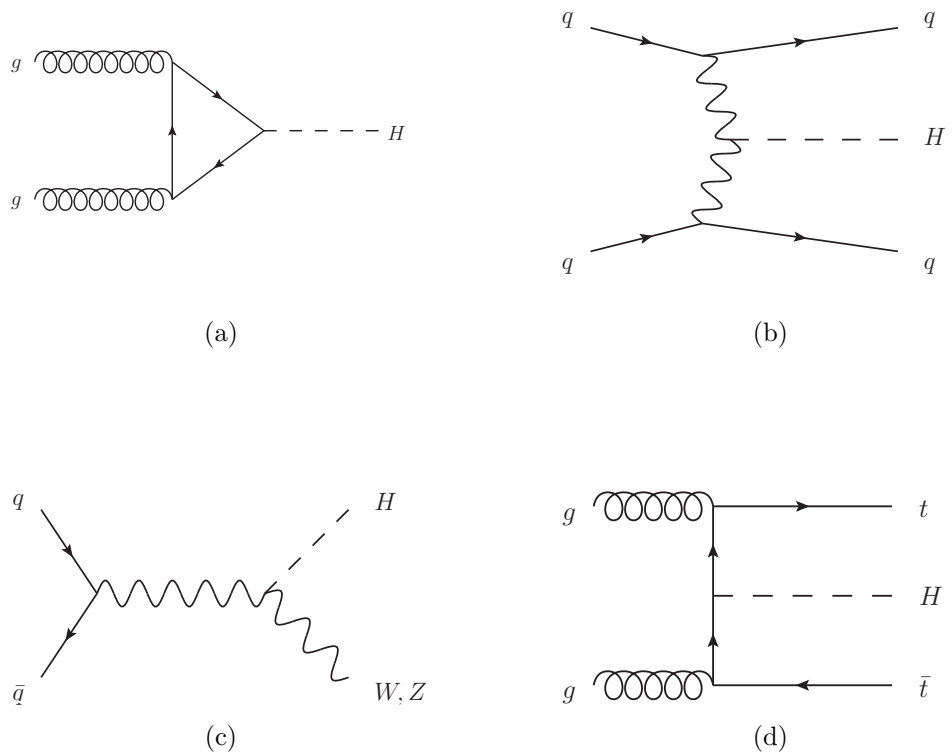


Figure 1.1: Higgs boson production modes at the LHC. Panel (a) shows the leading order Feynman diagram for gluon-fusion (ggF), (b) for vector boson fusion (VBF), (c) for associated production with a weak boson (VH) and (d) for associated production with top quarks ($t\bar{t}H$).

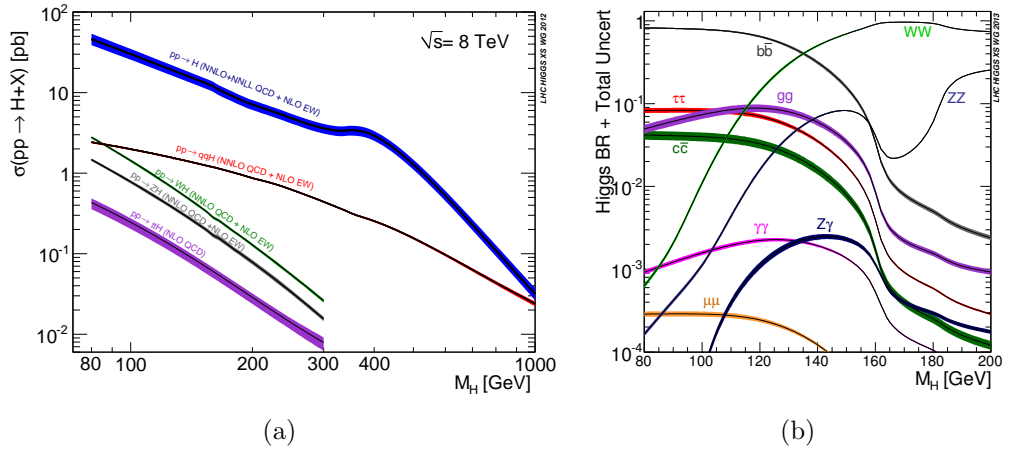


Figure 1.2: Higgs cross sections (a) and branching ratios (b) for various production modes and final states [1].

the additional W or Z boson in the final state.

Initial state gluons can convert to top quark pairs and a $t\bar{t}$ pair can fuse to a Higgs boson. The other two top quarks will be present in the final state in addition to the Higgs boson. This is the fourth largest production mode.

An overview of the cross sections of the production modes as a function of the Higgs boson mass m_H is shown in figure 1.2. It also shows the branching ratios of the Higgs boson to many final states. The event rate for a given final state is related to the product of production cross section and decay branching ratio. However, to select interesting channels to study, it is important to take the effect of backgrounds into account. This is done by studying the expected upper limits on the signal strength. The two quantities, the plain cross section times branching ratio $\sigma \times BR$ and the expected upper limit, are shown in figure 1.3. The conclusions from these two plots are quite different. For example, the event rate for $H \rightarrow ZZ^* \rightarrow 4\ell$ is small, but it is a statistically powerful channel when taking into account its clean signal and small background.

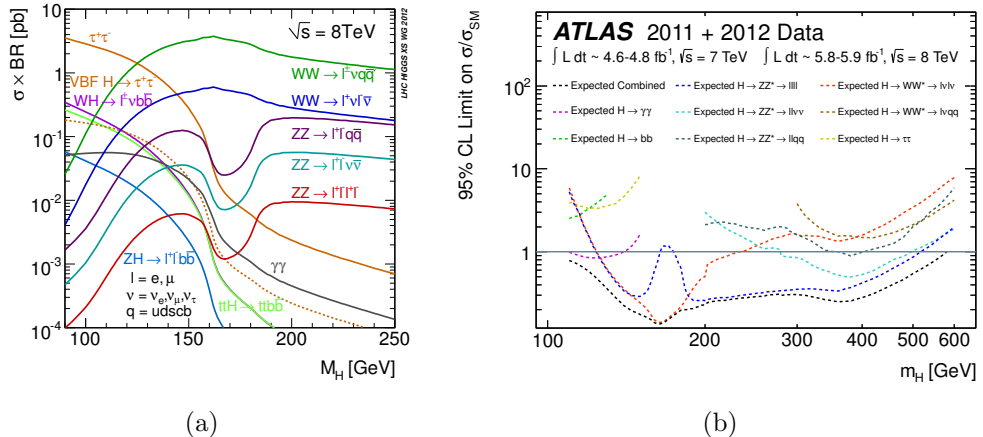


Figure 1.3: Theoretical calculations for $\sigma \times BR$ are shown in (a) and expected upper limits representing the statistical power of the analysis are shown in (b).

1.2 The ATLAS Detector

ATLAS is one of the two multi-purpose particle detectors at the LHC with the goal to identify and discover new particles [33].

The LHC is located at the European Council for Nuclear Research, or in French Conseil Européen pour la Recherche Nucléaire (CERN), in Geneva, Switzerland which was founded in 1952. At that time, fundamental physics was mostly concerned with the understanding of the interactions inside atoms and therefore the term “nuclear” [34]. Since the first proton-proton collisions in 2010, the LHC has been operated at the center of mass energies \sqrt{s} of 900 GeV, 7 TeV and 8 TeV. It is the largest collider in the world with a circumference of 27 km and is currently shut down for maintenance and upgrades and scheduled to switch back on in 2015 with $\sqrt{s} = 13$ TeV.

The LHC has four collision points at which also the four detectors were built. The detectors, or experiments, are the specialized b-physics detector LHCb, the specialized heavy ion detector ALICE and the two general purpose detectors CMS

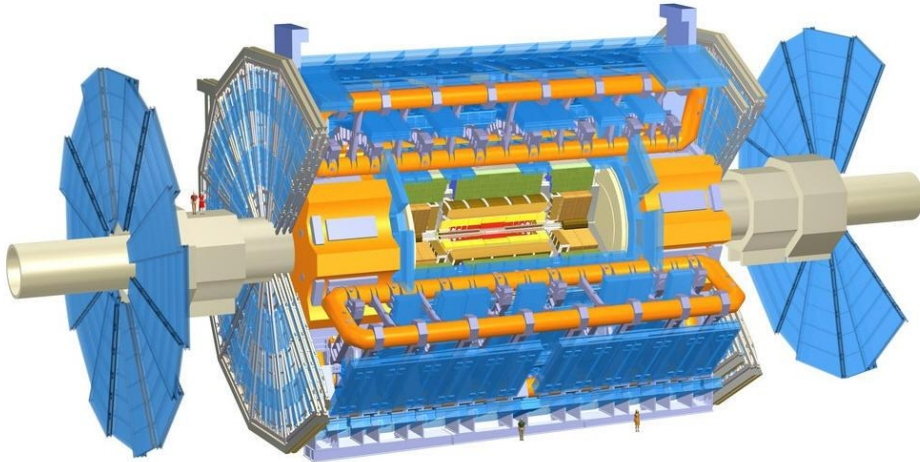


Figure 1.4: Overview of the ATLAS detector [2].

and ATLAS. The results presented in this thesis are based on up to 4.8 fb^{-1} at $\sqrt{s} = 7 \text{ TeV}$ and 21 fb^{-1} at $\sqrt{s} = 8 \text{ TeV}$ of collision data collected with the ATLAS detector shown in figure 1.4.

As a general purpose detector, the ATLAS detector must be sensitive to many particles, namely leptons, hadrons and photons. To measure the kinematics, it needs a good energy resolution over many orders of magnitude in energy. It also has to be able to continuously measure collisions at a high-rate over the entire run time of the LHC. The data of the measured events needs to be filtered, or “triggered”, and stored. It was not conceivable at the time the design was finalized to store all data in one location, so the data is distributed in real-time to computing centers around the world.

The geometry of ATLAS is a system of nested cylinders of different detector technologies. The central parts of the cylinders are sometimes called “barrels” and the ends “end caps” or “wheels”. ATLAS is built around one of the collision points in a cavern approximately 100 m under ground. It has a diameter of about

25 m, is 46 m long, weighs about 7,000 tonnes and contains about 3,000 km of electric cable. The state of the detector is read-out with approximately 100 million electronic channels.

To avoid confusion, there are official ATLAS coordinate systems. The euclidean coordinate system has the z -axis aligned along the beamline, x points towards the center of the LHC ring and y points up. The cylindrical coordinate system conventionally uses ϕ as its azimuthal angle and θ as the polar angle. However, θ is rarely used and instead expressed using the pseudorapidity $\eta = -\log \tan(\theta/2)$. Pseudorapidity η is similar to rapidity y . To show their similarity and difference, η and y can be written as

$$\eta = -\log \tan \left(\frac{|\mathbf{p}| + p_L}{|\mathbf{p}| - p_L} \right) , \quad y = -\log \tan \left(\frac{E + p_L}{E - p_L} \right) . \quad (1.7)$$

The two variables are equivalent when the energy of the particle is much larger than its mass which is generally the case at the LHC. When discussing energy and momentum measurements, the “transverse” direction is of special interest. The radial direction is what is called “transverse” and “longitudinal” means along the direction of the beamline. In a proton-proton collision, the constituent quarks and gluons take part in the hard interaction which carry an unknown fraction of the proton’s momentum. Therefore, the “longitudinal” component of the initial state momentum is unknown at hadron colliders.

Starting at the innermost layer moving radially outwards, the following sections describe the different detector components and their purpose in detail.

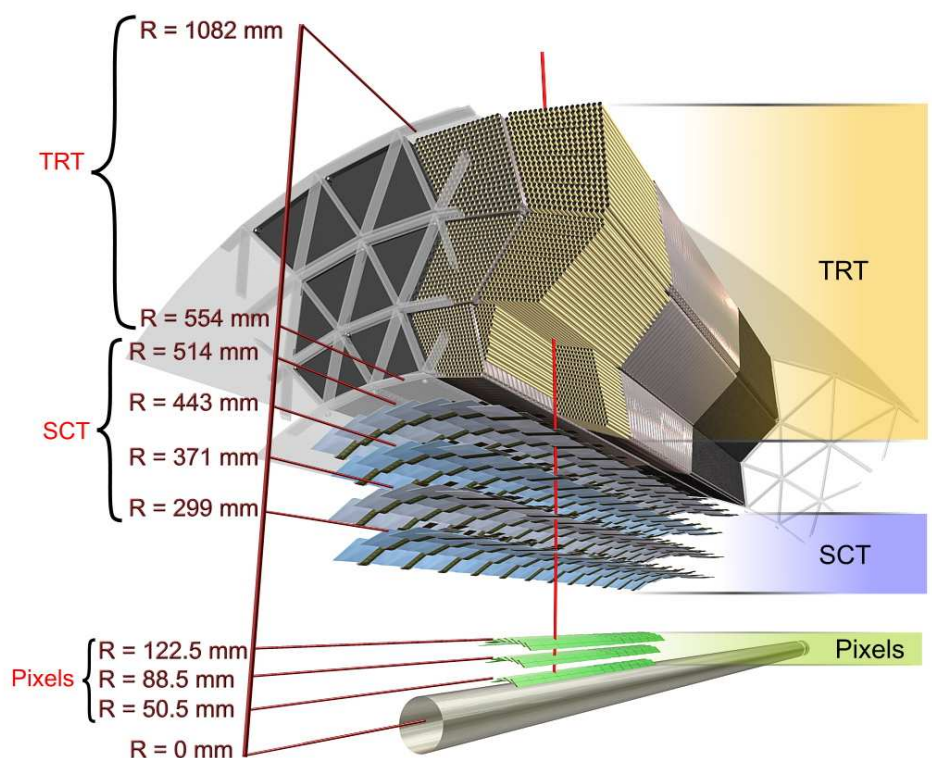


Figure 1.5: Inner detector perspective layout [3].

1.2.1 Inner Detector

The inner detector consists of the silicon pixel detector, the semiconductor tracker and the transition radiation tracker as shown in figure 1.5. It tracks the paths of charged particles. It extends out to a radius of 1.15 m from the beamline and covers a range of $|\eta| < 2.5$ for the silicon detectors and $|\eta| < 2.0$ for the transition radiation tracker. It is embedded in a 2 T solenoidal magnetic field which bends the paths of charged particles. By measuring the curvatures of the particle tracks in the inner detector, the electric charges and to some extent the momenta as well as the location of the interaction vertices can be inferred.

The silicon pixel detector (figure 1.6) is the closest detector to the interaction point. It is radiation hardened with layers of pixel modules at 5, 10 and 13 cm away from the beamline and additional modules in the endcap disks [35]. It has the highest granularity to accurately reconstruct the location of vertices; especially displaced vertices to detect τ s and b -quarks. The ongoing upgrade will substitute the current beam pipe with a smaller one [36] which will make room for an additional layer of pixel detectors; the “insertable b-layer”. A single pixel has an area of $50 \times 400 \mu\text{m}^2$. The pixel detector alone has 80.4 million readout channels.

The semiconductor tracker (SCT) has four layers in the barrel at 30.0, 37.3, 44.7 and 52.0 cm from the beamline and nine rings of modules in the end-caps on each side. The silicon strips are 6.4 cm long and 80 μm wide. Pairs of strip detectors are installed at an angle of 40 mrad between each other to provide 2D information from two 1D strips. The larger distance from the interaction point enables the SCT to have higher momentum resolution than the pixel detector. The SCT has a total of 6.2 million readout channels.

The last layer of the inner detector is the transition radiation tracker (TRT).

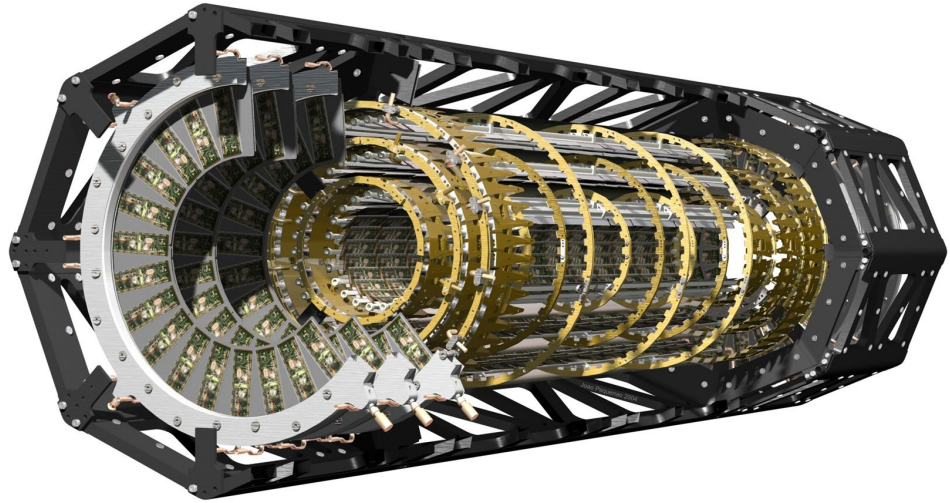


Figure 1.6: Inner detector: Pixel [4].

It covers a large volume with straw tubes that are 4 mm in diameter and up to 144 cm long with a $31 \mu\text{m}$ tungsten wire as the anode at the center. The inside of a straw has a $0.2 \mu\text{m}$ aluminum coating as the cathode. The straws are filled with Xe (70%), CO_2 (27%) and O_2 (3%). In the barrel, there are 50,000 straws parallel to the beam pipe. They are separated in the middle and the two sides are read out independently at the two ends. The end-caps contain 320,000 radially oriented straws in 18 wheels on each side giving a total number of 420,000 readouts. Each readout provides a drift time measurement. The drift time is obtained from the shape of the measured electron avalanche and is used to improve the spatial resolution down to $170 \mu\text{m}$.

1.2.2 Electromagnetic Calorimeter

The next layer moving radially outwards is the electromagnetic calorimeter. The barrel covers $|\eta| < 1.475$ and the end-caps $1.375 < |\eta| < 2.5$. It consists of alternating sheets of lead absorbers and liquid argon detector cells in a zig-

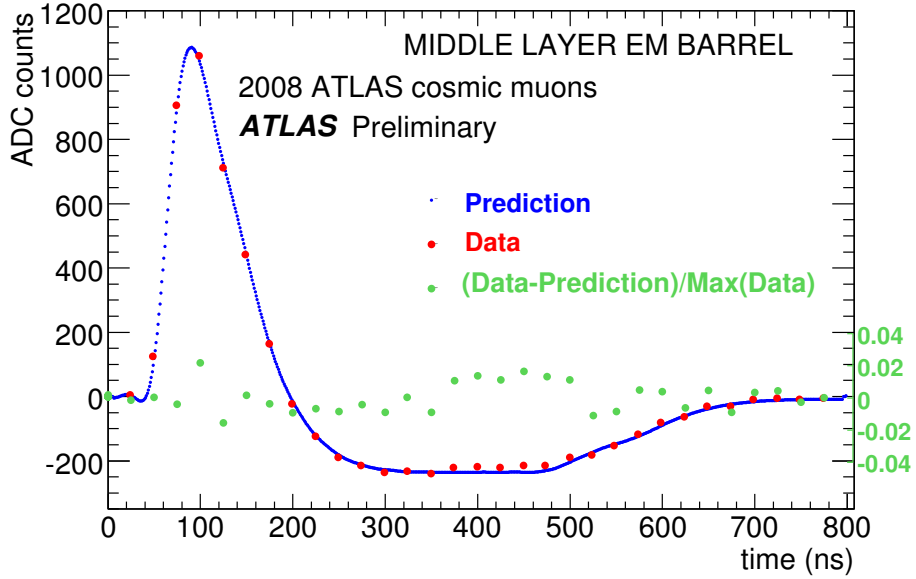


Figure 1.7: Liquid argon pulse shape [5].

zag pattern. Liquid argon was chosen for radiation hardness, speed and signal linearity and must be cooled down to 88 K. The cryostat that is responsible for the cooling also contains the solenoid magnet to reduce the amount of upstream material. The purpose of the lead absorbers is to induce showers of secondary particles which then ionize the liquid argon. By applying a high voltage of 2 kV, the detector cells measure a current of freed electrons as shown in figure 1.7 from which the shower shape and total deposited energy is inferred. Heavier charged particles like muons and pions have longer interaction lengths than electrons and photons and loose only little energy in the electromagnetic calorimeter.

Inside the coverage of the electromagnetic calorimeter at every value in (η, ϕ) , there are 3 – 4 layers with cells. The first layer, the presampler, consists of strips with a fine granularity in $(\Delta\eta, \Delta\phi)$ of $(0.0031, 0.098)$. This fine granularity helps to detect the subtle differences in the showers for example from two photons versus

a single π_0 which also decays to two photons in a small cone. The presampler is special in the sense that it does not contain lead absorbers. It corrects for the energy lost in the inner detector, magnet and cryostat. The end-caps have less upstream material and do not require a presampler. In total, the electromagnetic calorimeter has 182,468 readout channels.

1.2.3 Hadronic Calorimeter

The LHC collides hadrons which does produce a large number of QCD processes and therefore it is important to measure jets well. The general idea is to induce hadronic showers with a dense material and measure the deposited energy in the active material.

The hadronic calorimeter consists of three subsystems. The tile hadronic calorimeter in the barrel and two extended barrels that cover $|\eta| < 1.7$ [33], the hadronic end cap (HEC) calorimeter with $|\eta| < 3.2$ and the forward calorimeter (FCAL) with $3.2 < |\eta| < 4.9$.

In the barrel, the hadronic calorimeter uses steel as the absorber material and plastic scintillators as the active sampling material. The absorber and active layers have a thickness of 14 mm and 3 mm respectively. Its purpose is to measure central jets. It is 2.28 m to 4.25 m away from the interaction point. The barrel covers the pseudorapidity range $|\eta| < 1.0$ and the two extended barrel calorimeters $0.8 < |\eta| < 1.7$. The scintillating tile elements are read out using optical cables that are then connected to photomultiplier tubes. The hadronic thickness is 9.2 radiation lengths which should contain most jets and minimize “punch through” to the muon system.

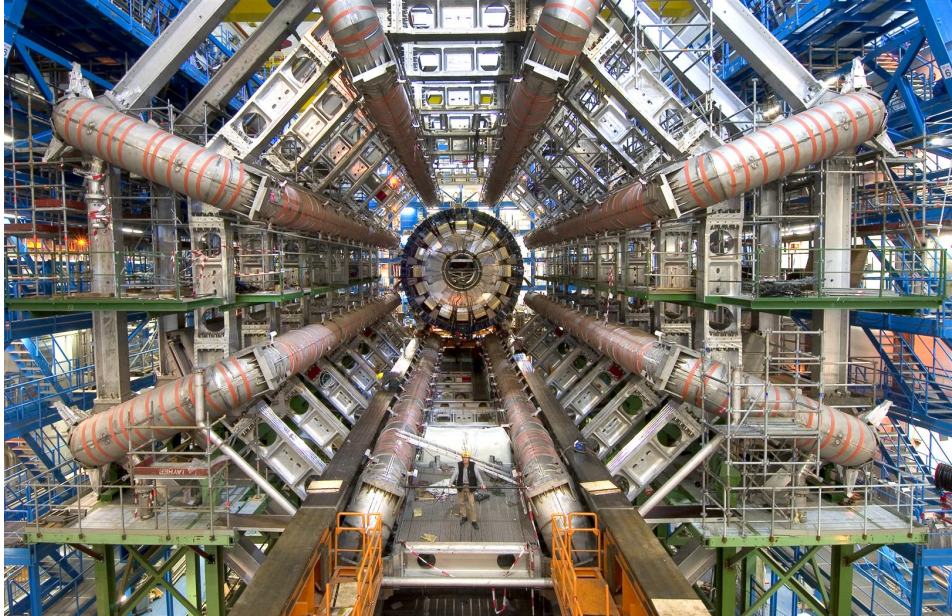


Figure 1.8: Barrel toroid magnets [6].

1.2.4 Muon Spectrometer

The muon spectrometer is ATLAS’s outermost layer of tracking chambers. It was designed to detect muons with energies of about 1 TeV at a high rate and good energy resolution. The muon system is inside an 8 T toroidal magnetic field that is produced by large barrel magnets at $|\eta| < 1.0$ shown in figure 1.8 and smaller end-cap magnets at $1.4 < |\eta| < 2.7$. The muon system employs various detector technologies where some are used to obtain fast signals for triggering like the Resistive Plate Chambers (RPCs) and Thin Gap Chambers (TGCs) and some are for obtaining precise measurements like the Monitored Drift Tubes (MDTs) and Cathode Strip Chambers (CSC).

The barrel contains three layers at 5, 7.5 and 10 m radial distance and inside $|\eta| < 1$ of MDTs and RPCs. The end-caps at 7, 10, 14 and 21-23 m in $1 < |\eta| < 2.7$ are MDTs, CSCs and TGCs. An overview schematic highlighting the muon system

is shown in figure 1.9. The positions of all chambers are actively monitored by alignment rays.

Having summarized all the detector components in the previous subsection, a schematic of logically inferring particle identities from detection or non-detection in various detector components is shown in figure 1.10.

1.3 The Trigger and Data Acquisition

Given today's technologies and the available resources, it is impossible to record and store all events. Even if it were possible, the majority of the events at the LHC correspond to processes that are considered uninteresting today. The LHC produces up to 40 million collisions per second which corresponds to 60 terabytes of data per second assuming 1.6 megabytes of RAW event size. The system that selects the interesting events from the uninteresting events is called the Trigger. It reduces the stream of events to a few hundred events per second. It is separated into three levels called the L1, L2 and EF. L1 uses dedicated microcontrollers and digital signal processors to process up to 40 million events per second and has an average output rate of 75,000 events per second. L2 takes the events from L1 and processes it on a farm of computers that are part of the High Level Trigger (HLT). Given the reduced event rate from L1, the L2 algorithms have more time and are more sophisticated in making a decision before they have to process the next event. However, the data rate is still so high that most L2 algorithms can only look at a part of the detector, the region of interest, to make a decision about this particular energy deposit. On average in the 2010 data taking period, L2 algorithms took 50 *ms* to make a decision. The output rate of L2 is about 3,000

ATLAS

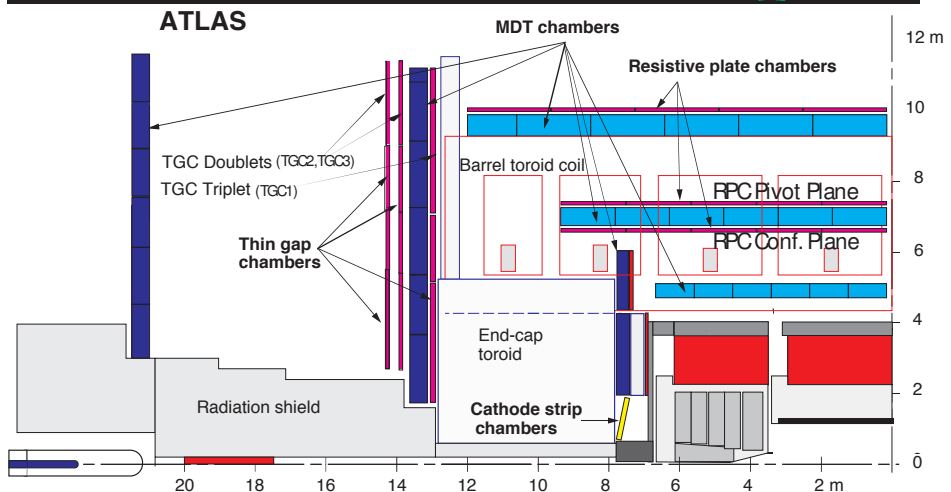
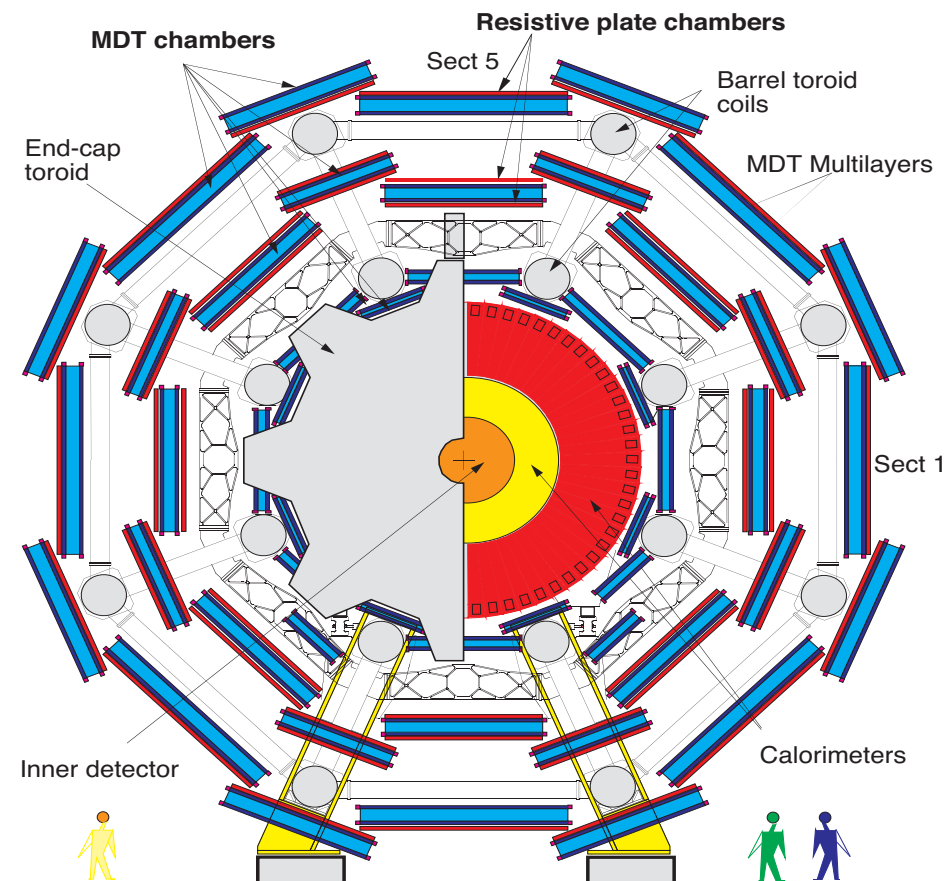


Figure 1.9: Muon system schematic [7].

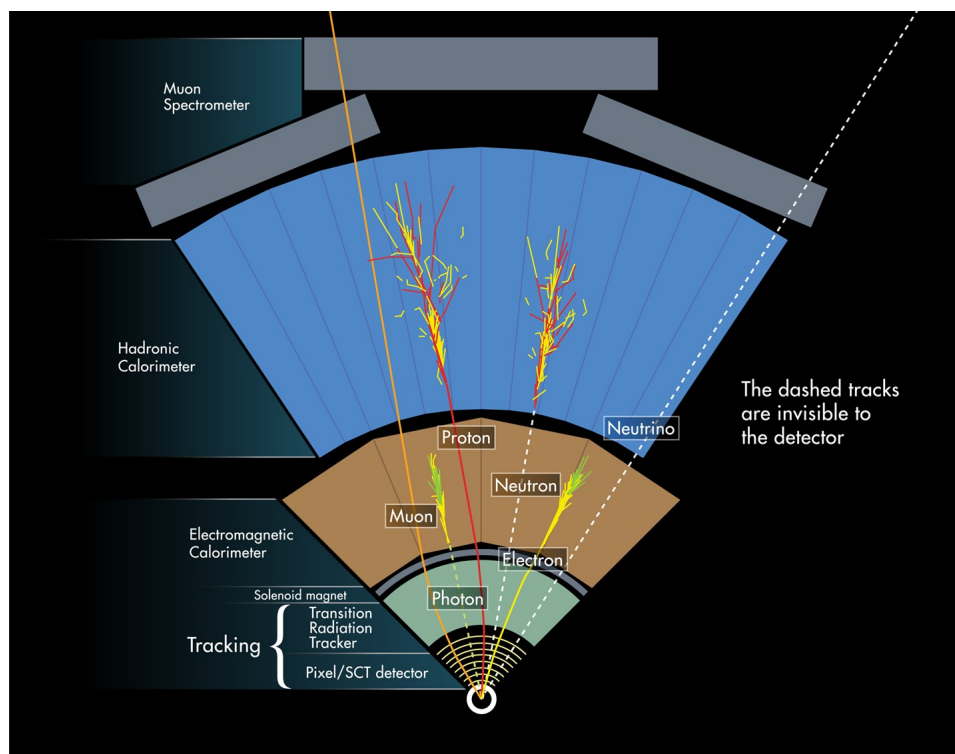


Figure 1.10: Particle identification [8].

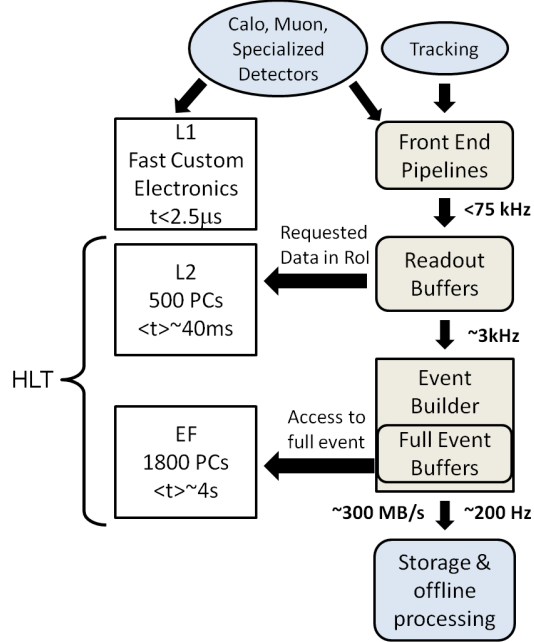


Figure 1.11: ATLAS Trigger and data acquisition schematic [9].

events per second which are fed to the EF, the Event Filer. The Event Filter is also part of the HLT computer farm. An algorithm that runs at EF level has up to three minutes to make a decision and has access to data from the full detector. In 2010, EF algorithms took on average 0.4 seconds to run. The output rate of EF has increased over time and is now at about 400 events per second [9].

Depending on the type of algorithm that labeled an event to be interesting, events are sorted into three streams which are the Egamma stream that contains events with electromagnetic clusters, the Muon stream which is mostly based on interesting signals from the muon spectrometer and the JetTauEtMiss stream with jet and tau candidates, total energy, missing energy and missing energy significance.

1.4 Data Sample

ATLAS has recorded 4.6 fb^{-1} at $\sqrt{s} = 7 \text{ TeV}$ of good data in 2011 and 20.3 fb^{-1} at $\sqrt{s} = 8 \text{ TeV}$ in 2012. In 2012 the mean number of interactions per bunch crossing (“pile-up”) was higher than in 2011. Both in 2011 and in 2012, the data taking efficiency was 93.5%. ATLAS data taking is summarized in figure 1.12.

The increased pile-up in 2012 posed a particular challenge to the trigger system. It is especially difficult for the missing transverse energy trigger to discriminate between real missing transverse energy \cancel{E}_T and energy imbalances in the calorimeter due to the high activity due to pile-up. It also impacted analyses with neutrinos in the final state that rely on precise \cancel{E}_T determinations, like $H \rightarrow WW^* \rightarrow \ell\nu\ell\nu$.

1.5 Statistical Modeling

Statistical modeling and procedures are especially well described in [37]. Further information can be found in [38, 39, 40, 41].

The recommended methods at the LHC for testing the validity of a hypothesis are based on frequentist p-values. They quantify the agreement of the observed data with a given hypothesis. All tests and limit setting procedures use the profile likelihood ratio test statistic.

The model and likelihood functions are built in the following way. The observed data set \mathcal{D}_{com} corresponds to observations in the current experiment. Another observed data set from previous experiments and previous studies in ATLAS is \mathcal{G} , the global observables. It is important to separate these two types of observed data to define ensembles of possible outcomes of the current measurement properly.

As discussed in the previous sections in detail, the statistical model for a search

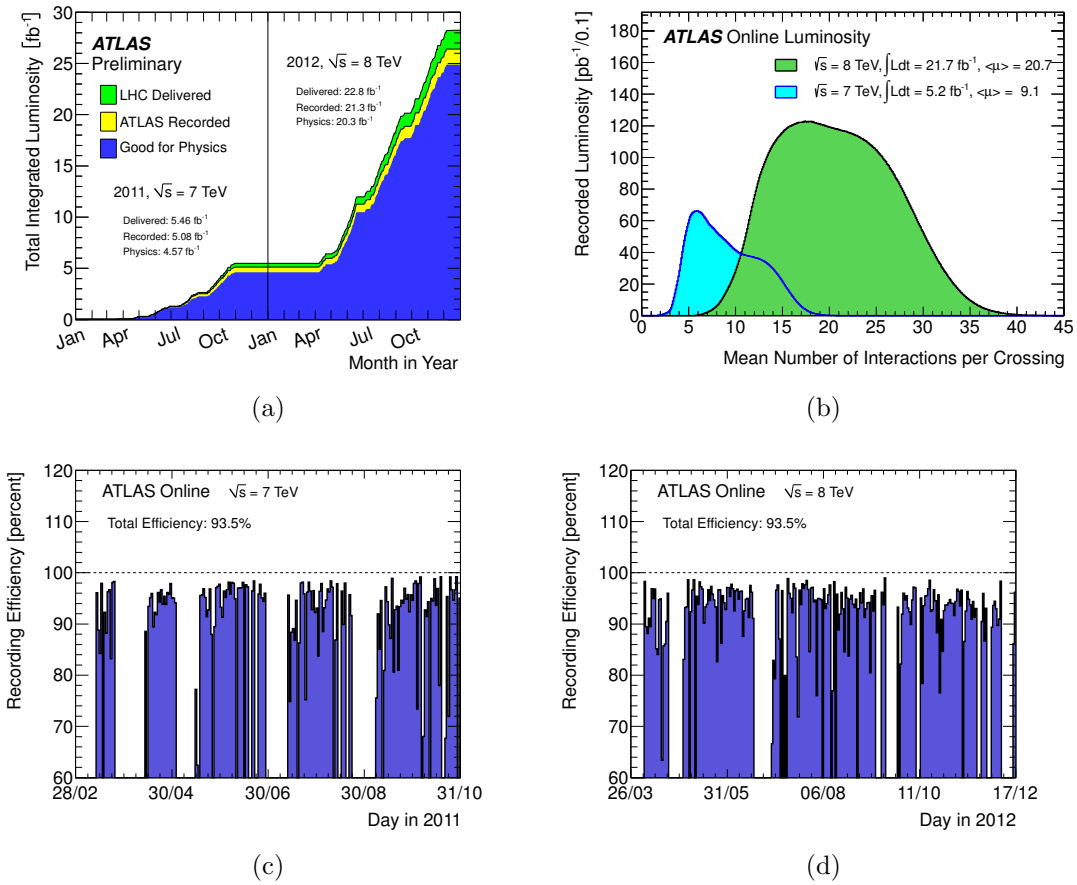


Figure 1.12: Integrated luminosity for 2011 and 2012 data taking is shown in (a) next to the mean number of interaction per bunch crossing in (b). The data taking efficiency for the two years is shown in (c) and (d).

channel c depends on its event selection. This selection procedure will pick up events from various sources and might be tuned to produce particularly strong features in a discriminating variable x like transverse mass or invariant mass. The probability density function (pdf) for x is $f(x|\boldsymbol{\alpha})$ where $\boldsymbol{\alpha}$ is the set of parameters of interest and nuisance parameters. The predicted number of events is denoted with ν which is a function of $\boldsymbol{\alpha}$. The observed data in this channel is $\mathcal{D} = \{x_1, \dots, x_n\}$ with n observed events. The probability model that is applicable here is an unbinned extended likelihood which is also called a marked Poisson model and is given by

$$f(\mathcal{D}|\boldsymbol{\alpha}) = \text{Pois}(n|\nu(\boldsymbol{\alpha})) \prod_{e=1}^n f(x_e|\boldsymbol{\alpha}) . \quad (1.8)$$

In each channel, there are several processes for signal and background that sum incoherently which means that the total expected number of events is the sum of the expected number of events from each process. The total shape is the weighted sum of each process's shape. Combining the search channels' data and models results in the combined model

$$f_{\text{com}}(\{\mathcal{D}_1, \dots, \mathcal{D}_{c_{\max}}\}|\boldsymbol{\alpha}) = \prod_{c=1}^{c_{\max}} \left\{ \text{Pois}(n_c|\nu_c(\boldsymbol{\alpha})) \prod_{e=1}^{n_c} f_c(x_{ce}|\boldsymbol{\alpha}) \right\} \quad (1.9)$$

where x_{ce} is the observed value from event e in channel c , which comes from data set \mathcal{D}_c .

Parametrization: The two hypotheses that are compared against each other are the background-only hypothesis and signal+background hypothesis, where the signal is the SM Higgs boson. It is convenient for many statistical methods, but also a good tool that provides further insight into the observed data, to connect these two hypotheses by a signal strength scale factor μ and build a single model

where $\mu = 0$ corresponds to the background-only hypothesis and $\mu = 1$ corresponds to the signal+background hypothesis. In this setting, it is convenient to use an explicit breakdown of $\boldsymbol{\alpha}$ which is $\{\mu, m_H, \boldsymbol{\theta}\}$ where $\boldsymbol{\theta}$ are all nuisance parameters.

Incorporating Results from Previous Measurements: The nuisance parameters $\boldsymbol{\theta}$ represent a wide range of effects that change the model for the Higgs search. For example, they represent a systematic uncertainty associated with our knowledge about the energy scale of certain detector elements. The measurements done for the Higgs searches are not tuned to measure these quantities precisely and are relying on measurements from performance groups in ATLAS. The performance groups' measurement is an *auxiliary* measurement for the Higgs search and their measured data \mathcal{D}_{aux} and model are written as

$$f_{\text{aux}}(\mathcal{D}_{\text{aux}} | \alpha_p, \boldsymbol{\alpha}_{\text{other}}) \quad (1.10)$$

where α_p is the nuisance parameter associated with the systematic uncertainty this auxiliary measurement was intended to constrain. This entire model and data set for this auxiliary measurement is in practice approximated by a Gaussian that is independent of $\boldsymbol{\alpha}_{\text{other}}$ and given by

$$f_p(a_p | \alpha_p, \sigma_p) \quad (1.11)$$

where a_p is a Global Observable and σ_p is the width of the Gaussian. Other approximate shapes are possible and used as well, like log-normal distributions. This simplified form of a model to measure α_p is called constraint term.

The total model for the current measurement of the Higgs signal and previous

measurements of nuisance parameters is

$$f_{\text{tot}}(\mathcal{D}_{\text{com}}, \mathcal{G} | \boldsymbol{\alpha}) = \prod_{c=1}^{c_{\max}} \left\{ \text{Pois}(n_c | \nu_c(\boldsymbol{\alpha})) \prod_{e=1}^{n_c} f_c(x_{ce} | \boldsymbol{\alpha}) \right\} \cdot \prod_p f_p(a_p | \alpha_p, \sigma_p) . \quad (1.12)$$

The response of a model due to changing nuisance parameters might change the yield, but also the shape of the model in a non-linear way. For models based on histograms filled using MC simulations, the parametric pdf $f(x|\boldsymbol{\alpha})$ is constructed from an interpolation between shapes generated for $\alpha_p = \{a_p - \sigma_p, a_p, a_p + \sigma_p\}$. A common choice for the interpolation algorithm is a piecewise function with a sixth-order polynomial with coefficients chosen such that the absolute values match at $\{a_p - \sigma_p, a_p, a_p + \sigma_p\}$ and additionally that the first and second derivatives match the extrapolation at $a_p - \sigma_p$ and $a_p + \sigma_p$.

The likelihood function corresponding to this model is

$$L(\mu, \boldsymbol{\theta}) = f_{\text{tot}}(\mathcal{D}_{\text{com}}, \mathcal{G} | \mu, m_H, \boldsymbol{\theta}) \quad (1.13)$$

where the dependence on data is implicit. At the time of the Higgs boson discovery, all models were based on a fixed m_H hypothesis which is also implicit in this notation for the likelihood.

Chapter 2

$H \rightarrow ZZ^* \rightarrow 4\ell$ Analysis

The scenario where the Higgs boson decays to two Z bosons which subsequently decay to pairs of electrons or muons, $H \rightarrow ZZ^* \rightarrow 4\ell$, is called the golden channel. The final state of four leptons is fully reconstructed and therefore this channel is expected to have a good Higgs boson mass resolution. The branching ratio of a SM Higgs boson decaying to two Z bosons is small and the branching ratio of a Z boson decaying leptonically is also small. However, the expected number of events from other processes producing four leptons in the final state is equally small which leads to a favorable signal over background ratio.

The latest ATLAS publications use the notation $H \rightarrow ZZ^* \rightarrow 4\ell$, where it is indicated that one of the Z bosons is off-shell and implying that the other Z boson is on-shell. In the signal, this configuration is likely, but also the scenario with both Z bosons off-shell is included, but the clumsy notation $Z^{(*)}Z^*$ is conventionally avoided. For the SM ZZ background, the most likely configuration depends on the four-lepton invariant mass, so the notation SM ZZ is used here instead of SM $(Z^{(*)}/\gamma*)(Z^{(*)}/\gamma*)$. Similarly for the $4l$ final state, the more accurate, but

probably confusing notation of $l^\pm l^\mp l'^\pm l'^\mp$ with $l, l' \in \{e, \mu\}$ is avoided.

During my PhD program, I contributed significant tools and analyses to the study of this channel in ATLAS. Sections 2.1, 2.2 and 2.4 are included to present a complete picture of the $H \rightarrow ZZ^* \rightarrow 4\ell$ analysis in ATLAS. Before the discovery, I was involved in studying background contributions from “fake” lepton sources (section 2.3) and the signal strength. During the discovery phase, I contributed to the simultaneous analyses of signal strength and Higgs boson mass and then implemented a new signal for the probabilistic model with particularly good features for property and mass measurements which is discussed in section 2.5.

This chapter is based on the conference notes [42, 43, 10] and the internal notes [44, 45, 46, 47, 48].

2.1 Simulation

Both signal and background events are fully simulated in GEANT4 [49] using a detailed model of the ATLAS detector [50]. Additional activity from pile-up is included in the simulation. MC samples are produced with an expected distribution of the mean number of interactions per bunch crossing that is later reweighted to the observed distribution in data.

2.1.1 Simulating Signal

The signal of a Higgs boson decaying to two Z bosons which each decay to two oppositely charged and same flavor leptons is produced using the POWHEG Monte Carlo (MC) event generator [51, 52]. It uses matrix elements for gluon fusion (ggF) and vector boson fusion (VBF) up to next-to-leading order (NLO).

The p_T spectrum for ggF is modeled according to [53] with QCD corrections up to NLO and QCD soft-gluon resummations up to next-to-next-to-leading logarithm (NNLL). Finite quark masses are taken into account [54]. The p_T reweighting of simulated events is done for 2011 simulations, but included before the simulations for 2012. Showering and hadronization is done using PYTHIA [55, 56]. Possible QED radiative corrections in final states are accounted for with PHOTOS [57, 58]. PYTHIA is used for generating VH and ttH processes.

The production cross sections and decay branching ratios are taken from [59, 60]. The ggF cross sections are calculated up to NLO [61, 62, 63] and next-to-next-to-leading order (NNLO) [64, 65, 66] in QCD, and NNLL [67], including NLO electroweak radiative corrections [68, 69]. Results are shown in [70, 71, 72] assuming factorization of QCD and EW corrections. For VBF production, full NLO QCD and EW calculations are given in [73, 74, 75], NLO calculations are available for VH [76], with NNLO in QCD [77] and NLO EW radiative corrections [78]. Cross section calculations at NLO QCD for $t\bar{t}H$ are available from [79, 80, 81, 82].

Decay branching ratios are given in [83] using PROPHECY4F [84, 85], which includes NLO QCD and EW corrections and interference between identical final-state fermions. An overview of the used production cross sections and decay branching ratios is shown in table 2.1.

Uncertainties associated with theoretical calculations are given in [1]. QCD scale uncertainties for $m_H = 125$ GeV are $^{+7\%}_{-8\%}$ for the ggF process, $\pm 1 - 2\%$ for VBF and VH and $^{+4\%}_{-9\%}$ for $t\bar{t}H$. The uncertainties arising from incomplete knowledge of parton distribution functions (PDFs) and the strong coupling constant α_S are added linearly. For gluon initiated processes, the uncertainty in PDF + α_S is $\pm 8\%$

m_H [GeV]	$\sigma(gg \rightarrow H)$ [pb]	$\sigma(qq' \rightarrow Hqq')$ [pb]	$\sigma(q\bar{q} \rightarrow WH)$ [pb]	$\sigma(q\bar{q} \rightarrow ZH)$ [pb]	$\sigma(q\bar{q}/gg \rightarrow t\bar{t}H)$ [pb]	$\text{BR}(H \rightarrow ZZ^* \rightarrow 4\ell)$ [10^{-3}]
$\sqrt{s} = 8 \text{ TeV}$						
123	20.2 ± 3.0	1.61 ± 0.05	0.73 ± 0.03	0.42 ± 0.02	0.14 ± 0.02	0.103
125	19.5 ± 2.9	$1.58^{+0.04}_{-0.05}$	0.70 ± 0.03	0.39 ± 0.02	0.13 ± 0.02	0.125
127	18.9 ± 2.8	1.55 ± 0.05	$0.66^{+0.02}_{-0.03}$	0.37 ± 0.02	$0.12^{+0.01}_{-0.02}$	0.148
300	$3.61^{+0.48}_{-0.50}$	0.44 ± 0.01	0.026 ± 0.001	0.015 ± 0.001	$0.008^{+0.01}_{-0.02}$	1.38
600	$0.52^{+0.08}_{-0.07}$	0.097 ± 0.004	—	—	—	1.23
$\sqrt{s} = 7 \text{ TeV}$						
123	$15.8^{+2.3}_{-2.4}$	1.25 ± 0.03	$0.60^{+0.02}_{-0.03}$	0.33 ± 0.02	$0.09^{+0.01}_{-0.02}$	0.103
125	15.3 ± 2.3	1.22 ± 0.03	0.57 ± 0.02	0.32 ± 0.02	$0.09^{+0.01}_{-0.02}$	0.125
127	14.9 ± 2.2	1.20 ± 0.03	0.54 ± 0.02	0.30 ± 0.02	0.08 ± 0.01	0.148
300	$2.62^{+0.36}_{-0.37}$	$0.34^{+0.02}_{-0.01}$	0.020 ± 0.001	0.012 ± 0.001	0.005 ± 0.01	1.38
600	$0.34^{+0.06}_{-0.05}$	$0.062^{+0.005}_{-0.002}$	—	—	—	1.23

Table 2.1: Production cross sections and decay branching ratios. Uncertainties correspond to total theoretical systematic uncertainty where QCD scale and PDF+ α_S uncertainties are summed linearly. Negligible cross sections are denoted with “—” [10].

and $\pm 4\%$ for quark initiated process. These values are estimated using [86], and by using CTEQ [87], MSTW [88], NNPDF [89]. The heavy Higgs line shape in ggF and VBF uses the complex-pole-scheme CPS [90] and has an uncertainty estimated using [91].

2.1.2 Simulating Background

The Standard Model ZZ background is generated with POWHEG for the quark-antiquark initial state and gg2ZZ [92] for the gluon-gluon initial state, and normalized to MCFM [93]. The ZZ^*qq' background is modeled with SHERPA [94]. The QCD scale uncertainty for these backgrounds is $\pm 5\%$. The PDF+ α_S uncertainties are $\pm 4\%$ for quark-initiated and $\pm 8\%$ for gluon-initiated backgrounds. Shape uncertainties are based on the prescription in [60].

TAUOLA is used for simulating tau decays [95, 96]. $Z + jets$ events are generated with ALPGEN [97] and normalized using control samples from data. They include $Zc\bar{c}$ and $Zb\bar{b}$ with the massless c -quark approximation and finite b -quark mass. The MLM matching scheme [98] is used to remove double counting from matrix element and parton shower jets, but not used for b -jets. $b\bar{b}$ pairs with separation $\Delta R = \sqrt{(\Delta\phi)^2 + (\Delta\eta)^2} > 0.4$ between b -quarks are taken from the matrix element calculation and from parton showers otherwise. For comparison, cross sections from QCD NNLO FEWZ [99, 100] (inclusive Z) and MCFM ($Zb\bar{b}$) are used. The $t\bar{t}$ background is generated with MC@NLO [101] and normalized to the approximate NNLO calculation from HATHOR [102]. The effect of the QCD scale uncertainty is $^{+4}_{-9}\%$ and of PDF+ α_S is $\pm 7\%$. In the tool chain, ALPGEN and MC@NLO are interfaced to HERWIG [103] and JIMMY [104] for the generation of the underlying event. The WZ background in the control regions is generated

with PYTHIA [105, 106].

2.2 Analysis Overview

One of the most basic quality requirements on the recorded data is that all relevant detector components had to be working properly. The integrated luminosity is 4.6 fb^{-1} at a center of mass energy of $\sqrt{s} = 7 \text{ TeV}$ and 20.7 fb^{-1} for $\sqrt{s} = 8 \text{ TeV}$.

2.2.1 Event Selection

The event selection for the $H \rightarrow ZZ^* \rightarrow 4\ell$ analysis uses single-lepton and di-lepton triggers. For 2012 data taking at $\sqrt{s} = 8 \text{ TeV}$, a single-muon trigger with $p_T > 24 \text{ GeV}$, a single-electron trigger with $E_T > 25 \text{ GeV}$, a di-muon trigger with (13, 13) or (18, 8) GeV thresholds in p_T for the (leading, sub-leading) muons, a di-electron trigger with (12, 12) GeV thresholds in E_T and electron-muon triggers with (12, 8) GeV and (24, 8) GeV thresholds for the (electron, muon) transverse energy and momentum were used where different electron identification requirements are applied in the two electron-muon triggers. In 2011, the LHC center of mass energy was $\sqrt{s} = 7 \text{ TeV}$ and ATLAS ran a different menu of triggers. This analysis used the single-muon trigger with a $p_T > 18 \text{ GeV}$ requirement, the single-electron trigger with $E_T > 20 - 22 \text{ GeV}$ depending on the specific data taking period, a di-muon trigger with (10, 10) GeV thresholds, a di-electron trigger with (12, 12) GeV thresholds and an electron-muon trigger with a 10 GeV transverse energy requirement on the electron and a 6 GeV transverse momentum requirement on the muon. Overall, the efficiency for the trigger part was $> 97\%$ for events

with muons and $\sim 100\%$ for events with four electrons.

Electron candidates are selected from clusters of energy in the electromagnetic calorimeter with corresponding tracks in the inner detector [107]. A Gaussian Sum Filter (GSF) algorithm [108] is used to account for energy losses due to bremsstrahlung. This improves the electron direction and impact parameter resolution. Clusters have to match longitudinal and transverse shower profiles expected from the inner detector track. The transverse momentum is computed from the cluster energy and track direction at the interaction point.

Muon candidates have to have matched inner detector tracks with complete or partial tracks in the muon spectrometer [109]. If a complete track from the inner detector and muon spectrometer is available, the momentum measurements are combined from the two components, but otherwise the momentum as measured in the inner detector is used. The η coverage for muons is extended by using the forward region of the muon spectrometer ($2.5 < |\eta| < 2.7$) which is outside the coverage of the inner detector. In the center ($|\eta| < 0.1$) which lacks muon spectrometer coverage, inner detector tracks with $p_T > 15$ GeV are identified as muons if calorimeter energies are consistent with a minimally ionizing particle. However, only one muon per event is allowed to be reconstructed by only the muon spectrometer or only the calorimeter deposits.

A Higgs candidate in this analysis consists of two same-flavor lepton pairs where in each pair the leptons have opposite charge. This is also called a *quadruplet* here, and is consistent with the four leptons coming from two Z bosons.

Further requirements in the analysis are the impact parameters of the leptons have to be less than 10 mm from the primary vertex in the transverse plane with respect to the beamline, except for forward muons without inner detector track

where no impact parameter is calculated. The primary vertex is the vertex with the highest $\sum p_T^2$ and > 3 tracks. Selected electrons have to have $E_T > 7$ GeV and $|\eta| < 2.47$. Selected muons are required to have $p_T > 6$ GeV and $|\eta| < 2.7$. In addition, the highest p_T lepton must have $p_T > 20$ GeV, the second one $p_T > 15$ GeV and the third $p_T > 10$ GeV. Also, leptons must be separated by $\Delta R > 0.1$ for same flavor, and $\Delta R > 0.2$ for opposite flavor leptons. At least one of the leptons in a quadruplet must be matched to a trigger object associated with a trigger that fired for this event.

It is possible to have multiple quadruplets in one event at this stage. To avoid double counting, this has to be resolved. The lepton pair with an invariant mass closest to the Z boson mass is referred to as the leading di-lepton pair with mass m_{12} . The event selection requires $50 \text{ GeV} < m_{12} < 106 \text{ GeV}$. Only quadruplets with the leading pair closest to the Z boson mass are kept. For events with more than four leptons, multiple quadruplets with different sub-leading lepton pairs are still possible. The invariant masses of sub-leading lepton pairs are denoted by m_{34} . In the selection, $m_{\min} < m_{34} < 115 \text{ GeV}$ with $m_{\min} = 12 \text{ GeV}$ for $m_{4l} < 140 \text{ GeV}$ which increases linearly to 50 GeV at $m_{4l} = 190 \text{ GeV}$ and stays at 50 GeV above $m_{4l} = 190 \text{ GeV}$. Z bosons corresponding to leading (sub-leading) pairs are labeled Z_1 (Z_2). All same-flavor, opposite-charge combinations of leptons in a quadruplet must have $m_{ll} > 5 \text{ GeV}$ to remove $J/\psi \rightarrow ll$ events. Finally, if more than one quadruplet remains, the one with m_{34} closest to the Z boson mass is selected.

The selected quadruplets are sorted into four categories: $4e, 2e2\mu, 2\mu2e, 4\mu$ which are ordered by the flavor of the leading di-lepton pair.

To reduce $Z + jets$ and $t\bar{t}$ backgrounds, the impact parameter significance $|d_0|/\sigma_{d_0}$ must be lower than 3.5 for muons and 6.5 for electrons.

The normalized track isolation discriminant is used to require the event to be reasonably clean. It is defined as the sum of transverse momenta of tracks, $\sum p_T$, inside a cone of $\Delta R < 0.2$ around a lepton excluding the lepton track divided by the lepton E_T . All tracks must come from the primary vertex and satisfy the following quality requirements. For muons, four hits in pixel and silicon strip detectors and a $p_T > 1$ GeV is required. For electrons measured in 2012, nine silicon hits (one in the innermost layer) and a $p_T > 0.4$ GeV is required. Seven silicon hits (one in innermost layer) and a $p_T > 1$ GeV is required for 2011 electrons. All leptons must have a normalized track isolation of < 0.15 . The name is a misnomer as the discriminant’s value shows “activity”, but it can be used for an isolation requirement when requiring the discriminant to be small.

Similar to the normalized isolation requirement on tracks in the inner detector, there is a normalized calorimetric isolation. For 2012 electrons, the sum of the positive-energy topological clusters [110] in the electromagnetic and hadronic calorimeter with a reconstructed barycenter falling in a cone of $\Delta R < 0.2$ around the candidate electron cluster, divided by the electron E_T is required to be less than 0.2. The cells with $\Delta\eta = 0.125$ and $\Delta\phi = 0.175$ around the electron barycenter are excluded from this calculation as they represent the “core” of the measured electron. The topological clustering algorithm suppresses noise by removing cells without a significant energy deposit in the cell itself or its neighboring cells. There is also “ambient energy” from pile-up and the underlying event. This energy is estimated and subtracted by averaging over the transverse energy density from low- p_T jets. Averaging is done over azimuth in two η regions. For 2011, the calorimeter isolation of electrons is cell-based instead of based on topological clusters in the electromagnetic and hadronic calorimeters and a value of less than 0.3 is required.

For muons, the normalized calorimetric isolation discriminant is defined as the sum of the calorimeter cells, $\sum E_T$, above 3.4 times the average noise fluctuation inside a cone of $\Delta R < 0.2$ around the muon direction, divided by the muon p_T . This value has to be smaller than 0.3, and smaller than 0.15 in the case of muons without an inner detector track. In all cases, contributions to p_T and E_T from other leptons of the quadruplet are subtracted.

Final State Radiation (FSR) is the emission of a photon from a final state lepton. It is simulated in MC. When modeling the invariant mass of the leptons to reconstruct the mass of the parent particle, the emitted photon should also be included, which is called FSR correction. This is done to improve the invariant mass resolution of the four-lepton system which in turn improves the Higgs mass measurement. The FSR correction for di-muon Z_1 candidates is only applied when $66 \text{ GeV} < m_{12} < 89 \text{ GeV}$ and the corrected m_{12} is less than 106 GeV. It adds photons with $E_T > 1 \text{ GeV}$ in a cone of $\Delta R < 0.08$ to 0.15 depending on the photon E_T to the muon. This recovers 70% of FSR photons within a fiducial region. About 85% of the corrected events have a true FSR photon. The other photon sources are pile-up and muon ionization.

The selection efficiency for the 2012 analysis and $m_H = 125 \text{ GeV}$ is 39% (4μ), 26% ($2e2\mu/2\mu2e$) and 19% ($4e$) and for 2011 it is 39% (4μ), 21% ($2e2\mu/2\mu2e$) and 15% ($4e$).

Furthermore, the Z boson mass constraint improves the m_{4l} resolution. It is only applied to the leading di-lepton pair when $m_{4l} < 190 \text{ GeV}$ and to both pairs for $m_{4l} > 190 \text{ GeV}$.

2.2.2 Additional Jet and Lepton Selection

The latest $H \rightarrow ZZ^* \rightarrow 4\ell$ analyses in ATLAS include a special selection on addition jets and leptons. The purpose is to obtain a handle on the production modes of the Higgs boson by having analysis categories with enhancements to certain production modes. This is then used to separately measure ggF, VBF and VH production cross sections. The categories are the four previously discussed categories by final state that are collectively called “main” and two additional categories “+2 jets” and “+1 lepton”.

+2 jets category: The selection for this category requires two additional high p_T jets with large rapidity separation. Topological clusters are used with the anti- k_t algorithm [111] and cone size $R = 0.4$ to identify jets. Jets within the inner detector acceptance ($|\eta| < 2.47$) are required to have $> 50\%$ of $\sum |p_T^{tracks}|$ originate from the primary vertex to suppress pile-up. Jets are required to have $p_T > 25$ GeV when they are inside $|\eta| < 2.5$ and $p_T > 30$ GeV in the region $2.5 < |\eta| < 4.5$. Once all jets are identified, a $\Delta\eta > 3$ and $m_{inv} > 350$ GeV is required for the highest p_T jets.

+1 lepton category: Events that fail the “+2 jets category” requirements are considered for the “+1 lepton category”. For this category, the event needs to contain an extra electron or muon with $p_T > 8$ GeV and other lepton requirements as in the main selection.

main categories: Events that fail both the “+2 jets” and “+1 lepton” category requirements are placed in one of the four main categories.

The expected number of events after this categorization are shown in table 2.2.

category	ggF, ttH	VBF	VH	ZZ
$\sqrt{s} = 8 \text{ TeV}$				
main	13.5	0.79	0.65	320.4
+2 jets	0.28	0.43	0.01	3.58
+1 lepton	0.06	-	0.14	0.29
$\sqrt{s} = 7 \text{ TeV}$				
main	2.20	0.14	0.11	57.7
+2 jets	0.03	0.06	-	0.44
+1 lepton	0.01	-	0.03	0.25

Table 2.2: Expected number of events for $m_H = 125 \text{ GeV}$ and applying the requirement $m_{4l} > 100 \text{ GeV}$ for the full Run I dataset of 20.7 fb^{-1} at $\sqrt{s} = 8 \text{ TeV}$ and 4.6 fb^{-1} at $\sqrt{s} = 7 \text{ TeV}$ [10].

2.2.3 Background Estimation

The irreducible SM ZZ background is obtained from MC simulations and normalized to theoretical cross section calculations. Data driven methods are used for the reducible backgrounds that are $Z + jets$ and $t\bar{t}$. Different approaches are used depending on the flavor of the subleading lepton pair.

Subleading Di-Muon Pair: Standard Model backgrounds come from $t\bar{t}$ processes and $Z + jets$ where $Z + jets$ includes a heavy quark $Zb\bar{b}$ component and π/K in-flight decays. Two control regions are used. Control region (1) has an enhanced $Zb\bar{b}$ component but π/K in-flight decays are suppressed and control region (2) has both components enhanced.

Control region (1) is similar to the signal region, but the isolation requirement is removed from the subleading pair selection. It is required that one of the subleading leptons fails the impact parameter significance requirement which suppresses ZZ but enhances $t\bar{t}$ and $Zb\bar{b}$ in this control region. The control region is visualized in

figure 2.1. In m_{12} , the $t\bar{t}$ component is flat and fitted to a second order Chebyshev polynomial whereas the $Z + jets$ component is peaked and fitted to a Breit-Wigner convoluted with a Crystal-Ball function. $Zb\bar{b}$ MC is used to derive a transfer factor from the number of events in the control region to the number of events in the signal region. In turn, the accuracy of the MC to obtain this transfer factor has been verified with data using another control region (3) that only requires a Z boson and exactly one extra muon. The extra muon has to satisfy the same requirements as a muon in the leading pair. An uncertainty of $\pm 10\%$ is assigned to this procedure of obtaining the transfer factor. This uncertainty is obtained from the difference between the MC based estimate and the control region (3) estimate.

Control region (2) is similar to control region (1) but instead of requiring that a subleading lepton fails the impact parameter significance requirement, it is required that one of the subleading leptons fails the track isolation requirement. This enhances $Zb\bar{b}$ and $t\bar{t}$ and removes much of ZZ as in control region (1), but also enhances π/K in-flight decays. The combination of control region (1) and (2) is used to estimate the π/K in-flight decay contribution to $Z + jets$ and amounts to about 20%.

Subleading Di-Electron Pair: There are various sources for what is called an electron at reconstruction level. There are true isolated electrons, electrons from heavy flavor decays, electrons from photon conversions and light jets misreconstructed as electrons. We have four methods to estimate the ll+ee background. Each of them has a control region and a transfer factor for each component to map from the control to the signal region.

For the first method, the control region has relaxed electron selection criteria for the sub-leading pair, so the events in the signal region are a subset of the events

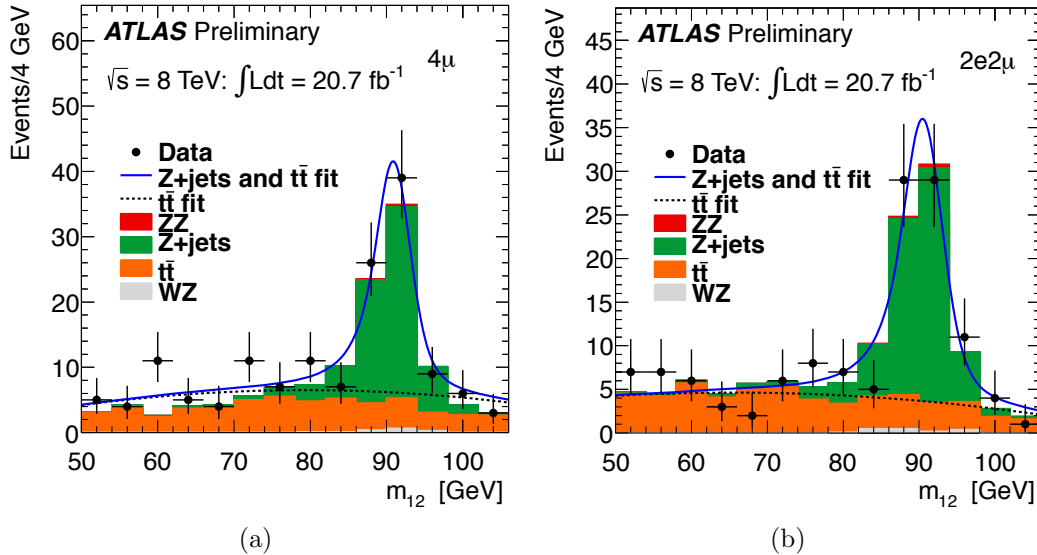


Figure 2.1: $H \rightarrow ZZ^* \rightarrow 4\ell$ control region (1). (a) shows the 4μ and (b) the $2e2\mu$ final state. The functional form that is fitted is a second order Chebyshev polynomial for the flat $t\bar{t}$ background and a Breit-Wigner for the peaked $Z + jets$ component convoluted with a Crystal-Ball function [10].

in the control region. The relative composition of the control region is estimated using reconstruction categories, i.e. it is based on whether a candidate lepton also satisfies tighter lepton requirements. The transfer factors for each component are derived using MC truth information.

The second method is referred to as $3l + l$. The sub-leading di-electron pair is same-sign. The name is derived from the requirement that the first three highest p_T leptons satisfy all analysis criteria, but the remaining electron is only required to have a good track with $n_{\text{hits}}^{\text{silicon}} \geq 7$ and $n_{\text{hits}}^{\text{pixel}} \geq 1$ and the lateral containment of the cluster energy along η . The different truth components are estimated using templates derived from MC in $n_{\text{hits}}^{\text{b-layer}}$ and R_{TRT} .

The control regions with sub-leading electron and muon pairs are shown in figure 2.2.

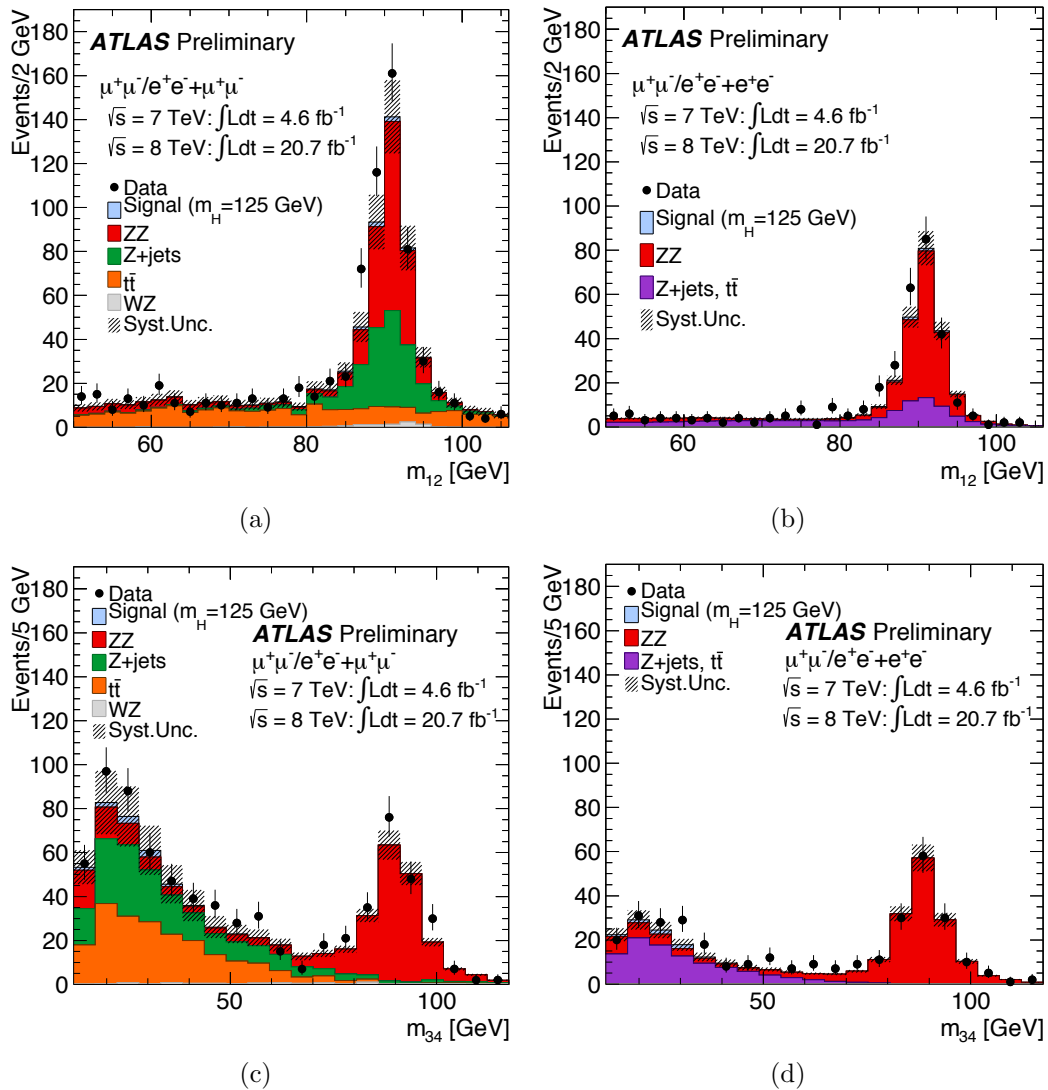


Figure 2.2: Invariant mass distributions for leading and sub-leading leptons pairs in the control region defined by a lepton pair forming a Z boson and a same-flavor lepton pair that can be both same-sign or opposite-sign.

+2 jets and +1 lepton categories: Similar techniques for background estimates are used with the additional requirements from the main selection.

All background estimates that are used in the official analysis are summarized in table 2.3. Using the full dataset, the results of the event selection and background estimates are shown in figure 2.3.

2.3 Estimating Fake Rates

This section summarizes an early study on fake rate estimations with the first 2 fb^{-1} collected in 2011 at $\sqrt{s} = 7 \text{ TeV}$. The purpose is to understand discrepancies between observed data and MC simulations. For loose definitions of electrons and muons as used in the $H \rightarrow ZZ^* \rightarrow 4\ell$ analysis, there are many sources for objects that get identified as electrons or muons and they might not all be modeled sufficiently in MC simulations. Therefore, a data-driven approach using fake factors is considered. The study shown here and other studies on data-driven fake estimates are the basis for the current methods used in the official ATLAS analysis of $H \rightarrow ZZ^* \rightarrow 4\ell$.

The event selection for this study is similar to the event selection that was used for the main ATLAS analysis for $H \rightarrow ZZ^* \rightarrow 4\ell$ at the time. No events with five or more leptons are observed in this data sample.

To increase sensitivity to non-SM phenomena, this study did not have the usual flavor and charge requirements on the second pair of leptons. In addition to the search for $H \rightarrow ZZ^* \rightarrow 4\ell$, this allows for new physics phenomena, such as $Z' \rightarrow HZ$ where H decays to $\tau\tau$ or WW , supersymmetric cascade decays, decays of microscopic black holes, etc. The most important Standard Model processes

method	estimate at $\sqrt{s} = 8$ TeV	estimate at $\sqrt{s} = 7$ TeV
4μ		
Z+jets	$2.4 \pm 0.5 \pm 0.6$	$0.22 \pm 0.07 \pm 0.02$
$t\bar{t}$	$0.14 \pm 0.03 \pm 0.03$	$0.03 \pm 0.01 \pm 0.01$
$2e2\mu$		
Z+jets	$2.5 \pm 0.5 \pm 0.6$	$0.19 \pm 0.06 \pm 0.02$
$t\bar{t}$	$0.10 \pm 0.02 \pm 0.02$	$0.03 \pm 0.01 \pm 0.01$
$2\mu2e$		
relaxed cuts	$5.2 \pm 0.4 \pm 0.5$	-
$3l + l$	-	$2.8 \pm 0.4 \pm 0.5$
$4e$		
relaxed cuts	$3.2 \pm 0.5 \pm 0.4$	-
$3l + l$	-	$2.5 \pm 0.3 \pm 0.5$
$+2$ jets		
summed	0.33 ± 0.09	0.15 ± 0.07
$+1$ lepton		
summed	0.08 ± 0.04	0.03 ± 0.02

Table 2.3: Estimated number of $Z + jets$ and $t\bar{t}$ events. When two uncertainties are given, the first uncertainty is the statistical component and the second one the systematic component [10].

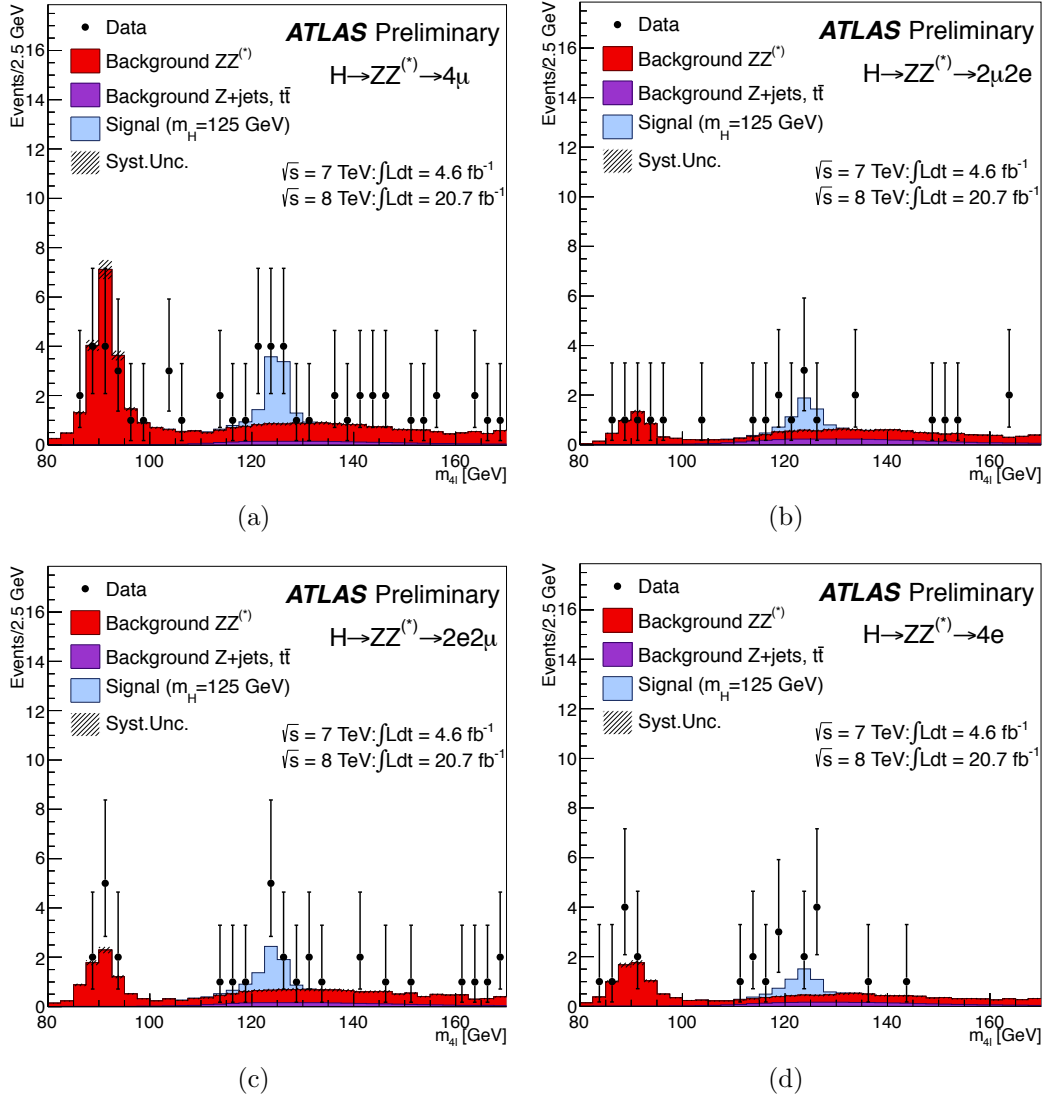


Figure 2.3: Event selection results for $H \rightarrow ZZ^* \rightarrow 4\ell$ [10].

contributing to the background of this analysis are ZZ , $t\bar{t}$ and (semi-)leptonic $Zb\bar{b}$ as well as $Z + jets$ with misidentification and the diboson backgrounds WW and WZ .

The object identification of muons, electrons and jets was close to, but not exactly the same as in the main analysis.

Lepton Fake Rate: After selecting events from data, an estimate of the contamination from “fakes” is necessary. Fake leptons are leptons originating from heavy flavor decays, reconstructed jets, photons, photon conversions and π_0 mesons identified as electrons as well as true muons produced in π/K in-flight decays.

The two leading leptons are required to be compatible with a Z boson using a mass window cut and requiring same flavor and opposite charge. The leading leptons also have to have high p_T . Therefore it is assumed that these two leptons are always real and never fake. The other two leptons can have low p_T and do not have a requirement on the invariant mass, charge or flavor.

The approach to estimate the contribution from fakes is similar to [112]. The notation needs to distinguish between truth level information and measured information. The truth level is denoted by T and F for true and fake leptons. The corresponding measured quantities are objects passing tighter selection – called L – and objects only passing looser or inverted selection – called J . The first two leptons that are assumed to never be fakes are denoted by a dash “-” acting as a place holder.

When extending the transfer factor method to two objects, it is best to require a strict order in the subscripts first. At the end of the derivation, it is easy to take into account that the ordering is not measurable. The notation $N_{--L_1J_2}$ and $N_{--J_1L_2}$ is introduced where the subscripts 1 and 2 label the slot. This results in

the expected number of events containing fakes

$$N_{--L_1 L_2}^{fake} = N_{--F_1 F_2} \cdot f_1 \cdot f_2 + N_{--T_1 F_2} \cdot f_2 + N_{--F_1 T_2} \cdot f_1$$

where $N_{--T_1 F_2}$, $N_{--F_1 T_2}$ and $N_{--F_1 F_2}$ are the numbers of events with one and two fake leptons in the signal region and f_1 and f_2 are the fraction of fakes identified as leptons. $N_{--T_1 F_2}$, $N_{--F_1 T_2}$ and $N_{--F_1 F_2}$ cannot be observed in data and are inferred from the observed number of events with one or two lepton-like jets $N_{--L_1 J_2}$, $N_{--J_1 L_2}$ and $N_{--J_1 J_2}$. The observed and truth level numbers are related by the following system of equations:

$$\begin{cases} N_{--L_1 J_2} = N_{--T_1 F_2}(1 - f_2) + N_{--F_1 F_2}f_1(1 - f_2) \\ N_{--J_1 L_2} = N_{--F_1 T_2}(1 - f_1) + N_{--F_1 F_2}f_2(1 - f_1) \\ N_{--J_1 J_2} = N_{--F_1 F_2}(1 - f_1)(1 - f_2) \end{cases}$$

This system can be used in the previous equation to substitute all the truth level quantities with measurable quantities.

$$N_{--L_1 L_2}^{fake} = -N_{--J_1 J_2} \frac{f_1}{1 - f_1} \frac{f_2}{1 - f_2} + N_{--L_1 J_2} \frac{f_2}{1 - f_2} + N_{--J_1 L_2} \frac{f_1}{1 - f_1} \quad (2.1)$$

The probability of faking a lepton is denoted by f . The quantity FR is defined by

$$FR \equiv \frac{f}{1 - f} \quad (2.2)$$

and denotes the ratio of the number of lepton-like jets accepted and rejected by our lepton selection cuts. A lepton-like jet is defined as a reconstructed lepton which fails the lepton identification or isolation requirement. For muons, we define

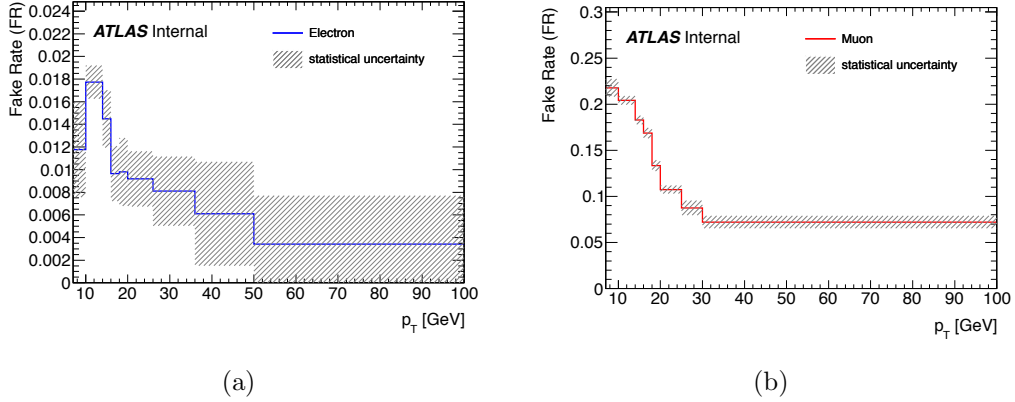


Figure 2.4: Estimated fake factors FR.

a selected muon to have $p_T^{\text{tracks}}(\Delta R < 0.2)/p_T^\mu < 0.15$ and a muon-like jet failing that isolation requirement. For electrons, we require the same isolation and in addition MEDIUM quality. For electron-like jets, we require that one of the two conditions is failing.

To collect events for signal and control regions, triggers without lepton-specific isolation are used (`EF_gg11_etcut` and `EF_mu13_MG`).

FR measured with non-lepton-specific triggers is

$$FR = \frac{N_{\text{selected leptons}}^{\text{data}} - N_{\text{selected leptons}}^{\text{MC}}}{N_{\text{lepton-like jets}}^{\text{data}} - N_{\text{lepton-like jets}}^{\text{MC}}} \quad (2.3)$$

where N^{MC} represents the Monte-Carlo estimate of the remaining contributions of known processes with real leptons in the final state. The largest contributions are W , Z and t decays. The obtained fake factors FR for electrons and muons are shown in figure 2.4.

The fact that the 3rd and 4th lepton are indistinguishable in observed events

is accounted for using

$$\begin{aligned} N_{--LL} &= N_{--L_1 L_2} \\ N_{--JJ} &= N_{--J_1 J_2} \\ N_{--LJ} &= N_{--L_1 J_2} + N_{--J_1 L_2} \end{aligned}$$

which gives

$$N_{--LL}^{\text{fake}} = -N_{--JJ} \cdot FR \cdot FR + N_{--LJ} \cdot FR \quad (2.4)$$

where FR refers to a corresponding J . Written in this form, this equation can be extended to FR factors that depend on kinematic properties of the object J , like p_T .

Three lepton case: The 3-lepton study investigates the above method in the case of three leptons. The higher number of observed 3-lepton events allows for a more detailed study of the method and especially allows for a direct comparison of data-driven estimates to MC estimates and data. In this selection, most events of the form $Z + l$ are $Z + \text{jets}$ at truth level. The processes ZZ , WZ , $t\bar{t}$ and $Z\bar{b}$ are also present.

The selection of candidate events is similar to the $4l$ case with the exception that only one lepton in addition to the leading pair is required. Similarly, the fake estimate is

$$N_{--L}^{\text{fake}} = N_{--J} \cdot FR(J) \quad (2.5)$$

Figure 2.5 shows the plain MC result without data-driven methods applied. Figure 2.6 shows how that picture changes with data-driven methods. Around the Z mass, there seems to be a problem with the data-driven estimate. An

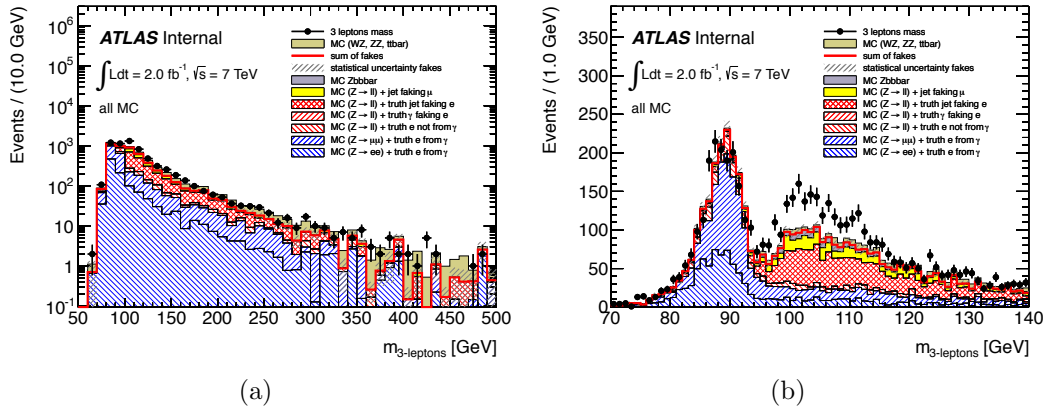


Figure 2.5: Monte Carlo estimates of $m_{3\text{-lepton}}$ spectrum.

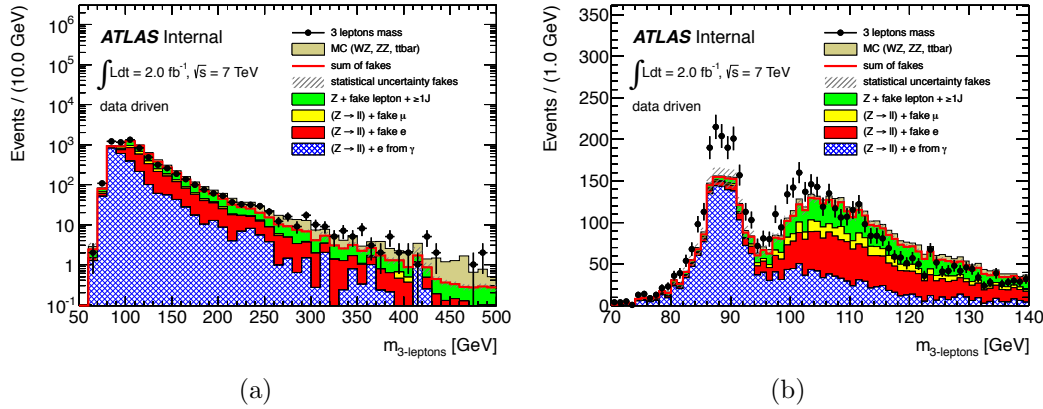


Figure 2.6: Data-driven estimates of $m_{3\text{-lepton}}$ spectrum.

investigation using Monte Carlo truth information showed that the discrepancy comes from electrons from photons radiated off the initial state. This was not taken into account in this analysis.

Applying 3-lepton insights to 4-lepton study: The three lepton study pointed out some missing contributions in the MC simulations, but also in the used data-driven approach. To study the size of the effect in the 4-lepton analysis, the data-driven approach was applied to the loose 4-lepton analysis and the difference between MC and data-driven approach are shown in figure 2.7.

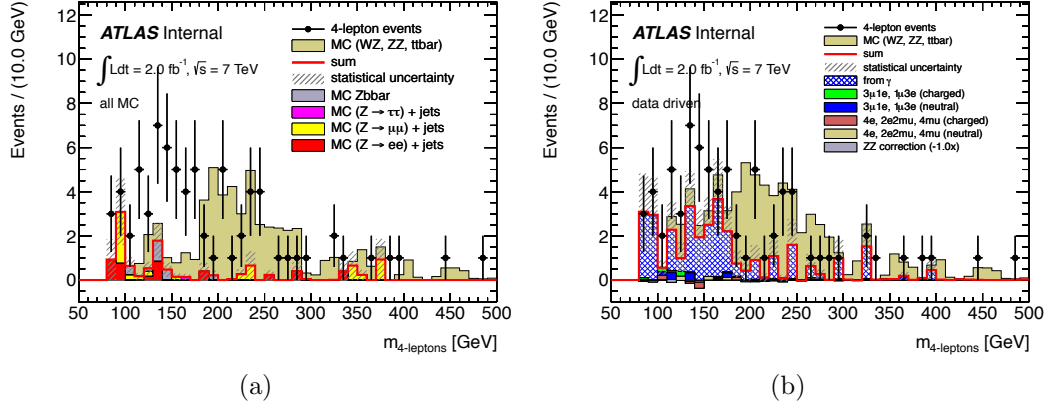


Figure 2.7: Monte Carlo (left) and data-driven (right) estimates of $m_{4\text{-leptons}}$ spectrum.

The method shown here and other studies were the basis for further studies in the $H \rightarrow ZZ^* \rightarrow 4\ell$ working group in ATLAS. The method for the official results improves on the work shown here by accounting for different transfer factors depending on the type of the source for the fake leptons.

2.4 Systematic Uncertainties

The following discussion separates uncertainties by the corresponding effect on the model. The first part discusses systematics that mostly affect the signal rate, the second part systematics that affect the mass measurement and the third part looks into systematics that affect the categorization of events. The size of the uncertainties are usually estimated by rerunning the full MC production with a few different values of the systematic that is studied and observing the change in that sample. For example, the systematic for an identification efficiency of an electron or muon is obtained by running all MC samples with a nominal value and $\pm 1\sigma$ variations and observing the change in the number of selected events. The

efficiencies that correspond to nominal and $\pm 1\sigma$ values were obtained by ATLAS's performance groups.

Signal rate: The signal rate is affected when a systematic changes a value that is used for event selection. Muon identification and reconstruction efficiency are estimated from MC to be $\pm 0.8\%$ (4μ), $\pm 0.4\%$ ($2\mu 2e$) and $\pm 0.4\%$ ($2e 2\mu$). Similarly, the efficiency uncertainties for electrons are $\pm 2.4\%$ ($4e$), $\pm 1.8\%$ ($2\mu 2e$) and $\pm 1.6\%$ ($2e 2\mu$) at $m_{4l} = 1$ TeV but are much larger around $m_{4l} = 125$ GeV with $\pm 9.4\%$ ($4e$), $\pm 8.7\%$ ($2\mu 2e$) and $\pm 2.4\%$ ($2e 2\mu$).

The isolation and impact parameter requirements have an associated selection efficiency that might in principle be different between MC and data events. That efficiency has been studied using $Z \rightarrow ll$ events in data and MC and good agreement with negligible uncertainty was found.

The p_T spectrum of ggF processes is a sensitive quantity. For 2011 data, the spectrum is re-weighted at analysis level. For 2012, this re-weighting is applied directly in the event generation and therefore included in the full detector simulation. A $\pm 1\%$ uncertainty is applied to allow for possible mismodeling. This number is obtained by testing various options for p_T spectra according to PDF and QCD scale uncertainties.

Background and overall rate: The background rate uncertainties were already included in table 2.3. The overall uncertainty on the luminosity is obtained from dedicated beam-separation scans (van der Meer scans) that were performed by the LHC. For 2011 and 2012, the uncertainties were estimated to be $\pm 1.8\%$ and $\pm 3.6\%$ respectively. The uncertainties that correspond to the incomplete understanding of theoretical calculations of cross sections for the ZZ background and signal were discussed in section 2.1.

process	ggF + ttH	VBF	VH	ZZ
+2 jets category				
theory cross section	21%	4%	4%	35%
underlying event	19%	4%	-	-
jet energy scale	14%	10%	10%	10%
+1 lepton category				
theory cross section	15%	4%	4%	30%
+1 lepton specific	3%	3%	5%	-

Table 2.4: Effect of $\pm 1\sigma$ systematic uncertainty variations on signal yields for +2 jets and +1 lepton categories [10].

Mass: Uncertainties on the measured Higgs mass originate mostly from energy and momentum scale uncertainties of the measured electrons and muons. For electrons, the energy scale uncertainty is estimated from $Z \rightarrow ee$ events and found to be $\pm 0.4\%$ ($4e$), $\pm 0.2\%$ ($2e2\mu$) and negligible for $2\mu2e$. For low E_T electrons, this estimate is verified with $J/\psi \rightarrow ee$ events. Uncertainties due to final-state radiation and background contamination are less than 0.1%. Similarly for final states with muons, large MC samples of $J/\psi \rightarrow \mu\mu$, $\Upsilon \rightarrow \mu\mu$ and $Z \rightarrow \mu\mu$ decays are used. Consequently, the mass uncertainty due to muon momentum uncertainties is estimated with $\pm 0.2\%$ (4μ) and $\pm 0.1\%$ ($2\mu2e$).

Categorization: Event categorization uncertainties are most relevant for the “+2 jets” and “+1 lepton” categories. For example, the structure of the underlying event or the jet energy scale affect whether an event *migrates* into the “+2 jets” or “+1 lepton” categories. The effect on the signal yields of these systematics on those categories is shown in table 2.4. For the +1 lepton category, the contribution from jet misidentification as lepton is small compared to the overall ggF uncertainty.

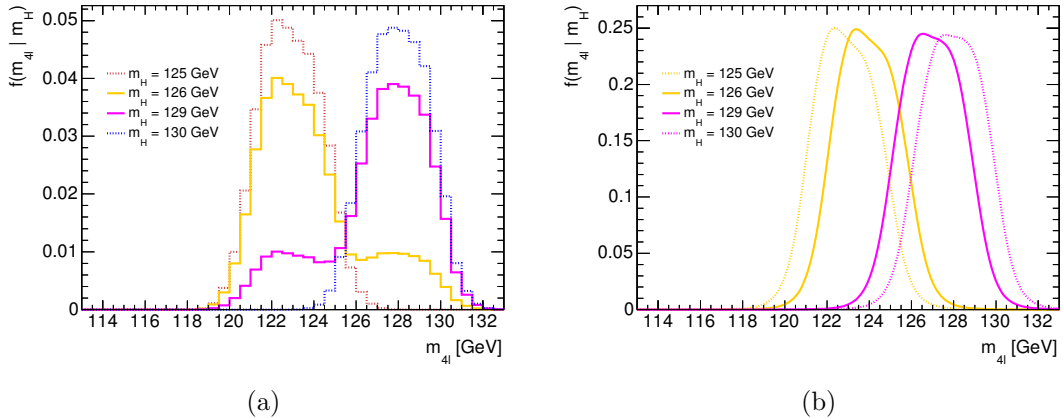


Figure 2.8: Comparison of (a) vertical and (b) horizontal interpolation for peaked shapes using a toy model. The dotted graphs are inputs and the solid graphs are outputs of the interpolation. The shapes are normalized to one.

2.5 $H \rightarrow ZZ^* \rightarrow 4\ell$ Signal Modeling

The shapes of probability density functions $f(x|\boldsymbol{\alpha})$ as introduced in section 1.5 are obtained using samples from fully simulated MC simulations. In 2011 in the absence of any hint for a signal, the $H \rightarrow ZZ^* \rightarrow 4\ell$ analysis group in ATLAS generated Higgs boson signal events for fixed m_H hypotheses in steps of 5 GeV. The generated events were all simulated in ATLAS’s full detector simulation. The event selection procedure above was then applied to all samples, producing weighted samples in m_{4l} . One-dimensional histograms in the m_{4l} range from 0 to 1 TeV with 2,000 bins were filled to represent signal shapes for all the m_H hypotheses for which MC simulations were available. A similar procedure was applied to build histograms representing distributions of background events.

As a first step to improve on the sampling density in m_H , the interpolation algorithm from [113] was applied to existing distributions to obtain shapes for intermediate fixed m_H . This algorithm is a “horizontal” interpolation algorithm

in the sense that it shifts peaked features of distributions. Alternatively, taking a weighted average of distributions is an example of a “vertical” interpolation. The two types of interpolations are shown in figure 2.8.

To improve the signal model further, it is useful to reconsider and review the available options to construct signal shapes in m_{4l} .

Histograms: ATLAS has developed good expertise for modeling binned probability density functions with histograms using the `HistFactory` tool [114]. It provides a clean interface to build statistical models from input histograms containing samples from expensive simulations. When the simulation becomes too expensive and only few simulated events are available, the shapes from histograms suffer from statistical bin-to-bin uncertainties; that is the fluctuation of the number of simulated events in a single bin. This can be taken into account by including a Poisson uncertainty for every bin. It introduces a nuisance parameter for every bin and is not feasible for models with more than a few hundred bins.

Analytic Functions: An alternative is to describe a shape using an analytic function fitted to MC samples. Usually, it has less degrees of freedom than a binned model making it less susceptible to statistical fluctuations. At the same time, the analytic function has to be flexible enough not only to accommodate the nominal shape but also all changes in the shape due to systematic uncertainties. It is also not guaranteed that the same form is still applicable when the event selection changes. This is particularly important when the shape has been determined empirically. In general, it is difficult to quantify the tension between an analytic shape and unbinned MC points. For example, tools like a “spurious signal term” [115] have been used to account for the fact that the background shape might look more like the signal term than the analytic shape allows for. This is a particular fix that

only applies when searching for a signal, but not when measuring it.

Kernel Density Estimates: There is another alternative to model the signal shape, and that is using kernel density estimates for example with KEYS [116]. KEYS uses variable width kernels that are wider for regions with fewer MC samples and narrower in regions with more MC samples. This produces smooth shapes where histograms have large statistical fluctuations while keeping the full structure of the shapes in regions that are more densely sampled. Kernel density estimates do not discretize the observable space (no bin boundaries) and can be continuously shifted.

Generally, the method of choice to parametrize a Higgs boson signal in m_H depends on the process and the mass resolution. The shape can be modeled by histograms for low mass resolution channels, and by analytic functions or kernel densities for high mass resolution processes. The choice of the interpolation algorithm depends on whether the probability distribution functions are binned or unbinned.

Once the signal shapes are obtained, a comprehensive model of signals and backgrounds has to be build that includes the responses of the yields and shapes to systematic uncertainty variations, e.g. with `HistFactory` for binned models.

2.5.1 An Improved Model

The starting point are the unbinned MC samples for discrete set of hypothesized Higgs boson masses. The “traditional” method is to create histograms and use a tool like `HistFactory` to create separate models for each parameter point.

Continuous Parametrization of Signal Normalizations and Systematic Uncertainties: The shapes in m_{4l} are pdfs and as such normalized to unity.

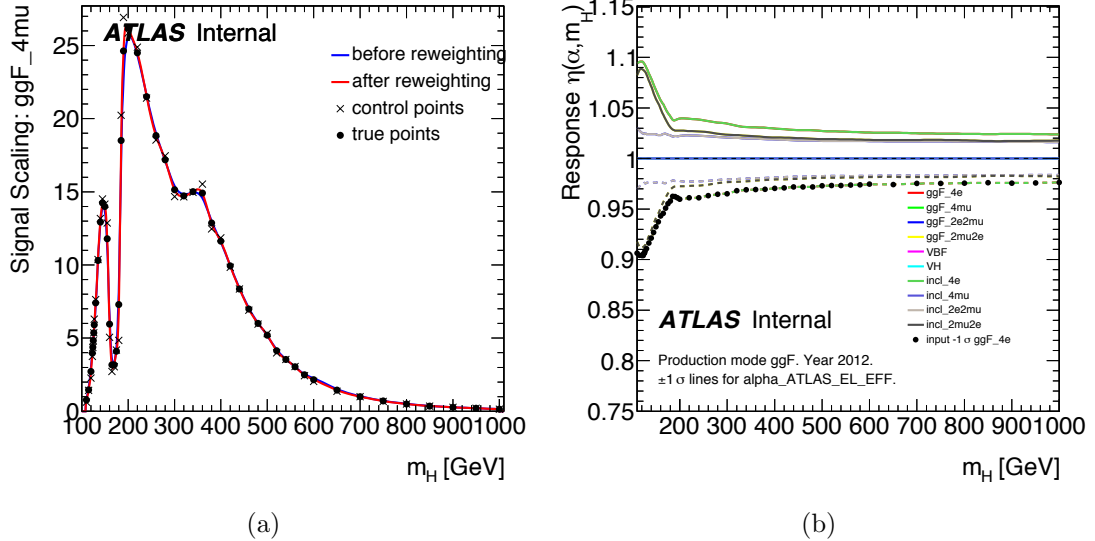


Figure 2.9: B-spline interpolations for (a) the expected number of events and (b) systematic uncertainties in m_H . Input values were determined from MC samples with full detector simulations at fixed values of m_H .

The interpolation of the expected number of events ν as a function of m_H is handled separately. An interpolation using B-splines is used as shown in figure 2.9(a). Systematic uncertainties that affect ν are implemented as in `HistFactory` models. Responses η to Higgs mass dependent systematic uncertainties are obtained from simulations at fixed values of m_H and intermediate response values are obtained from B-splines as shown in figure 2.9(b).

Systematic uncertainties like energy and momentum scale uncertainties that shift the overall signal shape can be applied directly to KEYS pdfs as shown in figure 2.10.

Signal Shapes: For this method, KEYS pdfs are created for every signal sample. They can be shifted continuously in m_{4l} . This allows to make use of simple proportionality relations between parameters and observables. Here, m_H

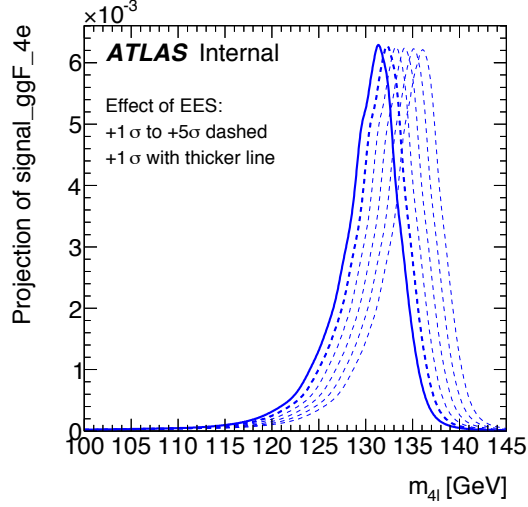


Figure 2.10: Effect of changing an energy scale on the shape of the $4e$ distribution in m_{4l} in arbitrary units.

and events x in m_{4l} are related by

$$f(x \mid m_H + \Delta) \approx f(x - \Delta \mid m_H) \quad .$$

An advantage of this method is that there is no assumption on the shape of $f(x \mid m_H)$.

Every fully simulated parameter point j with $m_H = m_j$ is described by a kernel density estimate (kde) of the form

$$f_j(x) = \frac{1}{n_j} \sum_{e=1}^{n_j} \frac{1}{h_e} K\left(\frac{x - x_{je}}{h_{je}}\right) .$$

Here, we want to use kdes f_j that can be shifted continuously in x by $\Delta_j = m_H - m_j$.

Each density

$$f_j(x \mid \Delta_j) = \frac{1}{n_j} \sum_{e=1}^{n_j} \frac{1}{h_{je}} K\left(\frac{x - x_{je} - \Delta_j}{h_{je}}\right)$$

is based on n_j kernels K at the simulated data points x_{je} and is using an adaptive

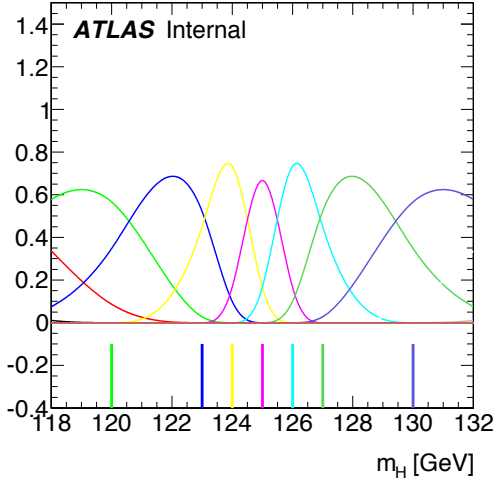


Figure 2.11: Third order B-spline basis functions that are used as weights.

bandwidth parameter h_{je} to apply narrower kernels in regions of high density and wider kernels in regions of low density. To increase performance, the shapes of the KEYS pdfs can be cached or calculated from k -d trees.

To obtain the signal shape at m_H , all f_j are first shifted by Δ_j and then interpolated according to

$$f_{\text{total}}(x \mid m_H) = \sum_j w_j(m_H) f_j(x \mid \Delta_j)$$

where the coefficients $w_j(m_H)$ are B-spline basis functions as shown in figure 2.11. B-splines are fast to evaluate, have local support, are positive by definition and can be evaluated at various orders to adjust the degree of “smoothing” and the size of the local support.

The model can be verified by leaving out a signal sample and comparing the interpolated shape to the shape obtained directly from the sample. This is shown in figure 2.12 for the extreme case of having MC samples only at 120 GeV and

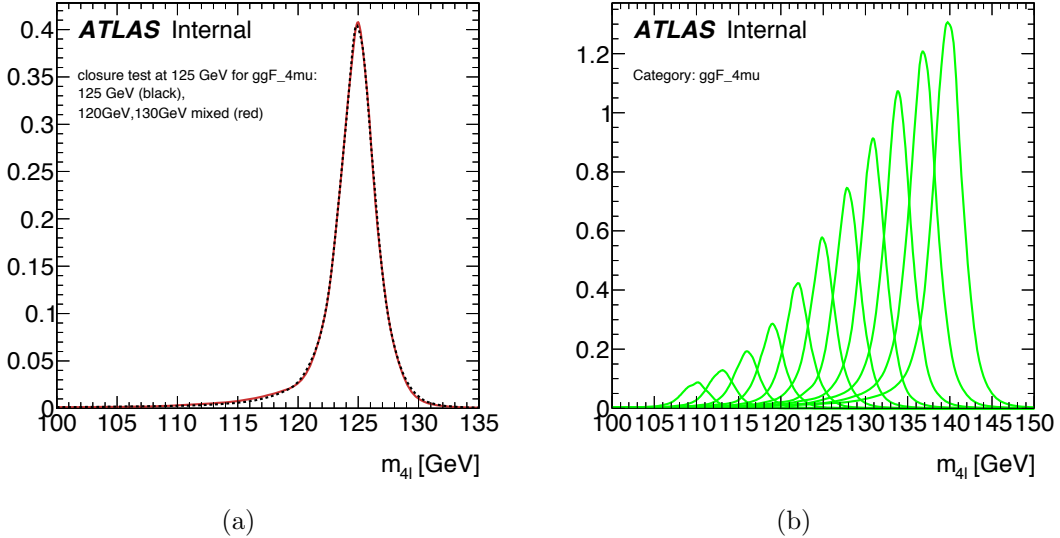


Figure 2.12: (a) Verification of the method. (b) Scan across m_H . Both plots are in arbitrary units.

130 GeV and trying to interpolate the shape at 125 GeV. Even in this case, the agreement is very good. Figure 2.12(b) shows a scan in m_H of the signal model for values that are interpolated in the model and were not available from MC.

2.5.2 Multivariate Kernel Density Estimates

The generalization to multivariate fixed kernel density estimates is given in [117], where the bandwidth matrix H is introduced. For multivariate product kernels, h and H are related by

$$H = h^2 \mathbf{1} .$$

A general form for a kde is then

$$f(x; H) = \frac{1}{n} \sum_{e=1}^n K_H(x - x_e) \quad (2.6)$$

where H is a bandwidth matrix (symmetric positive definite), K and K_H are related by

$$K_H(x) = |H|^{-1/2} K(H^{-1/2}x)$$

and K is a kernel (1-dimensional or multivariate) satisfying

$$\int K(x)dx = 1.$$

To construct an adaptive bandwidth matrix that depends on the function value f , one needs to find a unitless scale factor first. For probability density functions, the d -dimensional volume is unitless:

$$1\text{-dimensional: } \sigma_x f(x)$$

$$2\text{-dimensional: } \sigma_x \sigma_y f(x, y)$$

$$3\text{-dimensional: } \sigma_x \sigma_y \sigma_z f(x, y, z)$$

...

$$d\text{-dimensional: } \sqrt{\det(\Sigma)}f$$

Combining this scale factor with the argument given in [118] that was specific to product kernels, the more general expression for adaptive width kernel density estimates is

$$H = \left(\frac{4}{d+2} \right)^{\frac{2}{d+4}} \left(\frac{1}{n} \right)^{\frac{2}{d+4}} \frac{\Sigma}{\sqrt{\det(\Sigma)} f_0} .$$

This bandwidth matrix H and the zero'th order estimate of f , f_0 , are used to obtain f_1 which then can be used again to obtain better approximations of f iteratively.

The presented method is well suited to model signals with high resolution. It is fast to evaluate and allows the continuous parametrization of the shape directly in the model. It does not assume a particular shape of the signal.

I have used the one-dimensional form of this method since 2012 shortly after the discovery to provide the signal model for the official ATLAS $H \rightarrow ZZ^* \rightarrow 4\ell$ analysis. The results are significantly improved compared to previously used techniques which is discussed in section 4.1. Comparisons of the final results between the old and new signal models are shown in figure 2.13.

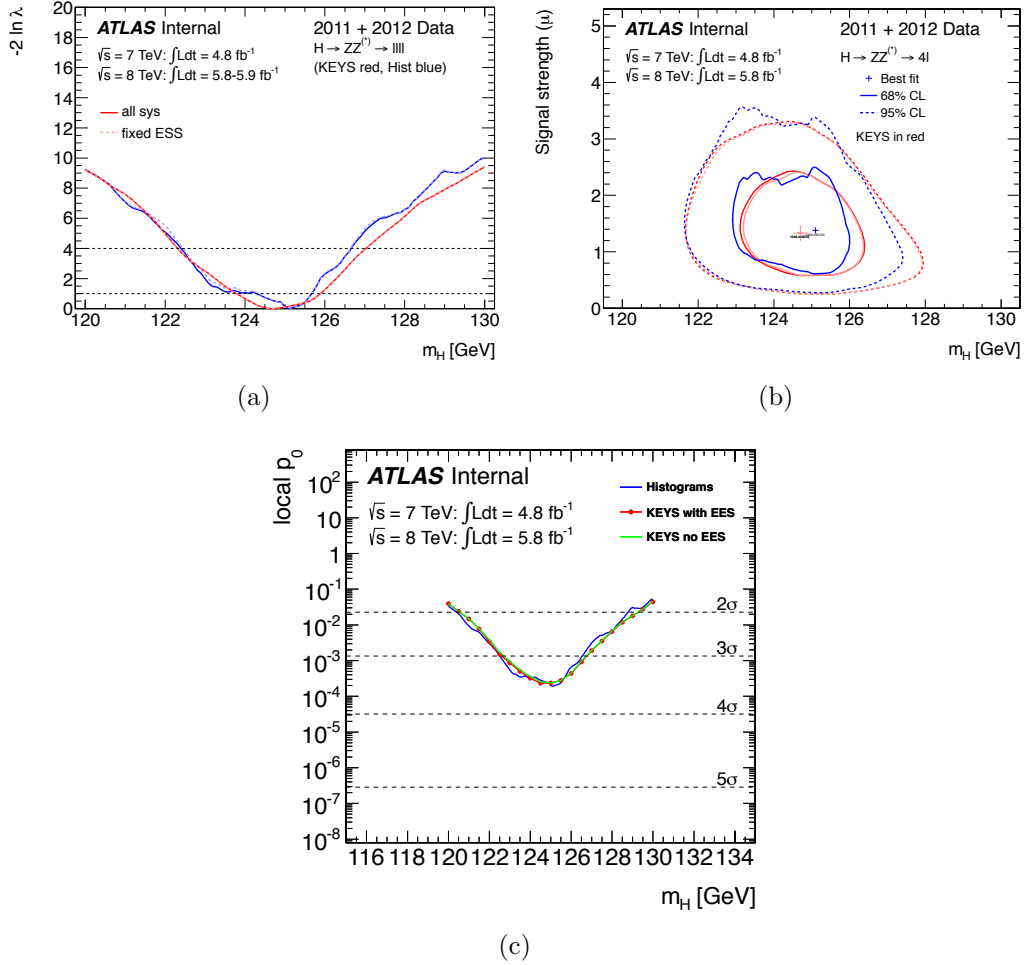


Figure 2.13: Improvements in the final result due to the new signal model (red) over the old signal model (blue) for (a) the mass measurement, (b) the confidence intervals in the (μ, m_H) plane and (c) the local p_0 values.

Chapter 3

Discovery

This chapter discusses the transition from excluding larger and larger ranges of the hypothesized Higgs boson mass to discovering a new particle in the unexcluded range. It is based on the conference notes and papers [119, 120, 121, 12, 37, 122], the internal note [11] and the presentation [123].

3.1 Statistical Methods

Tests of the values of μ are done for fixed Higgs masses m_H using the profile likelihood ratio $\lambda(\mu)$ [124]. The full likelihood fit to the data is used and includes all parameters that describe systematic uncertainties (nuisance parameters) and their correlations. The profile likelihood ratio is

$$\lambda(\mu) = \frac{L(\mu, \hat{\boldsymbol{\theta}}(\mu))}{L(\hat{\mu}, \hat{\boldsymbol{\theta}})} \quad (3.1)$$

where $\hat{\mu}$ and $\hat{\boldsymbol{\theta}}$ are maximum likelihood estimates of μ and $\boldsymbol{\theta}$ and $\hat{\boldsymbol{\theta}}(\mu)$ is the conditional maximum likelihood estimate of $\boldsymbol{\theta}$ depending on μ .

The physical range of μ is $\mu \geq 0$. However, it is convenient to allow negative values of μ in the model and to adjust the test statistic instead. Negative values of $\hat{\mu}$ correspond to deficits in data with respect to the background-only model. It is equivalent to impose $\mu \geq 0$ in the model or to impose the constraint in the likelihood ratio, i.e.

$$\tilde{\lambda}(\mu) = \begin{cases} \frac{L(\mu, \hat{\boldsymbol{\theta}}(\mu))}{L(\hat{\mu}, \hat{\boldsymbol{\theta}})} & \hat{\mu} \geq 0 \\ \frac{L(\mu, \hat{\boldsymbol{\theta}}(\mu))}{L(0, \hat{\boldsymbol{\theta}}(0))} & \hat{\mu} < 0 \end{cases} \quad (3.2)$$

The test statistic used to quantify an excess above the background-only hypothesis with $\mu = 0$ while considering the alternative hypothesis with $\mu > 0$ is

$$\tilde{q}_0 = \begin{cases} -2 \ln \lambda(0) & \hat{\mu} > 0 \\ +2 \ln \lambda(0) & \hat{\mu} \leq 0 \end{cases} \quad (3.3)$$

which also allows for the quantification of deficits (p-values larger than 0.5).

The test statistic \tilde{q}_μ is used to set upper limits on μ . The test is whether signal events are produced at a rate corresponding to μ against the alternative of being produced at a smaller rate:

$$\tilde{q}_\mu = \begin{cases} -2 \ln \tilde{\lambda}(\mu) & \hat{\mu} \leq \mu \\ +2 \ln \tilde{\lambda}(\mu) & \hat{\mu} > \mu \end{cases} \quad (3.4)$$

Ensembles of \tilde{q}_0 and \tilde{q}_μ can be generated from the probabilistic model. The model is hierarchical in the sense that first, the outcome of previous measurements is generated in the form of the global observables \mathcal{G} and second, the data set \mathcal{D}_{com} is generated for this set of global observables.

Upper limits are based on the CL_s technique [125]. A parameter point is regarded as excluded at the 95% CL when the value of CL_s falls below 5% where

$$CL_s(\mu) = \frac{p_\mu}{1 - p_b} \quad (3.5)$$

and p_μ and p_b are p-values obtained using the \tilde{q}_μ test statistic.

For the discovery scenario, the p-value under the background-only hypothesis is usually converted into a Gaussian significance Z which is defined as

$$Z = \Phi^{-1}(1 - p_0) \quad (3.6)$$

where Φ^{-1} is the inverse of the cumulative distribution of a Normal distribution.

The global p_0 value is corrected for the “look elsewhere” effect using the method in [126].

Statistical tests are performed in discrete steps in m_H . The results are based on asymptotic approximations [124] that were validated using the methods from [37].

All combinations of sub-channels for a particular Higgs boson decay and the full combination of all search channels are based on the signal strength μ and identify correlated nuisance parameters.

3.2 $H \rightarrow \gamma\gamma$

The $H \rightarrow ZZ^* \rightarrow 4\ell$ channel was discussed in detail in chapter 2. The $H \rightarrow \gamma\gamma$ channel is summarized here for the purpose of explaining the combination procedure.

In this channel, Higgs mass hypotheses are considered in the range between

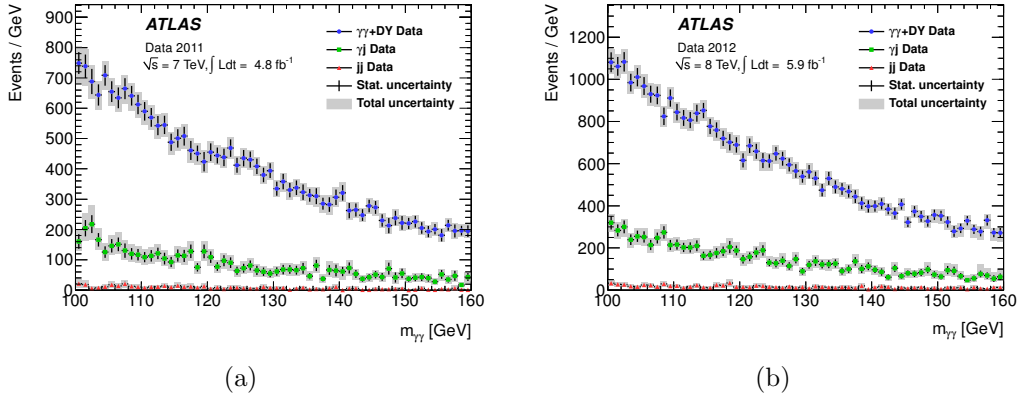


Figure 3.1: MC studies for $H \rightarrow \gamma\gamma$ at (a) $\sqrt{s} = 7$ TeV and (b) $\sqrt{s} = 8$ TeV.

110 GeV and 150 GeV. The SM diphoton production ($\gamma\gamma$) is the dominant background. There are also contributions from $\gamma + jet$ and $jet + jet$ which are commonly called γj and jj where jets are mis-identified as photons. Another contribution comes from the Drell-Yan process. Using MC events, the contributions from these processes in the $m_{\gamma\gamma}$ spectrum is studied and shown in figure 3.1. For all results, the datasets and analyses for $\sqrt{s} = 7$ TeV and $\sqrt{s} = 8$ TeV have been combined. The analyses do include dedicated categories with enhanced sensitivity to VBF production. VBF processes have two additional forward jets in the event.

Events are selected using a diphoton trigger which requires two clusters of energy depositions in the electromagnetic calorimeter. At $\sqrt{s} = 7$ TeV, the E_T threshold for both clusters was 20 GeV and at $\sqrt{s} = 8$ TeV they were (35, 25) GeV for the (leading, sub-leading) clusters. The clusters are also required to satisfy loose criteria for their shapes as expected from photon initiated electromagnetic showers. The trigger efficiency for the selected events is larger than 99%. The event has to contain a reconstructed vertex with two or more associated tracks with $p_T > 0.4$ GeV and two photon candidates.

A photon candidate has to be inside $|\eta| < 2.37$ excluding the region between barrel and end-cap at $1.37 < |\eta| < 1.52$. Some photons convert to electron-positron pairs with the material of the inner detector and in that case, there have to be one or two tracks associated to the calorimeter clusters. For $E_T > 30$ GeV, the reconstruction efficiency is 97%. Photon candidates are required to have $E_T > 40$ GeV for the leading and $E_T > 30$ GeV for the sub-leading photon.

Photons loose energy when they interact with the material of the detector. The material that is on a photon's path before being detected is called upstream material and energy losses have to be accounted for. There is also energy leakage outside of what is estimated to be the photon's energy cluster. MC simulations are used to calibrate these two effects for converted and unconverted photons separately. An η -dependent and data-driven correction of the order of $\pm 1\%$ using $Z \rightarrow e^+e^-$ events is applied.

For $\sqrt{s} = 7$ TeV, variables that describe shower shapes in the electromagnetic calorimeter and energy leakage into the hadronic calorimeter are fed into a neural network. The operating point was chosen such that it has similar jet rejection performance as a cut-based analysis, which results in a higher photon identification efficiency. For the newly recorded data at $\sqrt{s} = 8$ TeV, a cut-based and pile-up robust selection was used. The photon identification efficiency was in the range of 85% to 95%.

Jet backgrounds were further reduced using an energy isolation requirement. In a cone of $\Delta R < 0.4$ around the photon candidate and excluding the core range $(0.125, 0.175)$ in $(\Delta\eta, \Delta\phi)$, the deposited energy must be less than 4 GeV. The agreement between data and MC simulations for this isolation was checked using $Z \rightarrow e^+e^-$ and $Z \rightarrow l^+l^-\gamma$ events and the difference was taken as a systematic

uncertainty.

The invariant mass is constructed by using the energy deposits in the calorimeter from the two photons and the angles ϕ and η from the positions of the photons in the calorimeter and the position of the primary vertex.

Determining the primary vertex for $\gamma\gamma$ events is fairly involved. The first piece of information that is used is the longitudinal segmentation of the electromagnetic calorimeter. This is also called *calorimeter pointing*. Then there are the parameters of the beam spot and the vertices with their $\sum p_T^2$ of the associated tracks. This information is combined in a likelihood function. In addition, the reconstructed conversion vertex is used in the $\sqrt{s} = 7$ TeV analysis. Just using calorimeter pointing alone, the resolution along the z axis for the position of the primary vertex is ≈ 15 mm which improves to ≈ 6 mm for events with two reconstructed converted photons. For events with jets as required by the VBF optimized 2-jet category, the identification of the primary vertex is further improved due to inner detector tracks.

Using this selection, 59,039 diphoton candidates were observed in 4.8 fb^{-1} and 5.9 fb^{-1} at $\sqrt{s} = 7$ TeV and $\sqrt{s} = 8$ TeV with $m_{\gamma\gamma}$ between 100 GeV and 160 GeV of which 190.1 are expected to be signal events for a Higgs boson with mass $m_H = 126.5$ GeV.

To increase sensitivity, the events are separated into 10 mutually exclusive categories. They have different mass resolutions and different signal-to-background ratios. One of the ten categories is just for the VBF enhanced selection on two jets. The remaining nine categories are combinations of η regions of the two photons, the p_{Tt} and whether the photons are converted or not. p_{Tt} is a property of the

diphoton system and defined by

$$p_{\text{Tr}} = \frac{|(\mathbf{p}_{\text{T}}^{\gamma_1} + \mathbf{p}_{\text{T}}^{\gamma_2}) \times (\mathbf{p}_{\text{T}}^{\gamma_1} - \mathbf{p}_{\text{T}}^{\gamma_2})|}{|\mathbf{p}_{\text{T}}^{\gamma_1} - \mathbf{p}_{\text{T}}^{\gamma_2}|} \quad (3.7)$$

which is a component of the diphoton \mathbf{p}_{T} .

For the VBF enhanced 2-jet category, jets that are most likely coming from a VBF topology have to be identified. The anti- k_t algorithm [111] with $R = 0.4$ is used. For this category, two jets with $|\eta| < 4.5$ and $p_{\text{T}} > 25$ GeV are required. For the $\sqrt{s} = 8$ TeV analysis and in the range $2.5 < |\eta| < 4.5$, the p_{T} threshold is raised to 30 GeV. To suppress jets from pile-up, for jets that are inside the inner detector coverage of $|\eta| < 2.5$, the jet vertex fraction (JVF) has to be larger than 0.75, where JVF is the scalar sum of $p_{\text{T}}^{\text{track}}$ for tracks coming from the primary vertex versus the scalar sum of $p_{\text{T}}^{\text{track}}$ of all tracks of the jet. In addition and specific to the VBF topology, it is required that $\Delta\eta > 2.8$ between the two jets, that the invariant mass has to be larger than 400 GeV and that the azimuthal angle between the diphoton system and the 2-jet system is larger than 2.6. These cuts enhance the VBF process with respect to the other production processes such that about 70% of signal events come from the VBF process.

Of the remaining nine categories, there are “unconverted” categories with both photons unconverted, “converted” categories with at least one converted photon, “central” categories with both photons inside $|\eta| < 0.75$, “transition” categories with at least one photon in $1.3 < |\eta| < 1.75$ and “rest” categories with all remaining events that are neither “central” nor “transition”. Some categories are further divided into “low p_{Tt} ” and “high p_{Tt} ” with a threshold at $p_{\text{Tt}} = 60$ GeV. It was seen in MC studies that VBF, VH and $t\bar{t}H$ events have on average higher p_{Tt} than

background events. The overall selection efficiency is about 40%.

Modeling: For the signal, an analytic function is fitted to various MC samples to obtain its parameters for the shape. For the yield, theoretical calculations for ggF [127] are used and the destructive interference with $gg \rightarrow \gamma\gamma$ is taken into account. The analytic function is a Crystal Ball function [128] for the core of the distribution summed with a small and wide Gaussian distribution to describe the tails.

The background shape is estimated from data in each category separately. It is expected to be a smoothly falling function in the absence of a signal. A set of analytic functions are tested on MC estimates to select the analytic form for each category. The parameters are then obtained from a fit to data excluding a window around the expected signal. The chosen functions for the various categories are a fourth-order Bernstein polynomial, an exponential of a second-order polynomial and an exponential function. The bias from constraining the shape to any of the analytic forms has been estimated from MC and control regions in data. In the final model, a signal-like term of constrained height, the *spurious signal term*, is included in each background model to account for the fact that the true background shape could look a bit more like signal than the chosen background shape.

A summarized version of all categories is shown in figure 3.2. This is a nice representation, but for all results, the full model with 10 categories was used.

Systematic uncertainties: The photon reconstruction and identification efficiency is the largest experimental uncertainty affecting the signal yield with $\pm 8\%$ for $\sqrt{s} = 7$ TeV and $\pm 11\%$ for $\sqrt{s} = 8$ TeV. This is estimated from data using electrons from Z decays and photons from $Z \rightarrow l^+l^-\gamma$ events. The second largest experimental uncertainty of $\pm 4\%$ comes from modeling pile-up. In addition, there

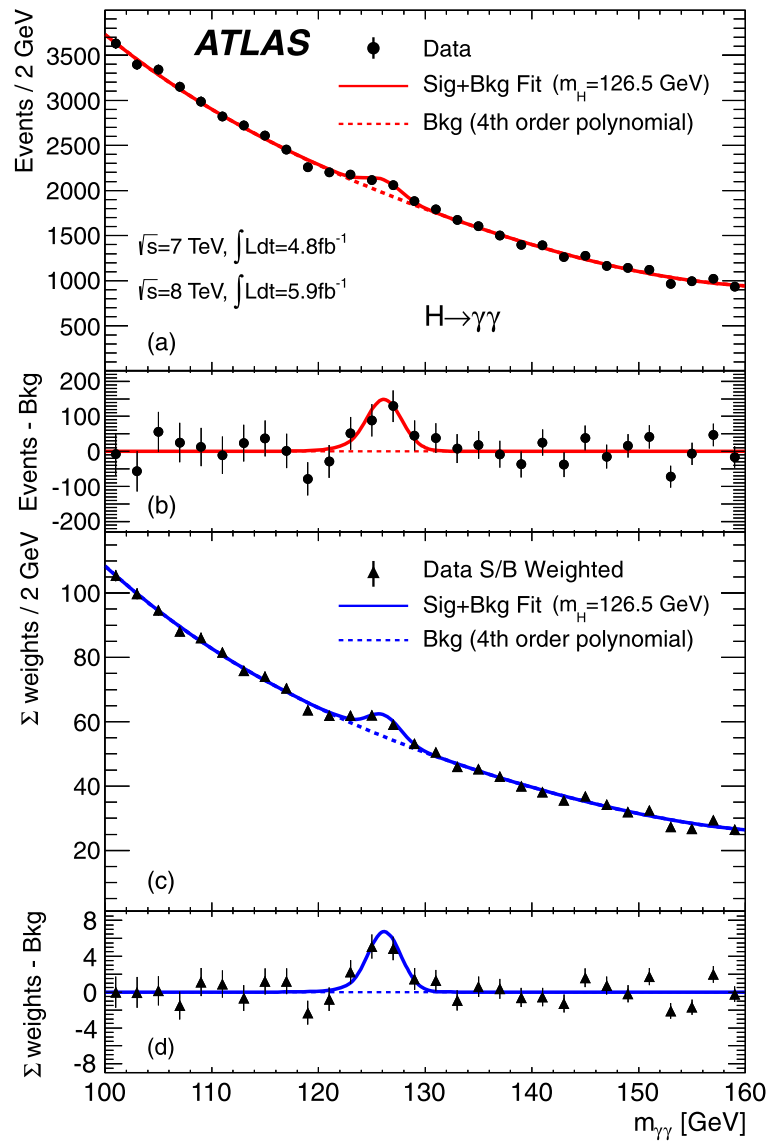


Figure 3.2: Invariant mass spectrum of $m_{\gamma\gamma}$ in $H \rightarrow \gamma\gamma$ decays.

is a trigger uncertainty of $\pm 1\%$, a photon isolation uncertainty of $\pm 0.4\%$ and $\pm 0.5\%$ for $\sqrt{s} = 7$ TeV and $\sqrt{s} = 8$ TeV and a luminosity uncertainty of $\pm 1.8\%$ and $\pm 3.6\%$ also for the two data taking periods respectively. In the 2-jet category, there is a large uncertainty due to the modeling of the underlying event of $\pm 6\%$ for the VBF process and $\pm 30\%$ for all other production processes.

A different set of uncertainties governs the composition of signal processes in each category. The imperfect knowledge about the amount of upstream material in front of the calorimeter is used to derive a migration uncertainty between the converted and unconverted categories of $\pm 4\%$. Similarly, the effect of pile-up on those two types of categories is $\pm 2\%$. The selection for the 2-jet category is sensitive to the jet energy scale which results in $\pm 19\%$ for the 2-jet category itself, but it also affects the other categories with up to $\pm 4\%$. The JVF cut for the $\sqrt{s} = 8$ TeV analysis comes with an uncertainty of $\pm 12\%$ for the signal yield in the 2-jet category. Furthermore, by using different PDFs and scales, the migration of events between categories is estimated to be $\pm 9\%$.

The mass measurement is also affected by systematic uncertainties. The largest contribution comes from the uncertainty on the energy resolution of the calorimeter with $\pm 12\%$. The uncertainty in the upstream material also affects the mass measurement with $\pm 6\%$ and pile-up affects it with about $\pm 4\%$.

3.3 $H \rightarrow WW^* \rightarrow \ell\nu\ell\nu$

Similarly as for the $H \rightarrow \gamma\gamma$ channel, the $H \rightarrow WW^* \rightarrow \ell\nu\ell\nu$ is only outlined here for the purpose of understanding the combination. For discovery only the “mixed flavor” analysis – that means $H \rightarrow WW^* \rightarrow e\nu\mu\nu$ – was included in the

combination.

Events with two oppositely charged leptons with different flavor and large transverse momentum are selected. In addition, there also should be large missing energy \cancel{E}_T , that is, a large momentum imbalance due to neutrinos from the leptonic W decay escaping detection. Irreducible backgrounds with real W bosons are non-resonant WW , $t\bar{t}$ and Wt . Reducible backgrounds are Drell-Yan, $W + jets$ and $W\gamma$ and to a lesser extent the di-boson processes $W\gamma^*$, $WZ^{(*)}$ and $ZZ^{(*)}$ where the additional leptons are not detected. The dominant backgrounds are estimated using data-driven techniques that normalize MC predictions, $W + jets$ is estimated in a fully data-driven way and smaller backgrounds are taken from MC simulations [12].

This channel focuses on the range of m_H between 110 GeV and 200 GeV. The $\sqrt{s} = 7$ TeV and $\sqrt{s} = 8$ TeV analyses are similar with the exception that some criteria have been tightened for 8 TeV to reduce the $W + jets$ component and to counteract the impact of the higher pile-up. The higher pile-up was one of the main reasons why the same flavor analyses were not included yet as the larger Drell-Yan background and worsened \cancel{E}_T resolution are problems for the analyses. Between the three analyses, the mixed flavor analysis provides more than 85% of the sensitivity.

The analysis uses single-muon and single-electron triggers with a p_T threshold at 24 GeV and selects leptons with $p_T > 25$ GeV and $p_T > 15$ GeV for the leading and sub-leading leptons. The dilepton system has to have an invariant mass of larger than 10 GeV. Two categories, called $e\mu$ and μe , are constructed depending on the flavor of the leading lepton.

Compared to the $H \rightarrow ZZ^* \rightarrow 4\ell$ analysis, more stringent lepton requirements

are applied. For electrons, both tracking and calorimetric information is used. For muons, candidates have to have a matching muon spectrometer and inner detector tracks which only has coverage inside $|\eta| < 2.5$. The isolation requirement for a lepton with transverse momentum p_T is that in a cone of $\Delta R = 0.3$ around the lepton there must be less than $[0.12, 0.20] \times p_T$ of charged particles transverse momentum and energy in topological clusters. The exact value depends on the lepton flavor and p_T of the lepton. The jet selection is the same as for the 2-jet category in $H \rightarrow \gamma\gamma$ with the exception that the jet vertex fraction has to be larger than 0.5.

The presence of neutrinos in the final state of the signal implies missing energy. \cancel{E}_T is the negative of the transverse momentum vector of all detected particles including clusters of energy in the calorimeter not associated to any reconstructed object. Usually the magnitude of \cancel{E}_T , \cancel{E}_T , is used in analyses. Neutrinos inside jets produce missing energy that is in the direction of a jet. However, in this analysis, \cancel{E}_T is supposed to discriminate against events without neutrinos from the hard interaction. The difference between the two scenarios is the angle between \cancel{E}_T and the closest reconstructed object. To suppress \cancel{E}_T from neutrinos in jets or mismeasured jets, the quantity $\cancel{E}_{T,\text{rel}}$ is introduced and defined by

$$\cancel{E}_{T,\text{rel}} = \cancel{E}_T \sin \Delta\phi_{\min} \quad \text{with} \quad \Delta\phi_{\min} = \min(\Delta\phi, \pi/2) \quad (3.8)$$

where $\Delta\phi_{\min}$ is the angle in the transverse plane between \cancel{E}_T and the closest lepton or jet with $p_T > 25$ GeV. The threshold for \cancel{E}_T in this analysis is 25 GeV.

The analysis is split into categories depending on the number of additional jets as this is one of the most relevant factors for the composition of the background.

In the 0-jet category, signal events are mostly from ggF and background events are mostly from WW . In the 2-jet category, which is inclusive and also includes three or more jets, the contribution from VBF to the signal is larger and the background is mostly $t\bar{t}$. The discriminating variable in all categories is m_T [129] which is defined as

$$m_T = \sqrt{(E_T^l + \cancel{E}_T)^2 - |\boldsymbol{p}_T^l + \cancel{\boldsymbol{E}}_T|^2} \quad (3.9)$$

where the transverse energy of the two-lepton system is $E_T^l = \sqrt{|\boldsymbol{p}_T^l|^2 + m_l^2}$.

Due to the V–A structure of weak interactions and the SM Higgs boson being a scalar, there are spin correlations in the WW system that favor smaller angular separations between the two final state leptons [130]. Therefore, a cut with $|\Delta\phi_{ll}| < 1.8$ is applied to enhance the signal with respect to background. In the 2-jet channel, the dilepton mass must be less than 80 GeV and for the 0-jet and 1-jet channel it must be less than 50 GeV.

To reduce Drell-Yan background in the 0-jet category, the transverse momentum of the dilepton system must be larger than 30 GeV.

The 1-jet channel suffers from backgrounds from top quark production. Therefore, events with b-tagged jets are removed. The algorithm for b-tagging uses a neural network exploiting features in the topology of weak decays of b- and c-hadrons [131]. Some events contain jets that have a p_T below the threshold for jet counting. This is a particular problem for top background events. Those events usually also contain a larger total transverse momentum p_T^{tot} which is

$$p_T^{\text{tot}} = |\boldsymbol{p}_T^{l1} + \boldsymbol{p}_T^{l2} + \boldsymbol{p}_T^j + \cancel{\boldsymbol{E}}_T| \quad (3.10)$$

and therefore a cut is introduced to keep $p_T^{\text{tot}} < 30$ GeV. Another background

process is $Z \rightarrow \tau\tau$. Assuming that the observed leptons are coming from τ decays and the missing energy only comes from neutrinos associated with these decays, the invariant mass $m_{\tau\tau}$ is constructed if the collinear approximation gives a real solution. If it does, events are required to have $|m_{\tau\tau} - m_Z| > 25$ GeV.

The 2-jet selection is similar to the 1-jet selection with the additional jets included in the sum for p_T^{tot} . To enhance the VBF contribution, the two highest p_T jets – called tag jets – have to have $|\Delta y_{jj}| > 3.8$ and $m_{jj} > 500$ GeV, and events with additional jets with $p_T > 20$ GeV with rapidity $y_{j1} < y < y_{j2}$ are rejected.

Systematic uncertainties: The main experimental uncertainties are the jet energy scale (JES) and jet energy resolution (JER), pile-up, \cancel{E}_T , b-tagging efficiency, the transfer factor for the $W + jets$ background and the integrated luminosity. The largest background modeling uncertainties are the normalization and modeling of the WW background, the top normalization and $W\gamma^*$ normalization. In the 2-jet category, statistical uncertainties from data and MC simulations dominate.

JES and JER are mostly responsible for migration of events between categories. The effect of JES variations is between $\pm 2\%$ and $\pm 9\%$ depending on p_T and η of the jet for $p_T > 25$ GeV and $|\eta| < 4.5$ [132]. For the signal yield, this means a variation of $\pm 7\%$ (0-jet) and $\pm 4\%$ (1-jet). The JER mostly affects the 1-jet channel and has an affect of $\pm 4\%$ on the signal yield and $\pm 2\%$ on the background yield. Pile-up is also JES dependent and is estimated to affect mostly the 1-jet channel with $\pm 4\%$ and $\pm 2\%$ for signal and background yields. The \cancel{E}_T measurement is also affected by JES as well as lepton momentum scale uncertainties. It also is sensitive to low p_T jets and low energy deposits in the calorimeter that do not have an associated reconstructed object. The impact on the signal and background yield

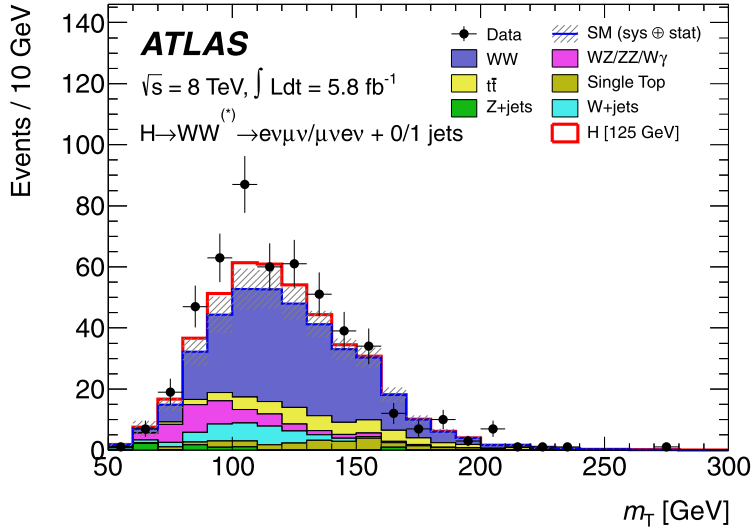


Figure 3.3: Transverse mass spectrum for $H \rightarrow WW^* \rightarrow e\nu\mu\nu$ and $H \rightarrow WW^* \rightarrow \mu\nu e\nu$ decays for the 0-jet and 1-jet category.

is estimated to be about 3%. The 1-jet channel is also sensitive to the b-tagging efficiency which has an impact of about 10% on the background. Due to differences in dijet and $W + jet$ events in the jet variables, the uncertainty on the yield of the $W + jets$ background is $\pm 40\%$ which results in a $\pm 5\%$ uncertainty for the total background. The integrated luminosity has an uncertainty of $\pm 3.6\%$.

The number of expected events for a SM Higgs boson with $m_H = 125$ GeV are 20 ± 4 signal events in the 0-jet category and 146 ± 16 expected background events. For the 1-jet and 2-jet categories, the expected signal events are 5 ± 2 and 0.34 ± 0.07 and for background 26 ± 6 and 0.35 ± 0.18 . The transverse mass spectrum for the 0-jet and 1-jet categories is shown in figure 3.3.

3.4 Combination

Various analyses that search for the Higgs boson are combined to form a more powerful model with increased sensitivity particularly to discover a new particle. The channels that entered the ATLAS combination in July 2012 are shown in table 3.1.

The common systematic uncertainties have to be correlated properly. The integrated luminosity is fully correlated across the channels. For analyses at $\sqrt{s} = 7$ TeV, this is a $\pm 3.9\%$ [142] in all yields except for the $H \rightarrow ZZ^* \rightarrow 4\ell$ and $H \rightarrow \gamma\gamma$ channels where a newer luminosity estimate was used in the input channel analysis and a $\pm 1.8\%$ [143] effect is included. Uncertainties that are related to final states that are the same across many analyses have to be correlated. Therefore, trigger and identification efficiencies for electrons and photons as well as electron and photon energy scales are fully correlated, which is particularly important for the combination of $H \rightarrow ZZ^* \rightarrow 4\ell$ and $H \rightarrow \gamma\gamma$. Similarly, uncertainties relating to muon reconstruction in the inner detector and the muon spectrometer are correlated. The correlation of jet energy scale and missing transverse energy depends on the kinematic selections and flavor compositions of the jets. Whereas light jet uncertainties are correlated across analyses, nuisance parameters describing heavy flavor jets in the $H \rightarrow b\bar{b}$ analysis are uncorrelated. With this dataset, various correlation schemes were tried for the jet components and gave negligible differences in the results. The \cancel{E}_T uncertainty has a correlated component from JES effects and an uncorrelated component due to low energy activity in the calorimeter that is not associated to reconstructed objects. Theory uncertainties in the Higgs production processes are particularly large and correlated across all analyses. The ggF signal yield changes by $^{+7\%}_{-8\%}$ due to uncertainty in the the QCD

Higgs Boson Decay	Subsequent Decay	Sub-Channels	m_H Range [GeV]	$\int \text{L} dt$ [fb $^{-1}$]	Ref.
2011 $\sqrt{s}=7$ TeV					
$H \rightarrow ZZ^*$	4ℓ	$\{4e, 2e2\mu, 2\mu2e, 4\mu\}$	110–600	4.8	[133]
	$\ell\ell\nu\bar{\nu}$	$\{ee, \mu\mu\} \otimes \{\text{low, high pile-up}\}$	200–280–600	4.7	[134]
	$\ell\ell q\bar{q}$	$\{b\text{-tagged, untagged}\}$	200–300–600	4.7	[135]
$H \rightarrow \gamma\gamma$	—	10 categories $\{p_{\text{TT}} \otimes \eta_\gamma \otimes \text{conversion}\} \oplus \{2\text{-jet}\}$	110–150	4.8	[136]
$H \rightarrow WW^*$	$\ell\nu\ell\nu$	$\{ee, e\mu, \mu e, \mu\mu\} \otimes \{0\text{-jet, 1-jet, 2-jet}\} \otimes \{\text{low, high pile-up}\}$	110–200–300–600	4.7	[137]
	$\ell\nu qq'$	$\{e, \mu\} \otimes \{0\text{-jet, 1-jet, 2-jet}\}$	300–600	4.7	[138]
	$\tau_{\text{lep}}\tau_{\text{lep}}$	$\{e\mu\} \otimes \{0\text{-jet}\} \oplus \{\ell\ell\} \otimes \{1\text{-jet, 2-jet, } VH\}$	110–150	4.7	[136]
$H \rightarrow \tau\tau$	$\tau_{\text{lep}}\tau_{\text{had}}$	$\{e, \mu\} \otimes \{0\text{-jet}\} \otimes \{E_{\text{T}}^{\text{miss}} < 20 \text{ GeV}, E_{\text{T}}^{\text{miss}} \geq 20 \text{ GeV}\}$ $\oplus \{e, \mu\} \otimes \{1\text{-jet}\} \oplus \{\ell\} \otimes \{2\text{-jet}\}$ $\tau_{\text{had}}\tau_{\text{had}}$	110–150	4.7	[139]
	$Z \rightarrow \nu\nu$	$E_{\text{T}}^{\text{miss}} \in \{120 - 160, 160 - 200, \geq 200 \text{ GeV}\}$	110–130	4.6	[133]
$VH \rightarrow Vbb$	$W \rightarrow \ell\nu$	$p_{\text{T}}^W \in \{< 50, 50 - 100, 100 - 200, \geq 200 \text{ GeV}\}$	110–130	4.7	[140]
	$Z \rightarrow \ell\ell$	$p_{\text{T}}^Z \in \{< 50, 50 - 100, 100 - 200, \geq 200 \text{ GeV}\}$	110–130	4.7	[141]
2012 $\sqrt{s}=8$ TeV					
$H \rightarrow ZZ^*$	4ℓ	$\{4e, 2e2\mu, 2\mu2e, 4\mu\}$	110–600	5.8	[133]
$H \rightarrow \gamma\gamma$	—	10 categories $\{p_{\text{TT}} \otimes \eta_\gamma \otimes \text{conversion}\} \oplus \{2\text{-jet}\}$	110–150	5.9	[136]
$H \rightarrow WW^*$	$e\nu\mu\nu$	$\{e\mu/\mu e\} \otimes \{0\text{-jet, 1-jet, 2-jet}\}$	110–200	5.8	[141]

Table 3.1: Overview of channels entering the combination during the discovery in July 2012 [12]. Some m_H ranges are split due to different optimization applied in each range.

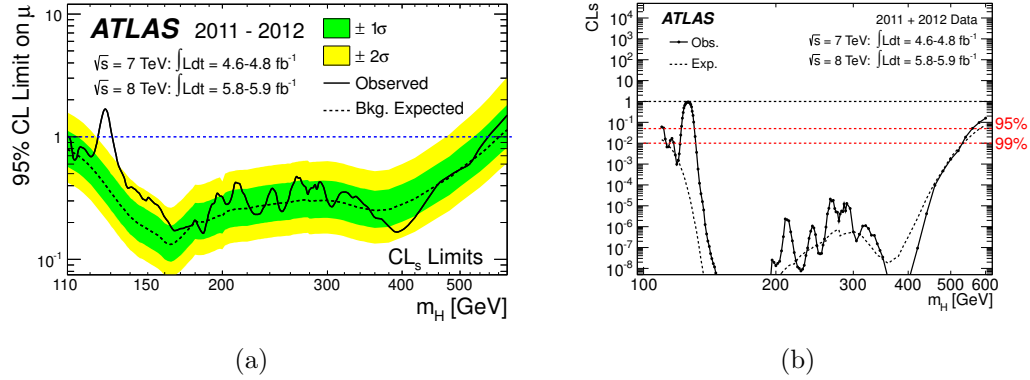


Figure 3.4: Exclusion ranges from the combination in July 2012. (a) shows the excluded signal strength at 95% CL as a function of m_H and (b) shows the CL to exclude a signal strength of $\mu = 1$ as a function of m_H .

scale for $m_H = 125$ GeV, $\pm 1\%$ for VBF and VH and $^{+4\%}_{-9\%}$ for $t\bar{t}H$ [1, 60]. Also the predicted branching ratios come with an uncertainty of $\pm 5\%$. The parton distribution functions of the proton at $\sqrt{s} = 7$ TeV and $\sqrt{s} = 8$ TeV also come with an uncertainty of $\pm 8\%$ for mostly gluon-initiated processes like ggF and $t\bar{t}H$ and $\pm 4\%$ for the quark-initiated processes VBF and VH [87, 86, 88, 89]. Interference effects with other SM processes and off-shell Higgs boson production are accounted for in an uncertainty of $\pm 150\% \times (m_H/\text{TeV})^3$ which results in a $\pm 4\%$ uncertainty at $m_H = 300$ GeV and smaller below that.

Excluded parameter space: Higgs masses are excluded at the 95% CL when the CL_s value at the SM signal strength $\mu = 1$ drops below 5%. The result is shown in figure 3.4(a). The expected exclusion range is from $m_H = 110$ GeV up to 582 GeV whereas the observed exclusion range is 111 GeV to 559 GeV with the important exception of 122 – 131 GeV. A large range is excluded even at the 99% CL as shown in figure 3.4(b).

Observation of an excess: The $H \rightarrow ZZ^* \rightarrow 4\ell$ and $H \rightarrow \gamma\gamma$ have fully reconstructible final states which results in a high resolution for the Higgs boson mass

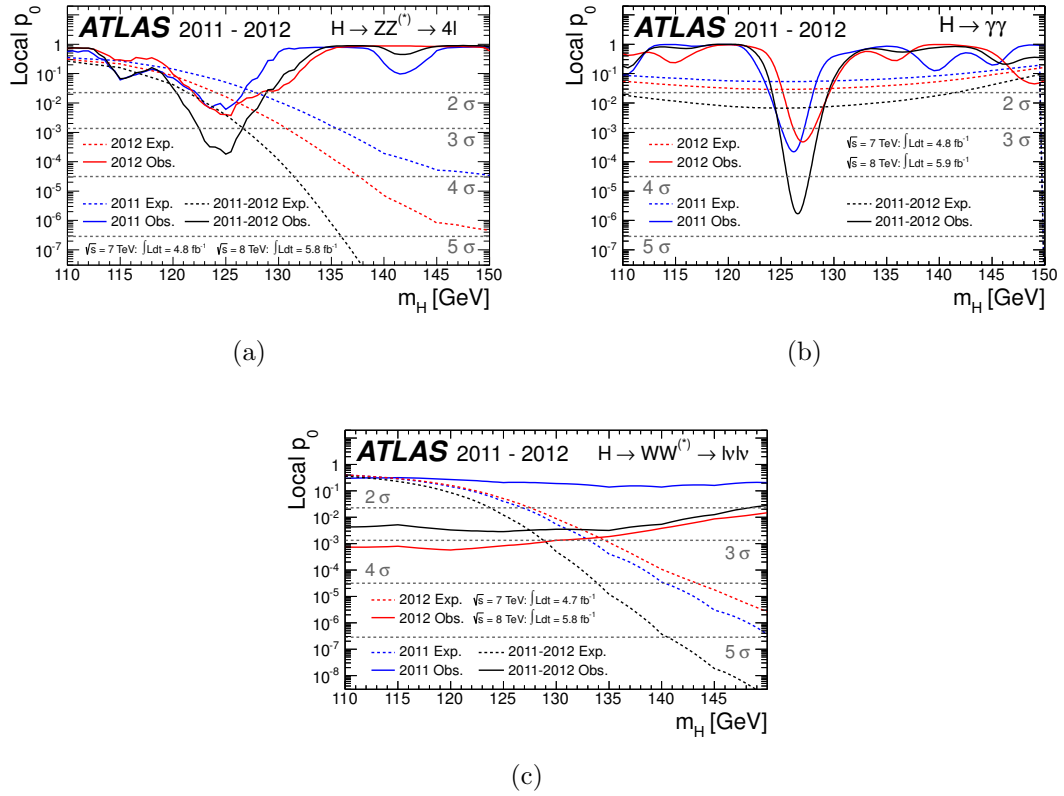


Figure 3.5: Local p_0 values for the channels (a) $H \rightarrow ZZ^* \rightarrow 4\ell$, (b) $H \rightarrow \gamma\gamma$ and (c) $H \rightarrow WW^* \rightarrow \ell\nu\ell\nu$.

parameter. Neutrinos in the final state of $H \rightarrow WW^* \rightarrow \ell\nu\ell\nu$ escape detection and decrease the mass resolution in this channel, although this channel is still highly sensitive to the signal. The p_0 values for the three channels are shown in figure 3.5 and the results of hypothesis tests of combined models in figure 3.6. These results are based on asymptotic approximations. At $m_H = 126.5$ GeV the local significance is largest with 6.0σ with an expectation of 4.9σ .

The asymptotic formulas are not strictly applicable when energy scale systematics are present. This effect was studied on earlier models where the generation of ensembles was still feasible and is shown in figure 3.7. This effect can also be

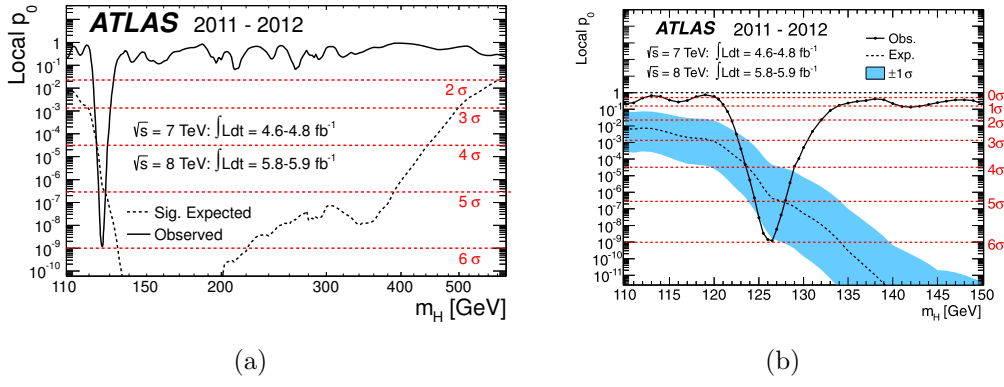


Figure 3.6: Combination results.

accounted for in the asymptotic equations using the approach described in [144] which reduces the local significance to 5.9σ . This significance is still local in the sense that it is obtained from a test with one specific Higgs boson mass. The global significance, that is the significance that such an excess can occur anywhere in the parameter range, is about 5.1σ when considering the full m_H range from $110 - 600$ GeV and about 5.3σ when only the range $110 - 150$ GeV is considered which is motivated from global fits to electroweak measurements.

Figure 3.8(a) shows also that there is power to measure the signal strength across the whole parameter range and that it is consistent with zero except around the excess, and figure 3.8(b) shows the breakdown by channel of the signal strength at $m_H = 126.0$ GeV.

3.5 Bayesian Checks on Limits

Upper limits using the CL_s method have the property that they are numerically equivalent to Bayesian upper limits (one-sided credibility intervals) with flat priors on the parameter of interest for the Gaussian and Poisson case. I constructed

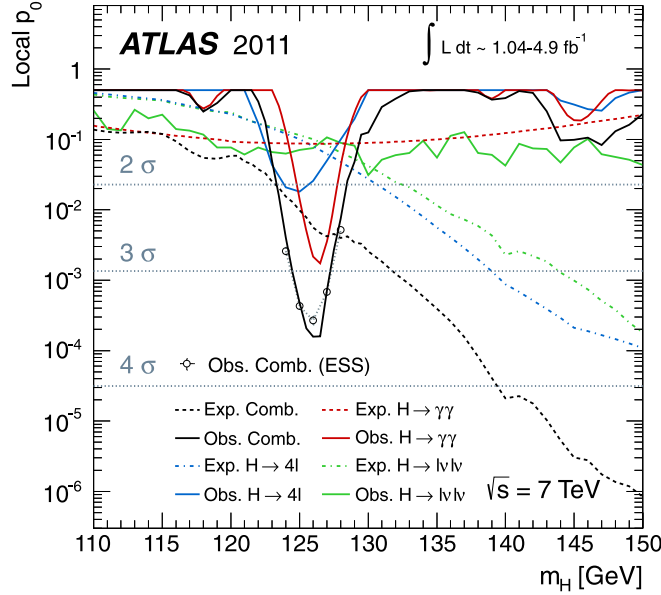


Figure 3.7: Local p_0 values for an earlier combination that shows the explicit tests of the asymptotic equations with pseudo-experiments on a model with uncertainties on energy scale systematics.

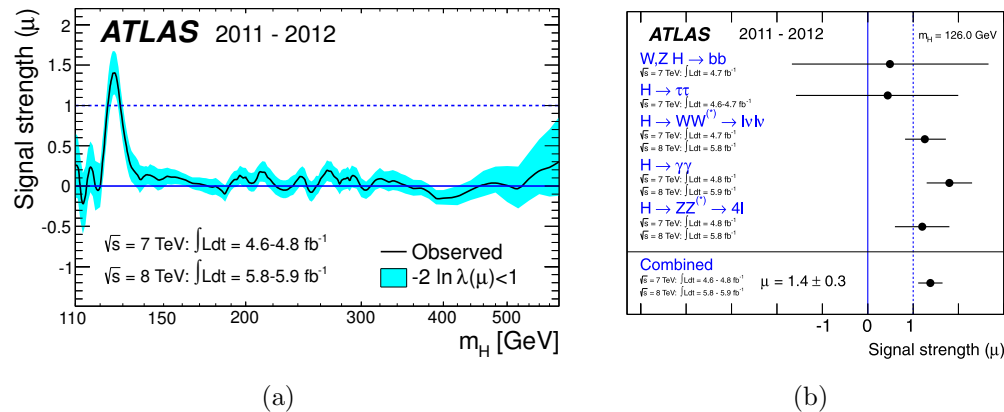


Figure 3.8: Signal strengths measurements in the combination (a) across the full parameter range and (b) broken down by channel.

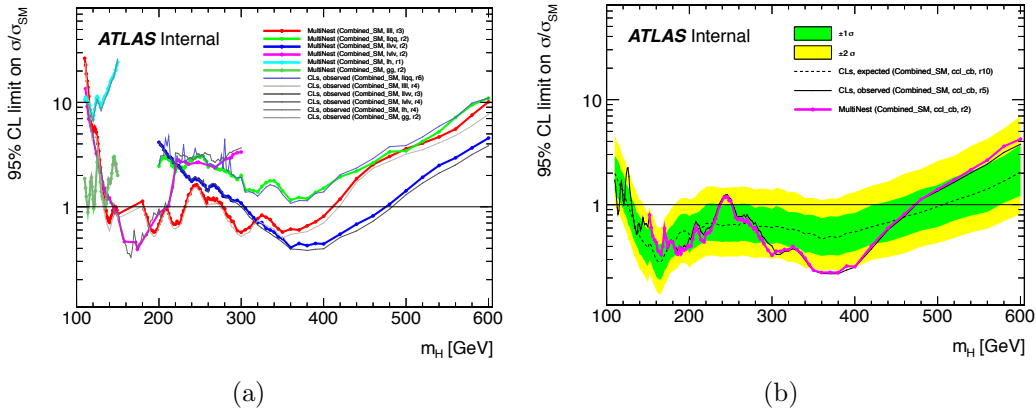


Figure 3.9: MULTINEST checks on upper limits with $1.1 - 4.9 \text{ fb}^{-1}$ of integrated luminosity at $\sqrt{s} = 7 \text{ TeV}$ for (a) individual decay channels and (b) the combination of those channels. The MULTINEST results and the results from asymptotic calculations are shown.

Bayesian credibility intervals with the goal to build confidence in our main results.

MULTINEST [145, 146] is a multimodal nested sampler. To use the ATLAS models, I wrote a generic interface for ROOT to the MULTINEST Fortran library. The results of studies for the individual channels that enter the combination and for the combination itself are shown in figure 3.9.

MULTINEST uses ellipsoidal approximations of iso-likelihood contours. This approximation becomes exponentially worse as the dimensionality of the parameter space is increased. In the low m_H range, the dimensionality of the parameter space is higher for the combined model as more input channels contribute. I used Metropolis-Hastings and Gibbs sampling to construct a credibility interval using Markov-Chain-Monte-Carlo (MCMC). The result of a run on the combined model is compared to asymptotic results in figure 3.10. At each parameter point m_H , five chains are constructed with 100,000 entries. The first 60,000 entries are discarded as burn-in and the most probable signal strength is evaluated for each chain separately. The chains with the lowest and highest most probable signal

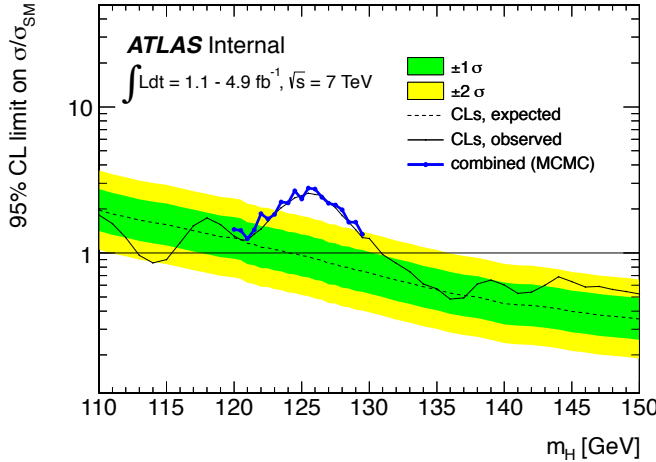


Figure 3.10: Checks using MCMC on the combined upper limit from asymptotic calculations.

strengths are discarded and the remaining three chains are merged; similar to a median filter.

3.6 Latest Results from $H \rightarrow ZZ^* \rightarrow 4\ell$

For this channel alone, the minimum p_0 value of a scan over hypothetical Higgs masses is 2.7×10^{-11} corresponding to a 6.6σ significance at $m_H = 124.3$ GeV. This is shown in figure 3.11(a). The Standard Model Higgs hypothesis is also excluded over a large range of m_H . The upper limit for the low mass range is shown in figure 3.11(b).

After discovering a new particle, its mass and coupling structure has to be determined which is the subject of the following two chapters.

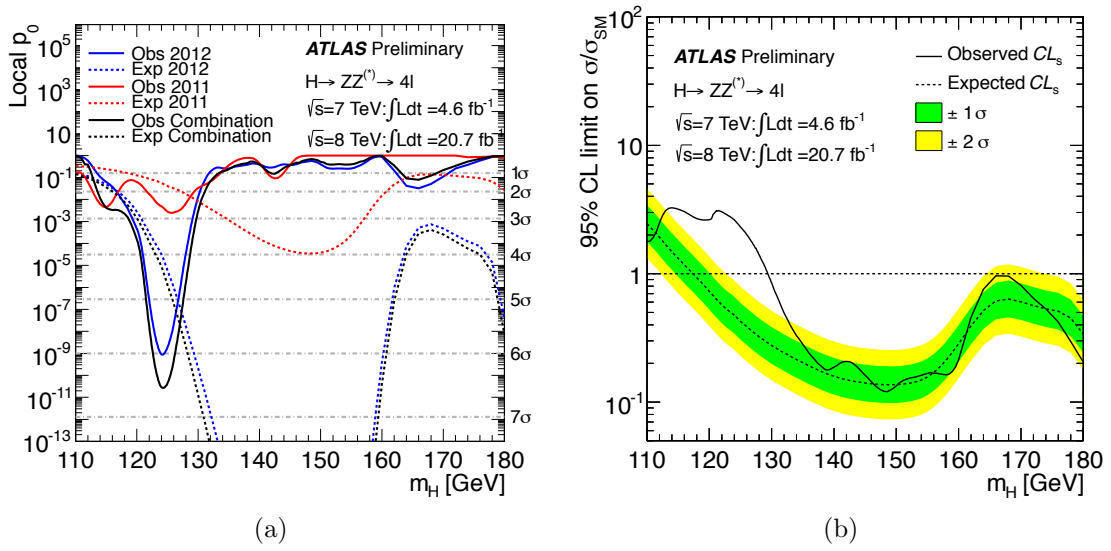


Figure 3.11: Scan of the (a) p_0 values and (b) upper limits across m_H hypotheses.

Chapter 4

Mass Measurement

After discovering a new particle, the first interesting property to measure is its mass. This chapter is based on the ATLAS conference notes [147, 148] and the ATLAS internal notes [11, 149]. Some software tools that I used for these studies are now part of `RooStats` or are available as the Python packages `BatchLikelihoodScan`¹ and `PyROOTUtils`².

Before measuring the Higgs mass itself, a likelihood contour in the plane (μ, m_H) gives insight into the best fit values $\hat{\mu}$ and \hat{m}_H which are two important properties of the newly found particle and provide an overview of the similarity of the observed signal in different decay channels.

To obtain a two-dimensional confidence interval, the likelihood ratio

$$\lambda(\mu, m_H) = \frac{L(\mu, m_H, \hat{\theta}(\mu, m_H))}{L(\hat{\mu}, \hat{m}_H, \hat{\theta})} \quad (4.1)$$

is used, where $\hat{\theta}(\mu, m_H)$ is the conditional maximum likelihood estimate for fixed

¹<https://github.com/svenkreiss/BatchLikelihoodScan>

²<https://github.com/svenkreiss/PyROOTUtils>

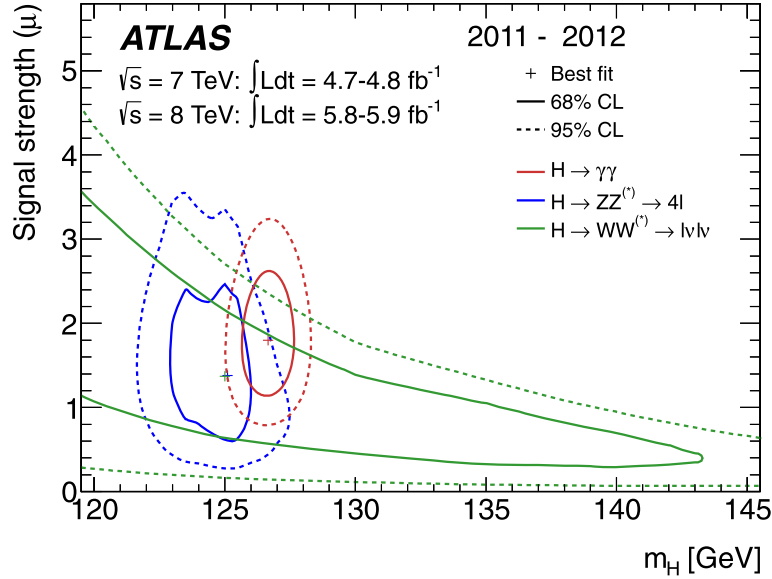


Figure 4.1: Likelihood contours in the (μ, m_H) plane.

μ and m_H . The likelihood contours are closed around $(\hat{\mu}, \hat{m}_H)$ in the presence of strong signal. This likelihood ratio is used to form the test statistic $-2 \ln \lambda(\mu, m_H)$. In the asymptotic limit, it is distributed as a χ^2 distribution with two degrees of freedom, denoted χ_2^2 .

Tests of size α define acceptance and rejection regions in this 2-dimensional parameter space. In the asymptotic regime, the threshold k_α that separates these two regions is defined by

$$P(\chi_2^2 > k_\alpha) = \alpha \quad (4.2)$$

and defines contours with confidence level $100(1 - \alpha)\%$. Therefore, the 68% and 95% CL contours are at $-2 \ln \lambda(\mu, m_H) = 2.3$ and 6.0 . I produced the results shown in figure 4.1 that were published in ATLAS's discovery paper [12] and in Science [121].

The mass measurement is particularly sensitive to energy and momentum scale

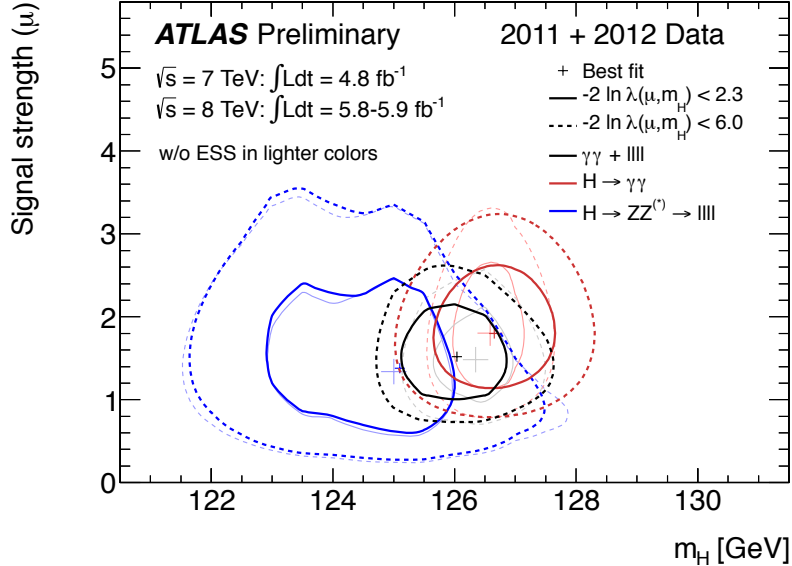


Figure 4.2: Comparison of likelihood contours in the (μ, m_H) plane with and without ESS uncertainties [11].

uncertainties, called ESS. A study is shown in figure 4.2 where “w/o ESS” are contours obtained with fixed nominal values of the ESS nuisance parameters. In figure 4.3 this procedure was modified to fix the ESS nuisance parameters at their best fit value to data instead of nominal values.

The results shown so far in this chapter are based on models at fixed values of m_H .

4.1 Combined Mass

To measure the mass of the newly discovered particle, neither the minimum of a p_0 scan over m_H nor the max of a μ scan can be used to measure the Higgs boson mass. A method had to be found to obtain the maximum likelihood estimate of m_H while only having models available for discrete values of m_H . In principle, the confidence interval of m_H for a single channel is constructed with a one-dimensional

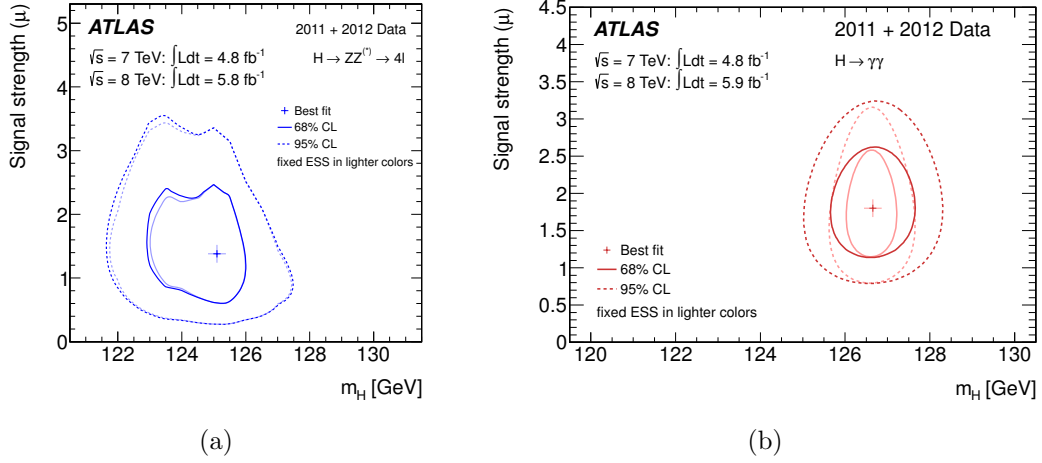


Figure 4.3: Likelihood contours in (μ, m_H) for (a) $H \rightarrow ZZ^* \rightarrow 4\ell$ and (b) $H \rightarrow \gamma\gamma$ with and without ESS uncertainties.

likelihood in m_H . The signal strength μ is treated as a nuisance parameter and profiled to data.

The first likelihood curves for the two channels $H \rightarrow ZZ^* \rightarrow 4\ell$ and $H \rightarrow \gamma\gamma$ are shown in figure 4.4. As expected, the interval obtained from $H \rightarrow \gamma\gamma$ is more sensitive to energy scale uncertainties than the interval for $H \rightarrow ZZ^* \rightarrow 4\ell$.

The combination of the two channels is shown in figure 4.5 . In the combination, there is the subtle difference of whether one wants to enforce that the signal strengths are the same in all channels. Various studies were made and are included in some of the figures here, but the final result for m_H is based on models where the two channels can have a different signal strengths. The profile likelihood ratio³ for this case is

$$\Lambda(m_H) = \frac{L(m_H, \hat{\mu}_{\gamma\gamma}(m_H), \hat{\mu}_{4l}(m_H), \hat{\theta}(m_H))}{L(\hat{m}_H, \hat{\mu}_{\gamma\gamma}, \hat{\mu}_{4l}, \hat{\theta})} . \quad (4.3)$$

³In earlier ATLAS publications, the symbol λ was used for profile likelihood ratios and then later replaced with Λ as λ started to be used to denote ratios of coupling scale factors.

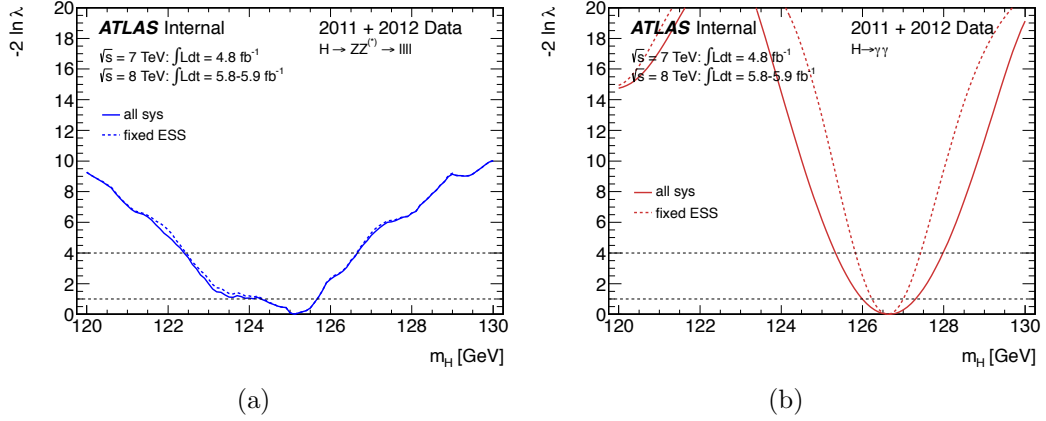


Figure 4.4: Likelihood curves in m_H for (a) $H \rightarrow ZZ^* \rightarrow 4\ell$ and (b) $H \rightarrow \gamma\gamma$.

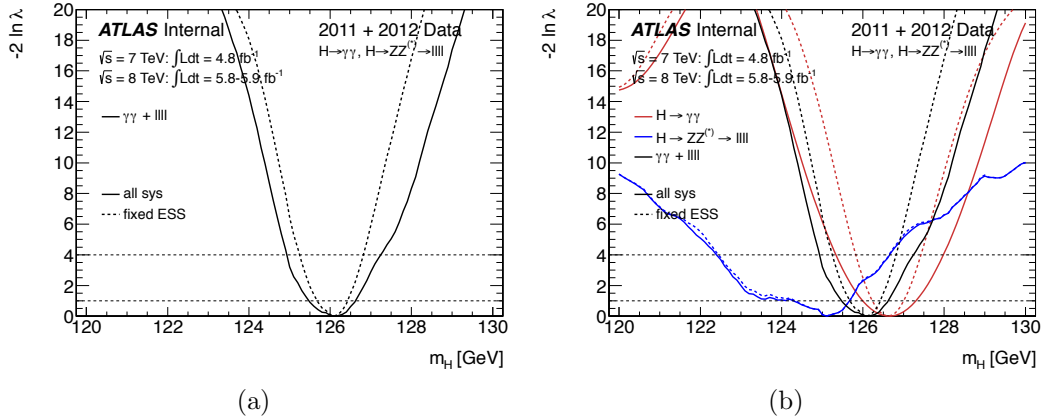


Figure 4.5: First likelihood curves $-2 \ln \lambda(m_H)$ for channels with μ profiled with (solid) and without (dashed) ESS uncertainties [11].

These first measurements were used to obtain a value and confidence interval for the discovery paper. The models were not optimized for mass measurements. The signals and backgrounds were modeled in a binned form with a bin width of 0.5 GeV in m_{4l} . Small numbers of events in the MC simulations that were used to make the binned signal lead to statistical fluctuations from bin to bin in the shape. The shape of the $H \rightarrow ZZ^* \rightarrow 4\ell$ likelihood curve is an artifact of that.

These problems especially in $H \rightarrow ZZ^* \rightarrow 4\ell$ prompted me to work on better

modeling techniques for such a channel. The low count of observed events made the model particularly susceptible to inaccuracies in the modeling of the shape due to a low number of available MC events. The method that I proposed uses an adaptive width kernel density estimate (KEYS [116]) for the signal combined with a piecewise linear interpolation for the existing background histograms. With the improved signal modeling, the observed events were also moved from a binned form to an unbinned form. The interpolation in m_H of the signal shapes was done with the interpolation algorithm described in section 2.5 that is specifically designed for horizontally moving shapes. After these improvements and adding the remaining data collected in 2012, the new result shown in figure 4.6(a) is a vastly improved version compared to the earlier result shown in figure 4.4(a). The additional data also allows a more detailed study of the mass measurement for the separate final states in the $H \rightarrow ZZ^* \rightarrow 4\ell$ channel as shown in figure 4.6(b). It can be seen that the 4μ final state is quite low in m_H and the $4e$ is fairly high and close to the Higgs boson mass measured in the $H \rightarrow \gamma\gamma$ channel.

The latest studies looking at the combined m_H measurement from $H \rightarrow ZZ^* \rightarrow 4\ell$ and $H \rightarrow \gamma\gamma$ give

$$m_H = 125.5 \pm 0.2(\text{stat})^{+0.5}_{-0.6}(\text{sys}) \text{ GeV} \quad (4.4)$$

which is shown in figure 4.7.

4.2 $H \rightarrow ZZ^* \rightarrow 4\ell$ and $H \rightarrow \gamma\gamma$ Mass Compatibility

From the very beginning right after the discovery, the measured values for m_H in the $H \rightarrow ZZ^* \rightarrow 4\ell$ and $H \rightarrow \gamma\gamma$ channels seemed to have some tension. This tension cannot be quantified from graphs like those in figure 4.7. I ran a special

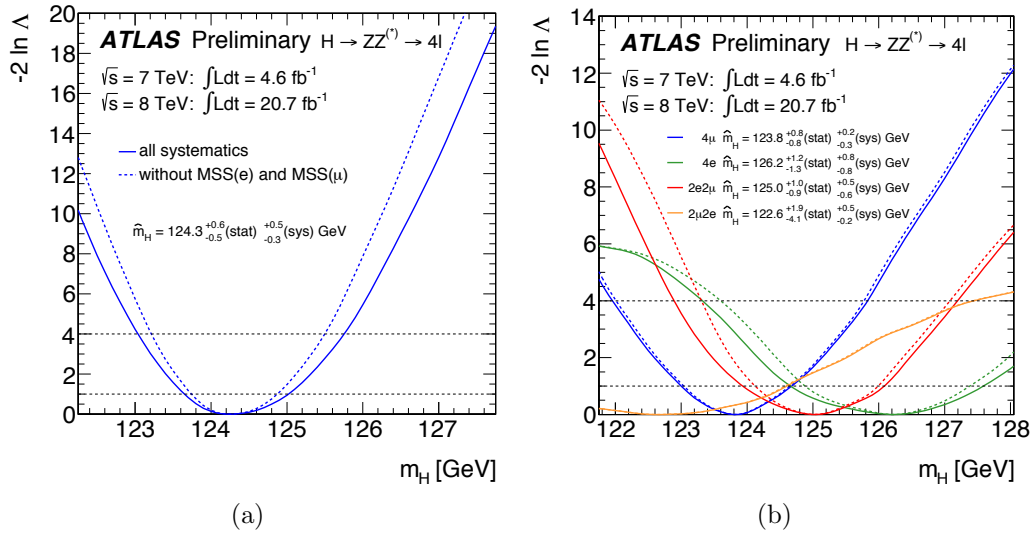


Figure 4.6: $H \rightarrow ZZ^* \rightarrow 4\ell$ mass measurement [10].

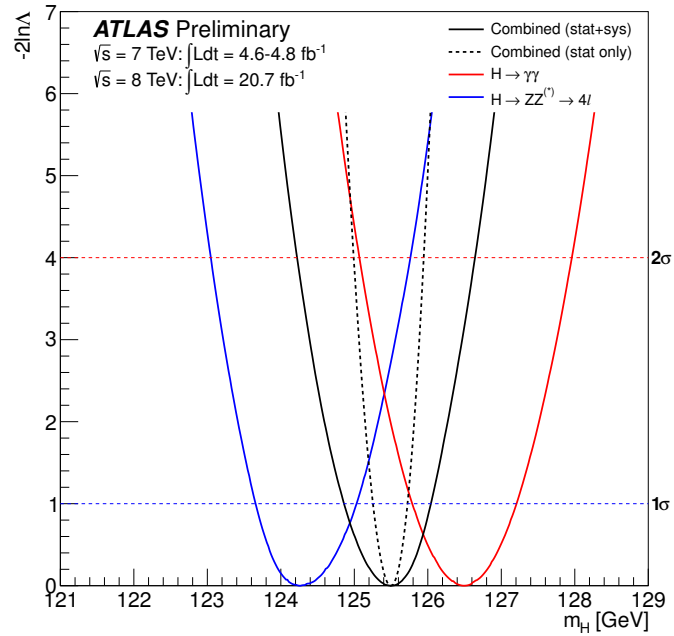


Figure 4.7: Latest combined Higgs boson mass measurement.

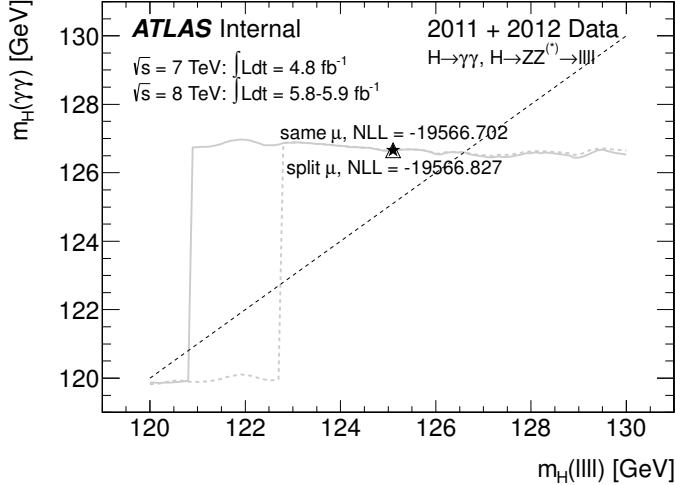


Figure 4.8: Illustrating the model to test the Higgs mass compatibility between the $H \rightarrow \gamma\gamma$ and $H \rightarrow ZZ^* \rightarrow 4\ell$ measurements. The best fit points in $(m_H^{4l}, m_H^{\gamma\gamma})$ are shown for the scenarios with a common signal strength (gray solid, star) and separate signal strengths $\mu^{\gamma\gamma}$ and μ^{4l} (gray dashed, triangle) [11].

study to map likelihood values in the $(m_H^{4l}, m_H^{\gamma\gamma})$ plane. Figure 4.8 shows the setup for the first mass compatibility study. Likelihood values were calculated in discrete steps in m_H^{4l} . The gray lines show the profiled values of $m_H^{\gamma\gamma}$ that contain the estimates for the global minima. The discontinuities are due to local minima. The dashed black line shows the hypotheses of fully compatible masses $m_H^{4l} = m_H^{\gamma\gamma}$.

Various scenarios to investigate the compatibility between the two measured Higgs masses in the $H \rightarrow \gamma\gamma$ and $H \rightarrow ZZ^* \rightarrow 4\ell$ channel are shown in figure 4.9. Shown are the profile likelihood ratio values along the diagonal of figure 4.8 which is $m_H^{4l} = m_H^{\gamma\gamma}$ with respect to the best fit point that is not on the diagonal and marked by a star and triangle. To quantize the compatibility at the “best” point at the bottom of the graph, it is important to note that this point is distributed like a χ^2 with one degree less than the one shown as “picking the best point” is equivalent to profiling one of the degrees of freedom.

The profile likelihood ratio that was used for all final results to study the mass

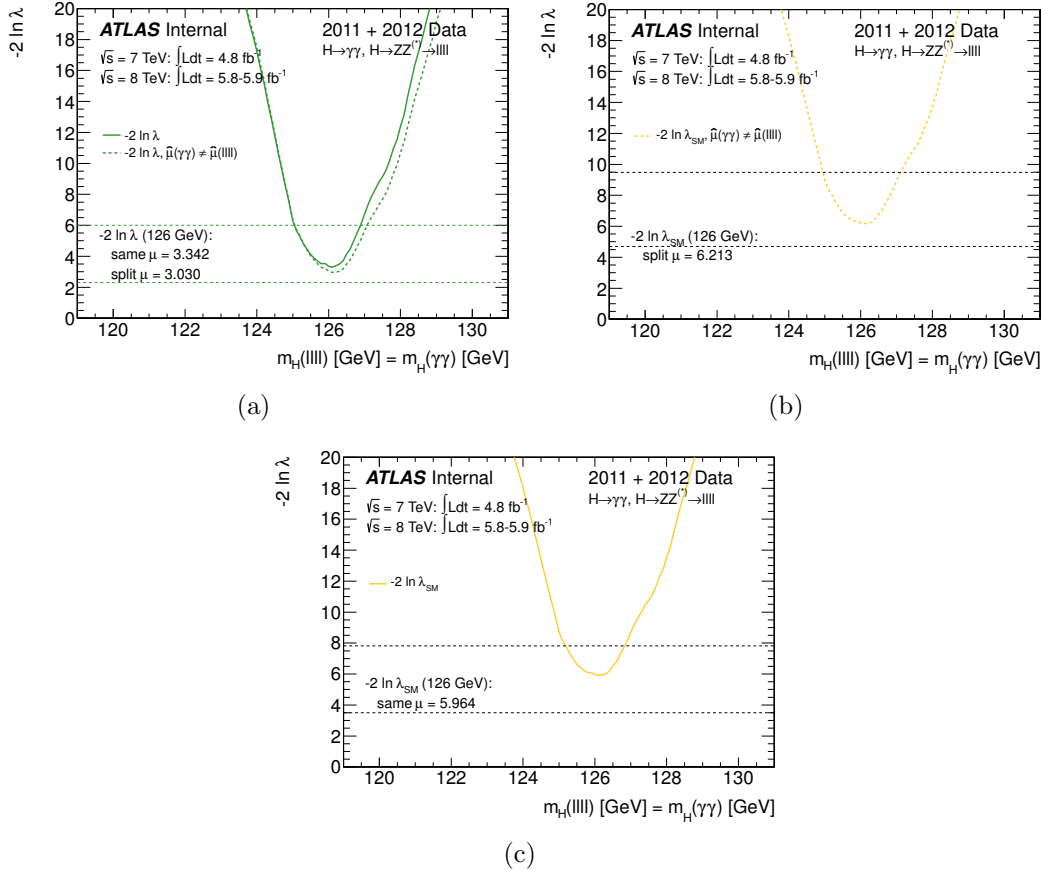


Figure 4.9: Scans of likelihoods along the dashed diagonal in figure 4.8. (a) The likelihood curve $-2 \ln \lambda(m_H)$ along $m_H^{\gamma\gamma} = m_H^{4l}$ with a single signal strength μ (solid) or independent signal strengths $\mu^{\gamma\gamma}$ and μ^{4l} profiled (both following a χ^2 distribution). (b) The likelihood curve $-2 \ln \lambda(m_H)$ along $m_H^{\gamma\gamma} = m_H^{4l}$ with independent signal strengths $\mu^{\gamma\gamma}$ and μ^{4l} free in the fit but evaluated at the SM values $\mu^{\gamma\gamma} = \mu^{4l} = 1$ (corresponding to a χ_4^2 distribution). (c) The likelihood curve $-2 \ln \lambda(m_H)$ along $m_H^{\gamma\gamma} = m_H^{4l}$ with a single signal strength μ free in the fit but evaluated at the SM values $\mu = 1$ (corresponding to a χ_3^2 distribution) [11].

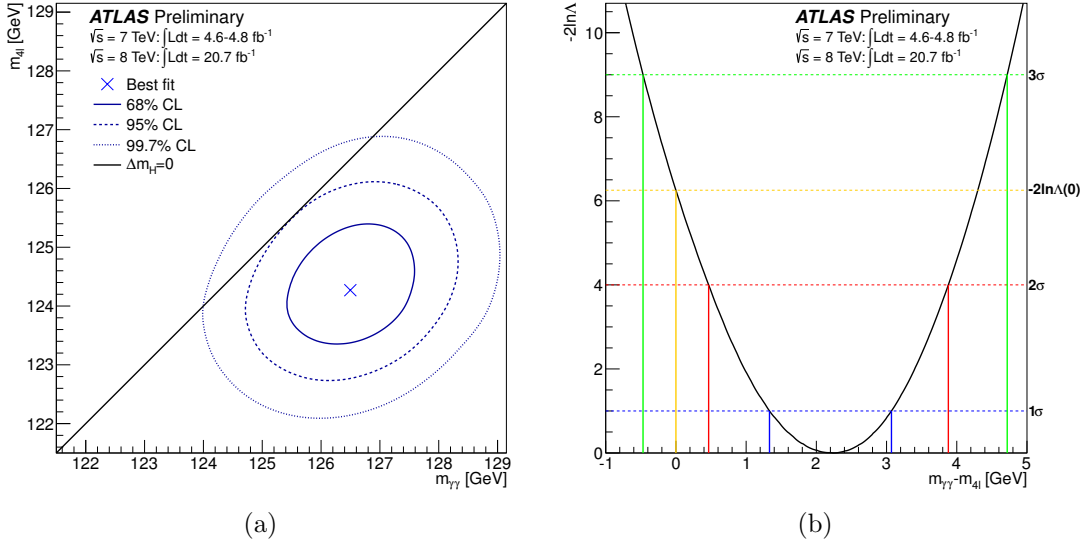


Figure 4.10: Latest results of the mass compatibility between the $H \rightarrow ZZ^* \rightarrow 4\ell$ channel and the $H \rightarrow \gamma\gamma$ channel.

compatibility of these two channels is

$$\Lambda(\Delta m_H) = \frac{L(\Delta m_H, \hat{m}_H(\Delta m_H), \hat{\mu}_{\gamma\gamma}(\Delta m_H), \hat{\mu}_{4l}(\Delta m_H), \hat{\theta}(\Delta m_H))}{L(\Delta \hat{m}_H, \hat{m}_H, \hat{\mu}_{\gamma\gamma}, \hat{\mu}_{4l}, \hat{\theta})} \quad (4.5)$$

Using the full 2011 and 2012 data sets, the latest results are shown in figure 4.10.

The measured mass difference $\Delta m_H = m_{\gamma\gamma} - m_{4l}$ is

$$\Delta \hat{m}_H = 2.3^{+0.6}_{-0.7}(\text{stat}) \pm 0.6(\text{sys}) \text{ GeV} \quad . \quad (4.6)$$

The probability that a single Higgs boson disfavors the $\Delta m_H = 0$ hypothesis by more than what is observed in data is 1.2% which corresponds to about 2.5σ . This result using the asymptotic approximation is checked with pseudo-experiments which gives a slightly higher probability of 1.5% and 2.4σ . This is a two-sided test where both the $m_H^{\gamma\gamma} > m_H^{4l}$ and $m_H^{\gamma\gamma} < m_H^{4l}$ cases are considered.

Chapter 5

Coupling Measurements

Coupling measurements investigate the interaction strengths of the Higgs boson with other particles. They are based on effective Lagrangians with the Standard Model gauge structure. Deviations from coupling strengths predicted by the Standard Model would provide the first hint for new physics beyond the Standard Model.

ATLAS has just made a new combination public [150]. My contribution to this conference note as one of the six authors inside of ATLAS is significant. In the past two years, I have been heavily involved in the ATLAS Higgs combination group [151, 152, 153, 154, 155, 156, 157, 158, 159], including as a co-author for the last publication [160].

As a more convenient interface to the numbers published by the LHC Higgs Cross Section Working Group, I published the Python package `LHCHiggsCouplings`¹ that I used for the studies in this chapter.

This chapter reviews the latest results and shows novel techniques to cross check

¹<https://github.com/svenkreiss/LHCHiggsCouplings>

Higgs boson Decay	Subsequent Decay	Sub-Channels	$\int L dt$ [fb $^{-1}$]	Ref.
2011 $\sqrt{s}=7$ TeV				
$H \rightarrow \gamma\gamma$	—	10 categories $\{p_{\text{Tr}} \otimes \eta_\gamma \otimes \text{conversion}\} \oplus \{2\text{-jet VBF}\}$ $\{4e, 2e2\mu, 2\mu2e, 4\mu, 2\text{-jet VBF}, \ell\text{-tag}\}$	4.8	[160]
$H \rightarrow ZZ^*$	4ℓ	$\{4e, e\mu, \mu e, \mu\mu\} \otimes \{0\text{-jet, 1-jet, 2-jet VBF}\}$	4.6	[160]
$H \rightarrow WW^*$	$\ell\nu\ell\nu$	$\{ee, e\mu, \mu e, \mu\mu\} \otimes \{0\text{-jet, 1-jet, 2-jet VBF}\}$	4.6	[160]
$VH \rightarrow Vbb$	$Z \rightarrow \nu\nu$	$E_{\text{T}}^{\text{miss}} \in \{120 - 160, 160 - 200, \geq 200 \text{ GeV}\} \otimes \{2\text{-jet, 3-jet}\}$ $p_{\text{T}}^W \in \{< 50, 50 - 100, 100 - 150, 150 - 200, \geq 200 \text{ GeV}\}$ $p_{\text{T}}^Z \in \{< 50, 50 - 100, 100 - 150, 150 - 200, \geq 200 \text{ GeV}\}$	4.6	[161]
2012 $\sqrt{s}=8$ TeV				
$H \rightarrow \gamma\gamma$	—	14 categories: $\{p_{\text{Tr}} \otimes \eta_\gamma \otimes \text{conversion}\} \oplus \{\text{loose, tight 2-jet VBF}\} \oplus \{\ell\text{-tag}, E_{\text{T}}^{\text{miss-tag}}, 2\text{-jet VH}\}$	20.3	[160]
$H \rightarrow ZZ^*$	4ℓ	$\{4e, 2e2\mu, 2\mu2e, 4\mu, 2\text{-jet VBF}, \ell\text{-tag}\}$	20.3	[160]
$H \rightarrow WW^*$	$\ell\nu\ell\nu$	$\{ee, e\mu, \mu e, \mu\mu\} \otimes \{0\text{-jet, 1-jet, 2-jet VBF}\}$	20.3	[160]
$VH \rightarrow Vbb$	$Z \rightarrow \nu\nu$	$E_{\text{T}}^{\text{miss}} \in \{120 - 160, 160 - 200, \geq 200 \text{ GeV}\} \otimes \{2\text{-jet, 3-jet}\}$ $p_{\text{T}}^W \in \{< 90, 90 - 120, 120 - 160, 160 - 200, \geq 200 \text{ GeV}\} \otimes \{2\text{-jet, 3-jet}\}$ $p_{\text{T}}^Z \in \{< 90, 90 - 120, 120 - 160, 160 - 200, \geq 200 \text{ GeV}\} \otimes \{2\text{-jet, 3-jet}\}$	20.3	[161]
$H \rightarrow \tau\tau$	$\tau_1\tau_2\tau_3\tau_4$	$\{ee, e\mu, \mu e, \mu\mu\} \otimes \{\text{boosted, 2-jet VBF}\}$ $\{e, \mu\} \otimes \{\text{boosted, 2-jet VBF}\}$ $\{\text{boosted, 2-jet VBF}\}$	20.3	[162]
$H \rightarrow \tau\tau$	$\tau_1\tau_2\tau_3\tau_4$	$\{\text{boosted, 2-jet VBF}\}$	20.3	

Table 5.1: Overview of channels entering the latest ATLAS combination. All analyses are updated to the full 2011 and 2012 data set. Analysis strategies were also updated to increase sensitivity to individual production modes.

current results and improve future analyses. The updated list of inputs used for these studies is shown in table 5.1. Here, the strategies of the individual analyses are updated from a pure search to also increase sensitivity to different production modes of the Higgs boson as shown for example by the extra categories in $H \rightarrow \gamma\gamma$ and $H \rightarrow ZZ^* \rightarrow 4\ell$ that are optimized for VBF and VH.

5.1 Cross Sections and Branching Ratios

The statistical procedures used here is not different from the methods shown so far. Hypothesis tests and confidence intervals for the parameters of interest $\boldsymbol{\alpha}$ are based on the profile likelihood ratio

$$\Lambda(\boldsymbol{\alpha}) = \frac{L(\boldsymbol{\alpha}, \hat{\boldsymbol{\theta}}(\boldsymbol{\alpha}))}{L(\hat{\boldsymbol{\alpha}}, \hat{\boldsymbol{\theta}})} \quad (5.1)$$

where $\boldsymbol{\theta}$ are the nuisance parameters. The test statistic $-2 \ln \Lambda(\boldsymbol{\alpha})$ is asymptotically distributed as a χ_n^2 distribution where n is the number of parameters of interest. For two degrees of freedom, approximate likelihood contours for 68% and 95% CL intervals are drawn at $-2 \ln \Lambda(\boldsymbol{\alpha}) = 2.3$ and 6.0 according to the asymptotic approximation with a χ_2^2 . The studies in this chapter are all done for a fixed Higgs boson mass hypothesis of $m_H = 125.5$ GeV.

Coupling measurements in ATLAS and CMS are done using the effective model framework provided by the LHC Higgs Cross Section Working Group which probes small deviations from the Standard Model without changing the tensor structure of the couplings. In this framework, the common interface to coupling measurements are the signal strength measurements for all decay channels broken down by production mode. All coupling measurements are special combinations of signal

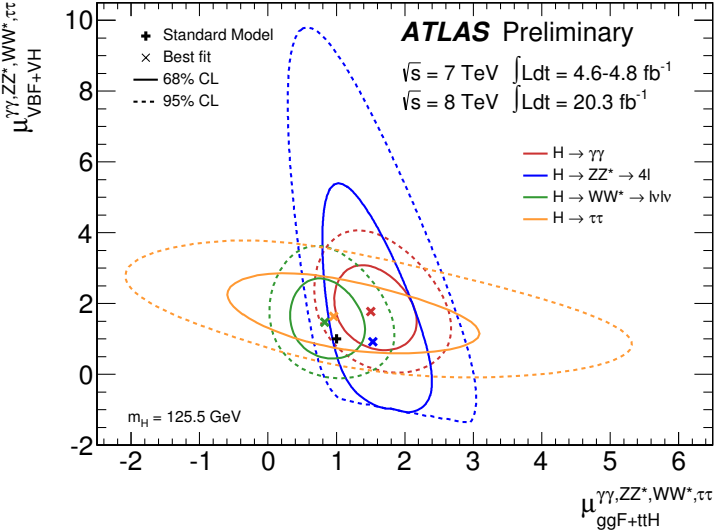


Figure 5.1: Likelihood contours for $H \rightarrow \gamma\gamma$, $H \rightarrow ZZ^* \rightarrow 4\ell$, $H \rightarrow WW^* \rightarrow \ell\nu\ell\nu$ and $H \rightarrow \tau\tau$ in the production times branching ratio planes ($\mu_{ggF+ttH} \times B/B_{SM}$, $\mu_{VBF+VH} \times B/B_{SM}$).

strength measurements. Likelihood contours for the four decay channels $H \rightarrow \gamma\gamma$, $H \rightarrow ZZ^* \rightarrow 4\ell$, $H \rightarrow WW^* \rightarrow \ell\nu\ell\nu$ and $H \rightarrow \tau\tau$ are shown in figure 5.1.

The detector can only measure event counts which are a product of production cross section and decay branching ratio. Therefore, the cross section and branching ratio are completely degenerate. Although the four channels are shown on the same plot, the axes are different for every channel as B/B_{SM} is specific to every decay channel. One way to break the degeneracy of production and decay rates is to form ratios. One possibility is to look at ratios of the two axes in figure 5.1 for each channel. Figure 5.2 shows measurements of the ratio of $\mu_{VBF+VH}/\mu_{ggF+ttH}$ where μ_{VBF+VH} is a signal strength common to VBF and VH and $\mu_{ggF+ttH}$ is a signal strength common to ggF and $t\bar{t}H$.

Another advantage is that the axis $\mu_{VBF+VH}/\mu_{ggF+ttH}$ is now independent of the decay channel under consideration and a combined value is meaningful. The

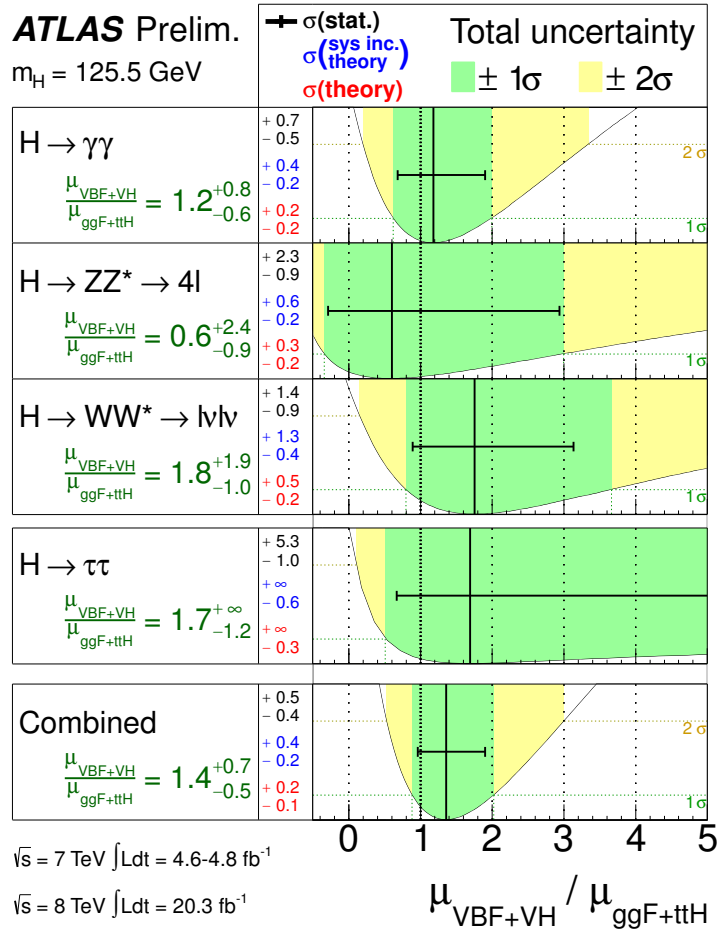


Figure 5.2: The ratio of the signal strength for processes dominated by gauge boson couplings, VBF and VH, over the signal strength for processes dominated by the top coupling, ggF and $t\bar{t}H$.

observed combined value of

$$\mu_{VBF+VH}/\mu_{ggF+ttH} = 1.4^{+0.5}_{-0.4}(\text{stat})^{+0.4}_{-0.2}(\text{sys}) \quad (5.2)$$

is compatible with the SM expectation.

The VBF process is particularly interesting by itself and so the assumption of equal signal strengths between the VBF and VH processes was relaxed. The combined measured ratio of $\mu_{VBF}/\mu_{ggF+ttH}$ without VH but with $\mu_{VH}/\mu_{ggF+ttH}$ being treated as a nuisance parameter is

$$\mu_{VBF}/\mu_{ggF+ttH} = 1.4^{+0.5}_{-0.4}(\text{stat})^{+0.4}_{-0.3}(\text{sys}) \quad (5.3)$$

and I produced the study shown in figure 5.3. It also shows that the hypothesis of $\mu_{VBF}/\mu_{ggF+ttH} = 0$ is unlikely. The evidence for VBF production is at the 4.1σ level. An earlier version of my study was published in the summary on the Higgs boson in the Particle Data Group's Review of Particle Physics [32].

Another way to break the degeneracy of cross section and branching ratio in the event count is to take ratios of decay channels which results in the ratio of branching ratios. We defined a normalized ratio ρ with respect to the theoretical values of the branching ratios in the Standard Model. For example, for the two channels $H \rightarrow \gamma\gamma$ and $H \rightarrow ZZ^* \rightarrow 4\ell$, ρ is defined as

$$\rho_{\gamma\gamma/ZZ} = \frac{BR(H \rightarrow \gamma\gamma)}{BR(H \rightarrow ZZ^*)} \cdot \frac{BR_{\text{SM}}(H \rightarrow ZZ^*)}{BR_{\text{SM}}(H \rightarrow \gamma\gamma)} \quad . \quad (5.4)$$

The observed likelihood curves are shown in figure 5.4 with the expected SM curves.

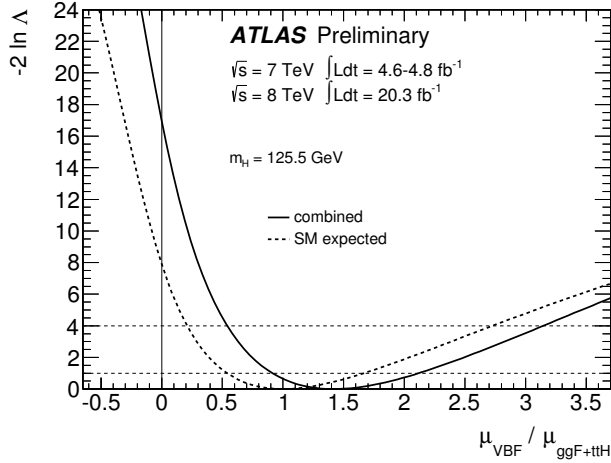


Figure 5.3: The ratio of the signal strength for the VBF process over the signal strength for ggF and $t\bar{t}H$ while profiling the signal strength for VH. It shows evidence for VBF production.

The measured values are

$$\rho_{\gamma\gamma/ZZ} = 1.1^{+0.4}_{-0.3}, \quad \rho_{\gamma\gamma/WW} = 1.7^{+0.7}_{-0.5}, \quad \rho_{ZZ/WW} = 1.6^{+0.8}_{-0.5} \quad (5.5)$$

which are all in agreement with the Standard Model expectation of one. The ratio $\rho_{ZZ/WW}$ was used as one of the first custodial symmetry measurements in the Higgs sector as it is a clean model independent ratio. The ρ -values are also interesting experimentally as the theoretical uncertainty in the production mode cross section cancels in the ratio.

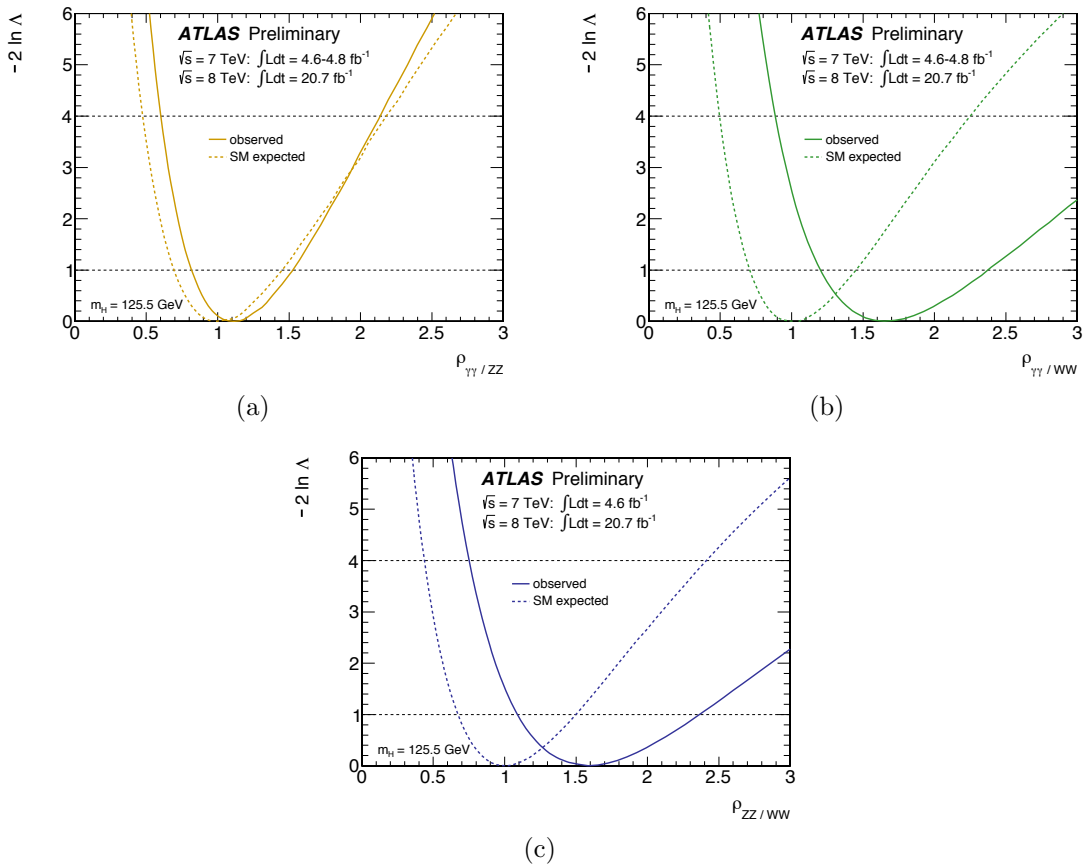


Figure 5.4: Measurements of the ratios of branching ratios ρ .

5.2 Testing the Standard Model Hypothesis: Benchmark Models

The LHC Higgs Cross Section Working Group proposed a set up leading order tree level motivated benchmark models in [163]. It is a framework to test for deviations from the Standard Model predictions of event rates. It is based on a few assumptions. The signal that the individual search channels observe all originate from one narrow resonance with a mass of 125.5 GeV. The width of the Higgs boson is neglected and the zero-width approximation is used, which implies that the production cross section and decay rates factorize without interference:

$$(\sigma \cdot BR)(i \rightarrow H \rightarrow f) = \frac{\sigma_i \cdot \Gamma_f}{\Gamma_H} \quad (5.6)$$

where σ_i is the Higgs production cross section from the initial state i , Γ_f is the partial width of the Higgs boson decaying to the final state f and Γ_H is the total width of the Higgs boson. The last assumption is that the tensor structure of the Higgs couplings is assumed to be the same as in the SM; i.e. the discovered Higgs boson is a CP-even scalar.

In this framework, coupling scale factors κ are introduced that are normalized to the SM coupling strengths and modify it in a way that is inspired by the leading order processes; see [163]. The effective coupling scale factors κ_γ , κ_g and κ_{VBF} as well as the total width scale factor κ_H^2 are expressed in terms of the more

fundamental coupling scale factors

$$\kappa_\gamma^s \sim 1.59\kappa_W^2 - 0.66\kappa_W\kappa_t + 0.07\kappa_t^2 \quad (5.7)$$

$$\kappa_g^2 \sim 1.06\kappa_t^2 - 0.07\kappa_t\kappa_b + 0.01\kappa_b^2 \quad (5.8)$$

$$\kappa_{VBF}^2 \sim 0.74\kappa_W^2 + 0.26\kappa_Z^2 \quad (5.9)$$

$$\kappa_H^2 \sim 0.57\kappa_b^2 + 0.22\kappa_W^2 + 0.09\kappa_g^2 + 0.06\kappa_\tau^2 + 0.03\kappa_Z^2 + 0.03\kappa_c^2 \quad (5.10)$$

for a Higgs boson mass of 125 GeV.

One of the simplest but also most interesting models is the model that investigates fermion and gauge couplings, called (κ_V, κ_F) . Here, the fundamental coupling scale factors are constrained with

$$\kappa_V = \kappa_W = \kappa_Z \quad (5.11)$$

$$\kappa_F = \kappa_t = \kappa_b = \kappa_\tau = \kappa_g . \quad (5.12)$$

One feature or caveat of this model is the assumption that only SM particles contribute to $gg \rightarrow H$ which ties κ_g directly to κ_F which is an invalid assumption for many models beyond the Standard Model. The latest results for this model when combining all channels as well as an overview for the individual channels is shown in figure 5.5. The combination shows that the data collected with ATLAS has excellent agreement with the predicted SM coupling strength to fermions and is slightly high in the coupling strength to gauge bosons. However, the SM point is well inside the 95% confidence interval. The current measured values of these

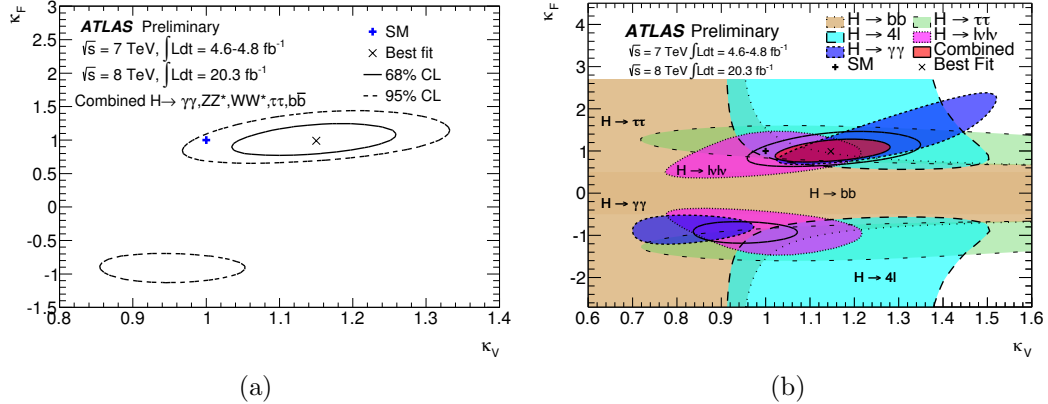


Figure 5.5: The (κ_V, κ_F) benchmark model. (a) shows likelihood contours for the combination of all channels and (b) shows contours for the individual decay channels.

two coupling parameters are

$$\kappa_V = 1.15 \pm 0.08 \quad (5.13)$$

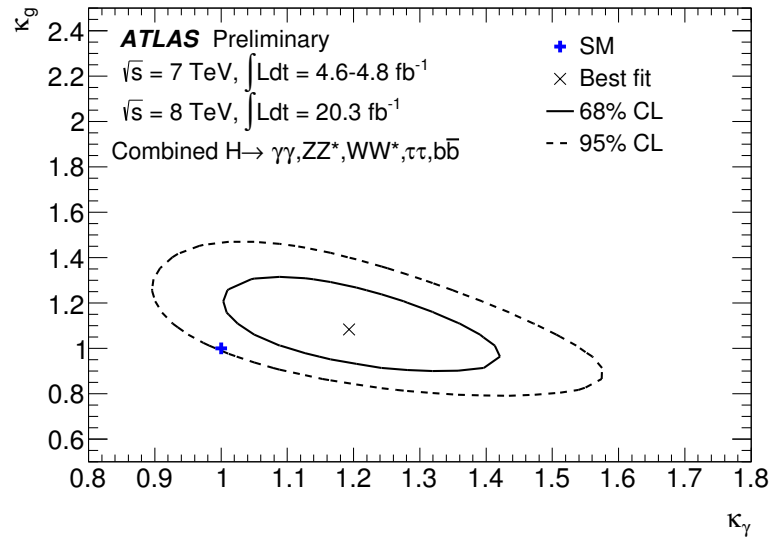
$$\kappa_F = 0.99^{+0.17}_{-0.15} . \quad (5.14)$$

Another benchmark model focuses on the two loops in the $gg \rightarrow H \rightarrow \gamma\gamma$ process for which a slightly high event rate was observed. This model tests possible non-Standard Model contributions to the process. Therefore, the parametrization of this model keeps the effective coupling scale factors $(\kappa_g, \kappa_\gamma)$. The likelihood contours and graphs are shown in figure 5.6. The measured values are

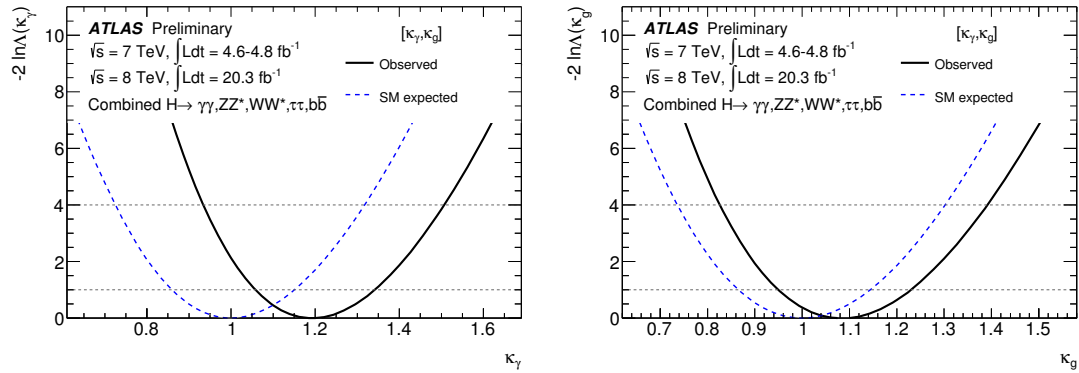
$$\kappa_g = 1.08^{+0.15}_{-0.13} \quad (5.15)$$

$$\kappa_\gamma = 1.19^{+0.15}_{-0.12} \quad (5.16)$$

which shows decent agreement when looking at the two parameters individually, but taken together, the compatibility with the SM decreases to 9%.



(a)



(b)

(c)

Figure 5.6: The $(\kappa_\gamma, \kappa_g)$ benchmark model.

The two models shown here rely on the assumption that only SM particles contribute to the total width of the Higgs boson. This assumption can be relaxed for the (κ_V, κ_F) model by forming ratios and investigating $(\kappa_F/\kappa_V, \kappa_V^2/\kappa_H)$ instead which allows to make similar physics statements. For the $(\kappa_g, \kappa_\gamma)$ model, the assumption can be relaxed by adding a term that captures possible invisible and undetectable decays to the total width, called $BR_{\text{inv,undet}}$ in which case the model becomes a three-parameter model with $(\kappa_g, \kappa_\gamma, BR_{\text{inv,undet}})$.

5.3 Studies using Bayesian Techniques

The coupling models are not necessarily unimodal and, as for example shown in figure 5.5, they are in fact multimodal. Also, the likelihood contours are not necessarily Gaussian and can have elongated, “banana”-shaped features. The validation of the approximate methods that are used to derive intervals from likelihoods are verified in the frequentist framework by generating pseudo-experiments from the full model. This has been done for the most important numbers that were published by ATLAS.

Another avenue to build confidence in the results is a cross check using Bayesian techniques. The result will be a credibility interval instead of a confidence interval, but in the case of a Gaussian likelihood and flat priors, we expect the two intervals to agree numerically although they have different meanings. It also addresses an always recurring concern that confidence intervals obtained from likelihood methods when profiling nuisance parameters result in overly aggressive results compared to marginalizing nuisance parameters as is done in the Bayesian context. For all studies, flat priors with a reasonable range were used for all parameters.

Given that this was just a qualitative check on the official result, the sensitivity of this choice was not studied.

The model that seemed most interesting to investigate is a modification of the (κ_V, κ_F) model where κ_V is broken down into the W and Z contributions which are parametrized with κ_Z and $\lambda_{WZ} = \kappa_W/\kappa_Z$ resulting in the $(\kappa_F, \kappa_Z, \lambda_{WZ})$ model. Samples drawn from the posterior and highest probability density (HPD) intervals² are shown in figure 5.7. It shows the multimodal nature of the model along κ_F and the elongated non-Gaussian shape in the (λ_{WZ}, κ_Z) plane. The non-Gaussian shape lends itself to study so called “volume effects” when comparing profiling versus marginalization of parameters.

Simple checks of convergence of the Markov chain to the stationary phase were done by investigating the time evolution of the likelihood value and of the parameters of interest, as shown in figure 5.8. This can be improved using other methods like autocorrelation.

The result of this study is shown in figure 5.9 which directly compares confidence and credibility intervals. The maximum of the profile likelihood is shifted to one and the $-\ln(L) = 0.5$ values are marked with $\Delta NLL = 0.5$ which is the approximate threshold for a likelihood-based 68% confidence interval. The distributions of the posterior are shown in blue and the 68% and 95% HPD intervals are marked in green and red. Figure 5.9(d) shows that the small discrepancy is due to the marginalization over both minima whereas the profile likelihood only picks the deeper minimum. It also shows – ignoring multiple modes – that the 68% confidence interval is numerically very close to the 68% Bayesian credibility interval.

²The ability to construct HPD intervals in one or more dimensions with **ROOT** and **RooStats** was implemented by me for this study.

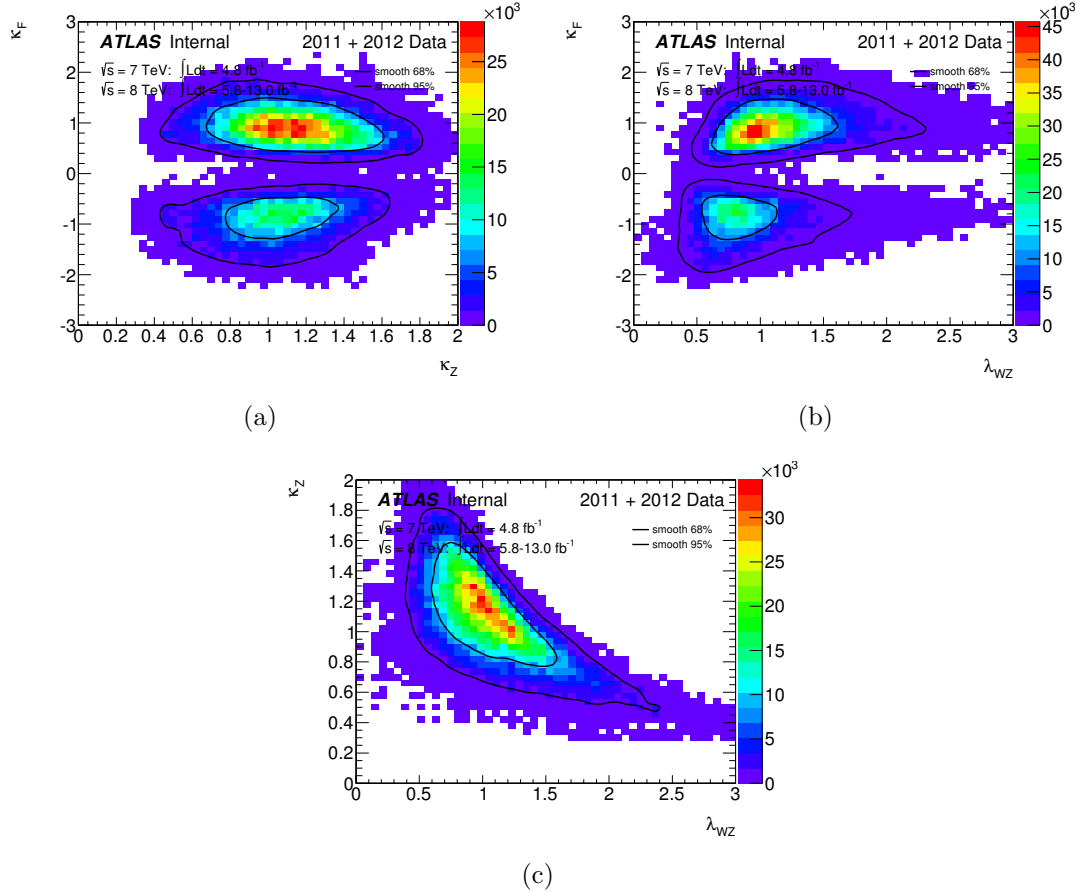


Figure 5.7: The histograms show the density of samples drawn from the posterior. Contours of the highest probability density intervals with 68% and 95% of posterior probability are also shown in solid black.

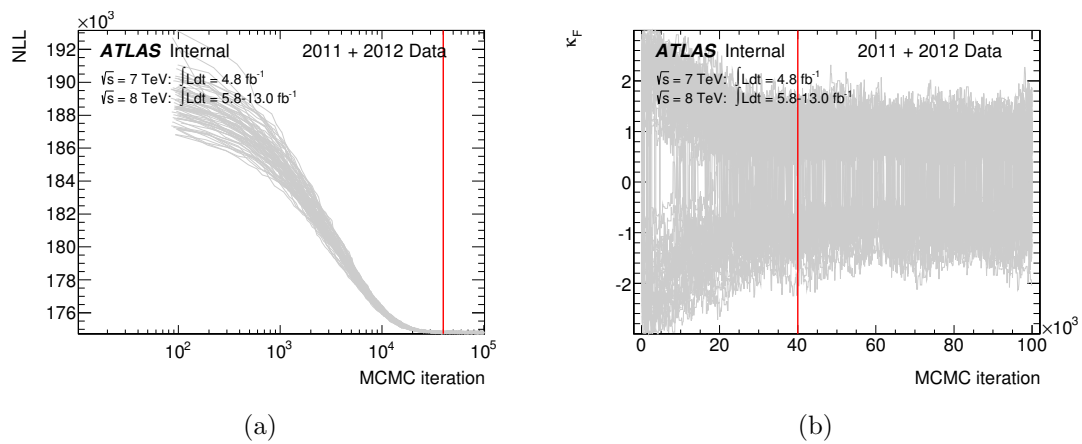


Figure 5.8: Convergence checks.

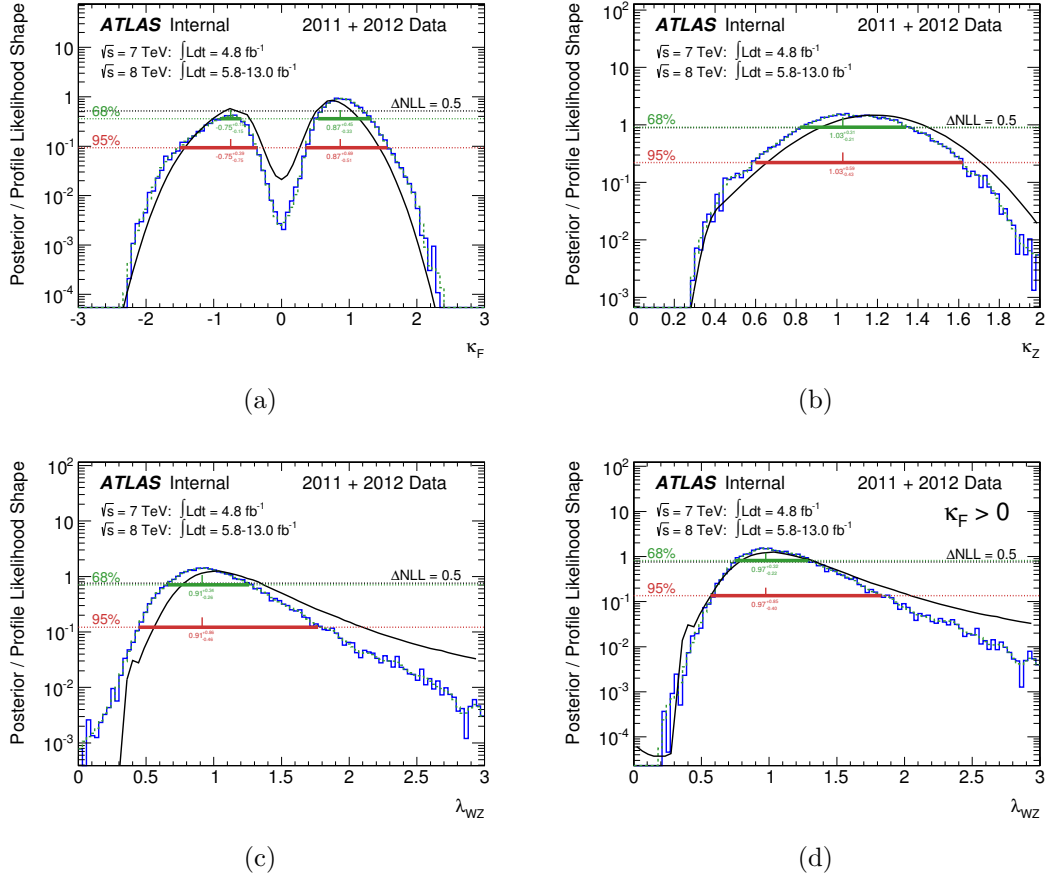


Figure 5.9: Direct comparison of confidence and credibility intervals. The distributions obtained by sampling from the posterior are shown in blue and the profile likelihoods are shown in black.

Overall, this Bayesian study showed good numerical agreement between the confidence and credibility intervals even for non-Gaussian and multimodal likelihood shapes.

5.4 Factorizing Theory Uncertainties

The ATLAS experiment has recently published the first profile likelihood scans of Higgs models shown in figure 5.10. Every scan uses the information from the full likelihood in each channel. Experimental nuisance parameters and nuisance parameters associated with theory uncertainties are profiled separately in each channel. Theory uncertainties use the standard prescription from the LHC Higgs Cross Section Working Group. That prescription is likely to change in the future as progress is being made on the theoretical side.

For a combination, it is necessary to profile common experimental and theoretical nuisance parameters to the same value. Therefore, they need to be *decoupled* from the likelihood scan for a single channel and a tool needs to be available to *recouple* the result. This is the subject of the paper “A Novel Approach to Higgs Coupling Measurements” [164] and the `decouple`³ software package that is summarized here.

To develop and study the method, we used simplified models shown in figure 5.13 that resemble the ATLAS results. The information from the full likelihood is still contained in the effective likelihood and no Gaussian approximation had to be made. Theory uncertainties that scale the signal cross sections move the contours in this plane. The responses to variations in luminosity and two QCD

³<https://github.com/svenkreiss/decouple>

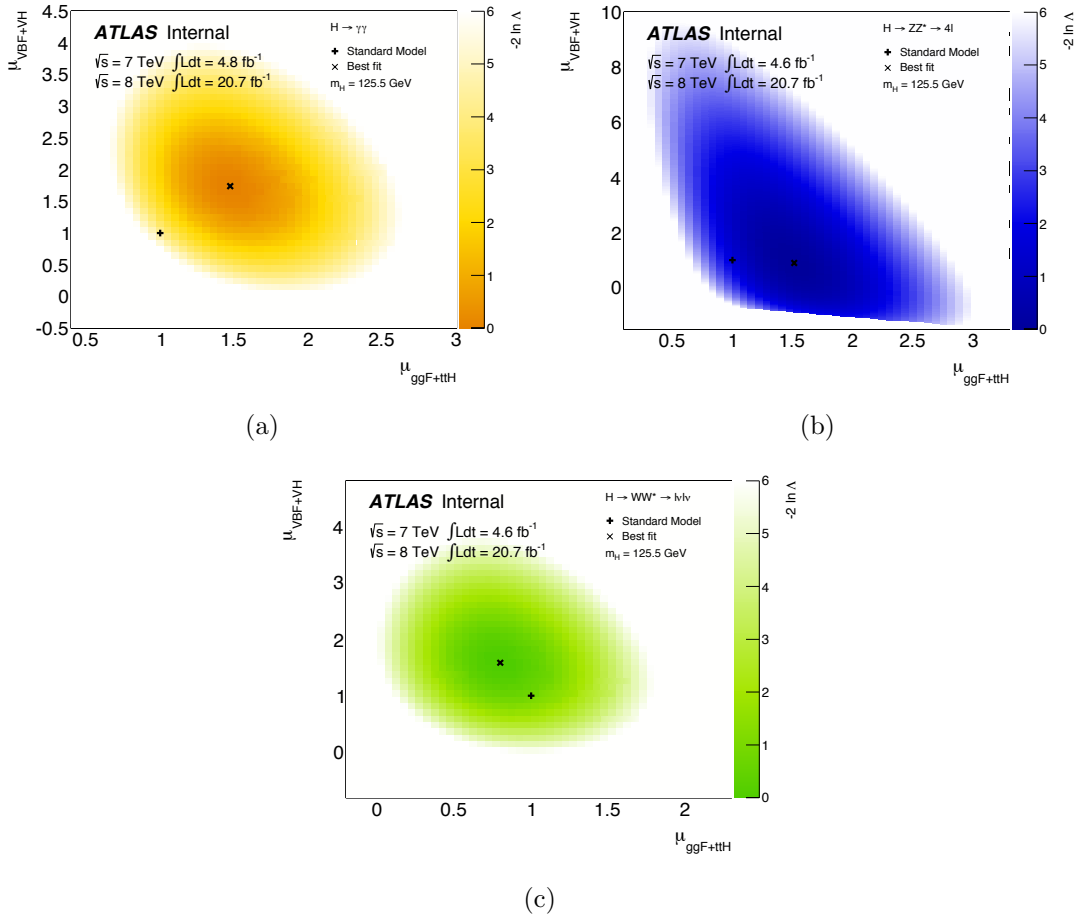


Figure 5.10: Profile likelihood scans for (a) $H \rightarrow \gamma\gamma$, (b) $H \rightarrow ZZ^* \rightarrow 4\ell$ and (c) $H \rightarrow WW^* \rightarrow \ell\nu\ell\nu$ in the plane $(\sigma_{ggF+ttH} \cdot BR, \sigma_{VBF+VH} \cdot BR)$.

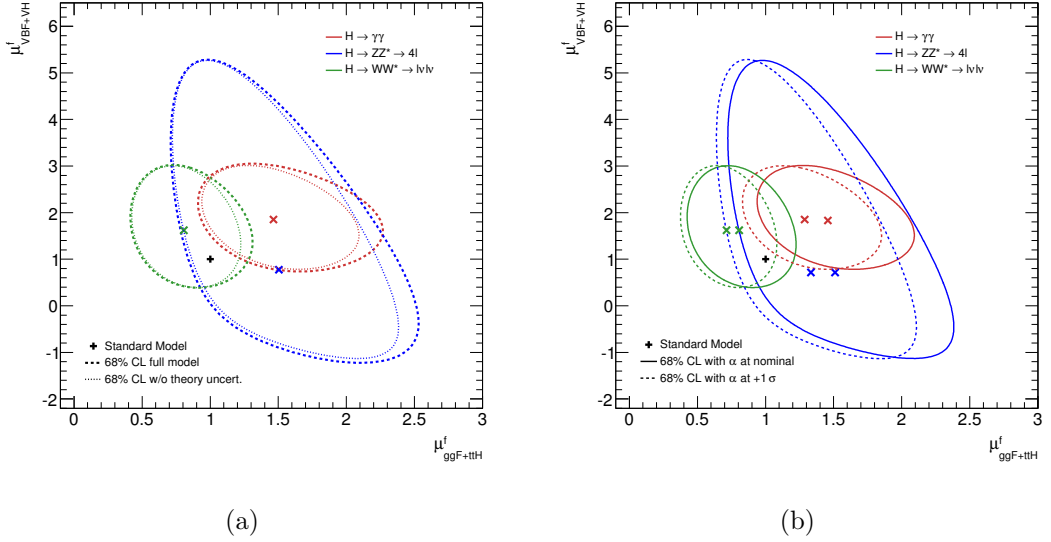


Figure 5.11: Simple models. (a) shows the full profile likelihood scan and compares it to a contour with fixed theory uncertainties. (b) shows how this fixed theory uncertainty contour moves and stretches when that uncertainty is fixed to a different value.

scales are shown in figure 5.12.

The full likelihood as used in ATLAS is

$$L_{\text{full}}(\boldsymbol{\mu}, \boldsymbol{\alpha}) = \prod_{c \in \text{category}} \left[\text{Pois}(n_c | \nu_c(\boldsymbol{\mu}, \boldsymbol{\alpha})) \prod_{e=1}^{n_c} f_e(x_e | \boldsymbol{\mu}, \boldsymbol{\alpha}) \right] \prod_{i \in \text{syst}} f_i(a_i | \alpha_i) \quad (5.17)$$

where $\nu_c(\boldsymbol{\mu}, \boldsymbol{\alpha})$ is the expected number of events for category c given by

$$\nu_c(\boldsymbol{\mu}, \boldsymbol{\alpha}) = \sum_{p,d} \mu_{pd} s_{cpd}(\boldsymbol{\alpha}) + b_c(\boldsymbol{\alpha}) \quad (5.18)$$

where p and d are labels for the production and decay modes. To factorize the unwanted uncertainties, the effective signal strength μ^{eff} is introduced such that

$$\nu_c(\boldsymbol{\mu}, \boldsymbol{\alpha}) \rightarrow \sum_{p,d} \mu_{cpd}^{\text{eff}} s_{cpd}(\boldsymbol{\alpha}_0) + b_c(\boldsymbol{\alpha}_0) \quad (5.19)$$

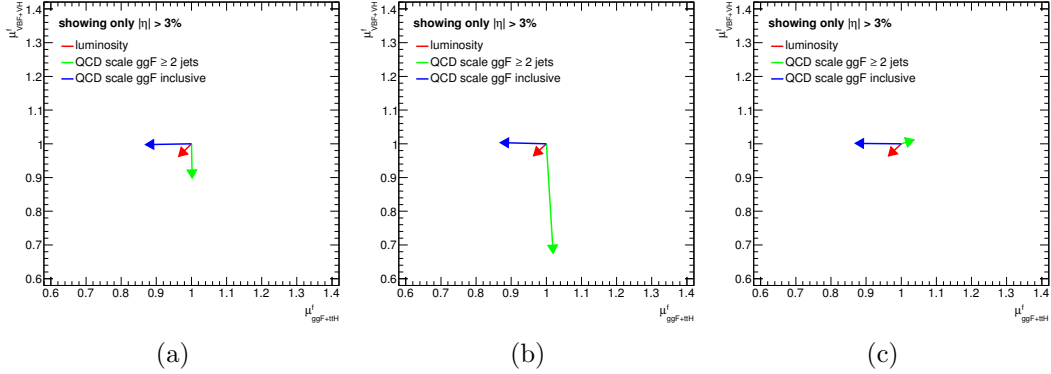


Figure 5.12: Response to variations of nuisance parameters in (a) $H \rightarrow \gamma\gamma$, (b) $H \rightarrow ZZ^* \rightarrow 4\ell$ and (c) $H \rightarrow WW^* \rightarrow \ell\nu\ell\nu$.

where the signal and background yields s and b are independent of $\boldsymbol{\alpha}$ and are only evaluated at the nominal values $\boldsymbol{\alpha}_0$. The dependence on $\boldsymbol{\alpha}$ is absorbed into $\boldsymbol{\mu}^{\text{eff}}(\boldsymbol{\mu}, \boldsymbol{\alpha})$.

The effective signal strength $\boldsymbol{\mu}^{\text{eff}}(\boldsymbol{\mu}, \boldsymbol{\alpha})$ is a function of $\boldsymbol{\mu}$ and $\boldsymbol{\alpha}$, but it can also be treated as a parameter $\boldsymbol{\mu}^{\text{eff}}$ and form the new effective likelihood $L_{\text{eff}}(\boldsymbol{\mu}^{\text{eff}})$.

At this point, the goal is to find a reparametrization $\boldsymbol{\mu}^{\text{eff}}(\boldsymbol{\mu}, \boldsymbol{\alpha})$ with parameters η and ϕ such that

$$L_{\text{full}}(\boldsymbol{\mu}, \boldsymbol{\alpha}) \approx L_{\text{recouple}}(\boldsymbol{\mu}, \boldsymbol{\alpha}) \quad (5.20)$$

where

$$L_{\text{recouple}}(\boldsymbol{\mu}, \boldsymbol{\alpha}) \equiv L_{\text{eff}}(\boldsymbol{\mu}^{\text{eff}}(\boldsymbol{\mu}, \boldsymbol{\alpha})) \cdot L_{\text{constr}}(\boldsymbol{\alpha}) \quad . \quad (5.21)$$

Reparametrization templates are inspired by the form of the full likelihood.

For the signal yield, a possible choice is

$$\begin{aligned} \mu_{pd}^{\text{eff}}(\boldsymbol{\mu}, \boldsymbol{\alpha}) &= \mu_{pd} \left[1 + \sum_i \eta_{pi} (\alpha_i - \alpha_{0,i}) \right] \\ \text{motivated by } s_{cpd}(\boldsymbol{\alpha}) &= s_{cpd}(\boldsymbol{\alpha}_0) \left[1 + \sum_i \eta_{pi} (\alpha_i - \alpha_{0,i}) \right] \end{aligned}$$

in the full likelihood. Similarly, for nuisance parameters that affect background rates

$$\begin{aligned} \mu_{pd}^{\text{eff}}(\boldsymbol{\mu}, \boldsymbol{\alpha}) &= \mu_{pd} + \frac{b_c(\boldsymbol{\alpha}_0)}{s_{cpd}(\boldsymbol{\alpha}_0)} \left[1 + \sum_i \phi_{ci} (\alpha_i - \alpha_{0,i}) \right] \\ \text{motivated by } b_c(\boldsymbol{\alpha}) &= b_c(\boldsymbol{\alpha}_0) \left[1 + \sum_i \phi_{ci} (\alpha_i - \alpha_{0,i}) \right] . \end{aligned}$$

An interesting special case arises when an uncertainty of one production mode affects the signal strength measurement of another production mode. This happens for example in VBF-optimized analyses that usually have a large ggF contamination. For “cross-talk” nuisance parameters, a possible template is

$$\mu_{pd}^{\text{eff}}(\boldsymbol{\mu}, \boldsymbol{\alpha}) = \mu_{pd} + \sum_{i,p'} \mu_{p'd} \eta_{pi}^{p'} (\alpha_i - \alpha_{0,i}) .$$

Considering all the cases, a general template could be of the form

$$\mu_{pd}^{\text{eff}}(\boldsymbol{\mu}, \boldsymbol{\alpha}) = \mu_{pd} + \sum_{i,p'} \mu_{p'd} \eta_{pi}^{p'} (\alpha_i - \alpha_{0,i}) + \sum_i \phi_i (\alpha_i - \alpha_{0,i}) . \quad (5.22)$$

The parameters in this template need to be determined. Using knowledge about the physical situation, it might be possible to reduce the number of template parameters below $n_p \cdot n_\alpha$ for n_p production modes and n_α nuisance parameters.

In that case, the remaining parameters can be determined using the covariance matrix at the best fit point.

For general templates, the local information contained in the covariance matrix is not enough and more global information of the full likelihood needs to be used. For example, a loss function

$$Loss(\boldsymbol{\eta}) = \int d\boldsymbol{\mu} d\boldsymbol{\alpha} \pi(\boldsymbol{\mu}, \boldsymbol{\alpha}) |L_{\text{full}}(\boldsymbol{\mu}, \boldsymbol{\alpha}) - L_{\text{recouple}}(\boldsymbol{\mu}, \boldsymbol{\alpha}; \boldsymbol{\eta})|^2 \quad (5.23)$$

can be defined and minimized with respect to the template parameters $\boldsymbol{\eta}$. $\pi(\boldsymbol{\mu}, \boldsymbol{\alpha})$ is a weight function. One possibility is to treat $\pi(\boldsymbol{\mu}, \boldsymbol{\alpha})$ as a posterior obtained using a baseline constraint term: $\pi(\boldsymbol{\mu}, \boldsymbol{\alpha}) \propto L_{\text{main}}(\boldsymbol{\mu}, \boldsymbol{\alpha}) L_{\text{constr}}(\boldsymbol{\alpha})$. In practice, this means that the integral in the loss function can be obtained using MCMC. Here MCMC is only a tool to generate sampling points to be used to obtain parameter values for the template. This does not make the whole method Bayesian.

A demo that shows recoupled coupling results with different assumptions on the size of theory uncertainties is shown in figure 5.13. A combination of the full likelihood functions is also shown for comparison. The demo is available at <https://github.com/svenkreiss/recoupledDemo>. Most of the complexities of the likelihoods are encoded in the effective likelihood. Therefore, the demo runs in a few minutes on a standard computer whereas the full likelihood scans usually run for a few hours.

This is a powerful procedure for approximating likelihoods and it has a stable software implementation. For the case of a Gaussian likelihood and linear systematic effects, it is similar to the Best Linear Unbiased Estimate (BLUE) method [165, 166]. It is possible to construct combined likelihood functions where

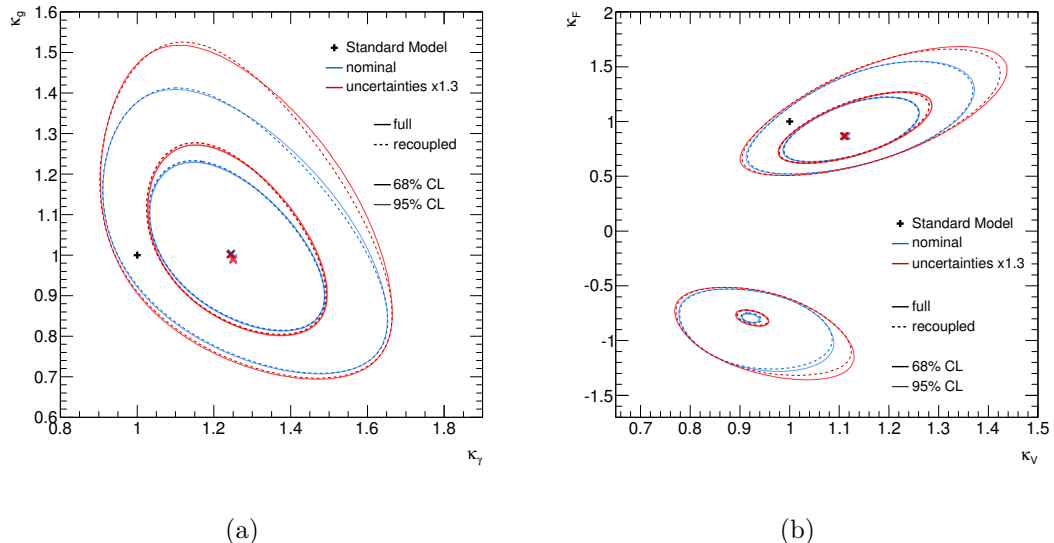


Figure 5.13: Example coupling combinations with nominal and $\times 1.3$ inflated theory uncertainties for (a) a $(\kappa_\gamma, \kappa_g)$ model and (b) a (κ_V, κ_F) model. The dashed lines are contours of a true full likelihood combination for comparison.

one Higgs decay channel is implemented using a full likelihood and another Higgs decay channel uses the effective likelihood procedure shown here. The effective likelihood is also a natural interface to publish future experimental results.

Chapter 6

Conclusion

The newly discovered Higgs boson has a mass of

$$m_H = 125.5 \pm 0.2(\text{stat})^{+0.5}_{-0.6}(\text{sys}) \quad (6.1)$$

and is overall consistent with a CP -even scalar as predicted for the Higgs boson in the Standard Model. The measured overall signal strength is

$$\mu = 1.30 \pm 0.12(\text{stat})^{+0.14}_{-0.11}(\text{sys}) . \quad (6.2)$$

The existence of VBF production of Higgs bosons is established at the 4.1σ level. No significant deviations in any of the studies of the couplings of the Higgs boson to other particles has been observed so far. As more data is collected in the coming years, the precision of these measurements will increase and will allow to probe the Standard Model prediction more carefully. The expected relative errors for benchmark coupling parameters are shown in table 6.1.

In the context of this thesis, methods for data-driven studies of observed colli-

Luminosity	300 fb^{-1}	3000 fb^{-1}
Coupling parameter	7-parameter fit	
κ_γ	5 – 7%	2 – 5%
κ_g	6 – 8%	3 – 5%
κ_W	4 – 6%	2 – 5%
κ_Z	4 – 6%	2 – 4%
κ_u	14 – 15%	7 – 10%
κ_d	10 – 13%	4 – 7%
κ_l	6 – 8%	2 – 5%
Γ_H	12 – 15%	5 – 8%

Table 6.1: Expected precision for benchmark coupling parameters per experiment at the LHC for integrated luminosities of 300 fb^{-1} and 3000 fb^{-1} . The range is obtained from two assumptions on the systematic and theory uncertainties [13].

sion events were shown and applied to ATLAS data. Advanced statistical modeling techniques were studied which resulted in the official signal model for the ATLAS $H \rightarrow ZZ^* \rightarrow 4\ell$ analysis. The analyses to measure the Higgs boson mass and their progress after the discovery of a Higgs boson were shown.

The question of naturalness to explain a weak-scale Higgs mass still remains open. The next run of the LHC program at $\sqrt{s} = 13 \text{ TeV}$ that starts in 2015 will hopefully shed light on the underlying physical principles and unveil hints for a theory like supersymmetry or something unexpected will be discovered.

Bibliography

- [1] LHC Higgs Cross Section Working Group, S. Dittmaier, C. Mariotti, G. Passarino, and R. Tanaka (Eds.), *Handbook of LHC Higgs cross sections: 1. Inclusive observables*, CERN-2011-002 (CERN, Geneva, 2011) , [arXiv:1101.0593 \[hep-ph\]](https://arxiv.org/abs/1101.0593).
- [2] *ATLAS overview*, <http://cds.cern.ch/record/1095924>. ATLAS Experiment, Copyright CERN 2008.
- [3] *Inner detector perspective layout*,
http://www.ge.infn.it/~rossi/leoweb/ID_perspective_layout.jpg.
- [4] *Inner detector: Pixel*, <http://cds.cern.ch/record/1095925>. ATLAS Experiment, Copyright CERN 2008.
- [5] *Liquid argon pulse shape*, <http://www-library.desy.de/preparch/desy/proc/proc10-01/meng.pdf>.
- [6] *Barrel toroid*, <http://cds.cern.ch/record/910381>. Copyright CERN 2005.
- [7] *Muon system schematic*, <http://arxiv.org/pdf/1006.4384v2.pdf>.

- [8] *Particle identification*, <https://cds.cern.ch/record/1505342>. ATLAS Experiment, Copyright CERN 2013.
- [9] ATLAS Collaboration, *Performance of the ATLAS Trigger System in 2010*, Eur. Phys. J. **C 72** (2012) 1849, [arXiv:1110.1530 \[hep-ex\]](https://arxiv.org/abs/1110.1530).
- [10] ATLAS Collaboration, *Measurements of the properties of the Higgs-like boson in the four lepton decay channel with the ATLAS detector using 25 fb⁻¹ of proton-proton collision data*, ATLAS-CONF-2013-013, ATLAS-COM-CONF-2013-018 (2013) .
- [11] HSG1, HSG2, HSG3, and HSG7, *Properties of the Excess Observed in the Search for the Standard Model Higgs Boson*, Tech. Rep. ATL-COM-PHYS-2012-1053, CERN, Geneva, Jul, 2012.
- [12] ATLAS Collaboration, G. Aad et al., *Observation of a new particle in the search for the Standard Model Higgs boson with the ATLAS detector at the LHC*, Phys.Lett. **B716** (2012) 1–29, [arXiv:1207.7214 \[hep-ex\]](https://arxiv.org/abs/1207.7214).
- [13] S. Dawson, A. Gritsan, H. Logan, J. Qian, C. Tully, et al., *Higgs Working Group Report of the Snowmass 2013 Community Planning Study*, [arXiv:1310.8361 \[hep-ex\]](https://arxiv.org/abs/1310.8361).
- [14] S. L. Glashow, *Partial-symmetries of weak interactions*, Nucl. Phys. **22** (1961) no. 4, 579.
- [15] S. Weinberg, *A model of leptons*, Phys. Rev. Lett. **19** (1967) 1264.
- [16] A. Salam, *in Elementary Particle Theory*, p. 367. Almqvist and Wiksell, Stockholm, 1968.

- [17] G. 't Hooft and M. Veltman, *Regularization and Renormalization of Gauge Fields*, Nucl. Phys. **B44** (1972) 189.
- [18] F. Englert and R. Brout, *Broken symmetry and the mass of gauge vector mesons*, Phys. Rev. Lett. **13** (1964) 321.
- [19] P. W. Higgs, *Broken symmetries, massless particles and gauge fields*, Phys. Lett. **12** (1964) 132.
- [20] P. W. Higgs, *Broken symmetries and the masses of gauge bosons*, Phys. Rev. Lett. **13** (1964) 508.
- [21] G. S. Guralnik, C. R. Hagen, and T. W. B. Kibble, *Global conservation laws and massless particles*, Phys. Rev. Lett. **13** (1964) 585.
- [22] P. W. Higgs, *Spontaneous symmetry breakdown without massless bosons*, Phys. Rev. **145** (1966) 1156.
- [23] T. W. B. Kibble, *Symmetry breaking in non-Abelian gauge theories*, Phys. Rev. **155** (1967) 1554.
- [24] L. Evans and P. Bryant, *LHC Machine*, JINST **3** (2008) S08001.
- [25] F. Halzen and A. Martin, *Quarks and leptons: an introductory course in modern particle physics*. Wiley, 1984.
<http://books.google.com/books?id=zwDvAAAAMAAJ>.
- [26] The LEP Electroweak Working Group.
<http://lepewwg.web.cern.ch/LEPEWWG/>, 2010.

- [27] LEP Working Group for Higgs boson searches, ALEPH, DELPHI, L3 and OPAL Collaborations, *Search for the standard model Higgs boson at LEP*, Phys. Lett. **B 565** (2003) 61.
- [28] CDF and D0 Collaboration, T. Aaltonen et al., *Combination of Tevatron searches for the standard model Higgs boson in the W+W- decay mode*, Phys. Rev. Lett. **104** (2010) 061802, arXiv:1001.4162 [hep-ex].
- [29] CDF Collaboration, T. Aaltonen et al., *Combined search for the standard model Higgs boson decaying to a bb pair using the full CDF data set*, submitted to Phys. Rev. Lett. (2012) , arXiv:1207.1707 [hep-ex].
- [30] D0 Collaboration Collaboration, V. M. Abazov et al., *Combined search for the standard model Higgs boson decaying to bb} using the D0 Run II data set*, Phys.Rev.Lett. **109** (2012) 121802, arXiv:1207.6631 [hep-ex].
- [31] CDF Collaboration, D0 Collaboration Collaboration, T. Aaltonen et al., *Evidence for a particle produced in association with weak bosons and decaying to a bottom-antibottom quark pair in Higgs boson searches at the Tevatron*, Phys.Rev.Lett. **109** (2012) 071804, arXiv:1207.6436 [hep-ex].
- [32] Particle Data Group Collaboration, J. Beringer et al., *Review of Particle Physics (RPP): Status of Higgs Boson Physics*, <http://pdg.lbl.gov/2013/reviews/rpp2013-rev-higgs-boson.pdf>, 2013.
- [33] ATLAS Collaboration, *Detector and Physics Performance Technical Design Report*, CERN-LHCC/99-14/15 (1999) .
- [34] *About CERN*, <http://home.web.cern.ch/about>. Accessed: 2014-04-01.

- [35] F. Hugging, *The ATLAS Pixel Detector*, IEEE Transactions on Nuclear Science **53** (June, 2006) 1732–1736, [physics/0412138](#).
- [36] M. Marcisovsky, *ATLAS Insertable B-Layer*, Tech. Rep. ATL-INDET-PROC-2009-012, CERN, Geneva, Sep, 2009.
- [37] ATLAS Collaboration, G. Aad et al., *Combined search for the Standard Model Higgs boson in pp collisions at $\sqrt{s} = 7$ TeV with the ATLAS detector*, Phys.Rev. **D86** (2012) 032003, [arXiv:1207.0319 \[hep-ex\]](#).
- [38] ATLAS and CMS Collaboration, *Procedure for the LHC Higgs boson search combination in Summer 2011*, ATL-PHYS-PUB-2011-11/CMS NOTE-2011/005 (2011) .
- [39] L. Moneta, K. Belasco, K. S. Cranmer, S. Kreiss, A. Lazzaro, et al., *The RooStats Project*, PoS **ACAT2010** (2010) 057, [arXiv:1009.1003 \[physics.data-an\]](#).
- [40] K. Cranmer, G. Lewis, L. Moneta, A. Shibata, and W. Verkerke, *HistFactory: A tool for creating statistical models for use with RooFit and RooStats*, Tech. Rep. CERN-OPEN-2012-016, New York U., New York, Jan, 2012.
- [41] W. Verkerke and D. Kirkby, *The RooFit toolkit for data modelling*, Tech. Rep. physics/0306116, SLAC, Stanford, CA, Jun, 2003.
[arXiv:physics/0306116v1 \[physics.data-an\]](#).
- [42] ATLAS Collaboration, *Observation of an excess of events in the search for the Standard Model Higgs boson in the $H \rightarrow ZZ^{(*)} \rightarrow 4\ell$ channel with the*

ATLAS detector., ATLAS-CONF-2012-092, ATLAS-COM-CONF-2012-106
(2012) .

- [43] ATLAS Collaboration, *Updated results and measurements of properties of the new Higgs-like particle in the four lepton decay channel with the ATLAS detector*, ATLAS-CONF-2012-169, ATLAS-COM-CONF-2012-204 (2012) .
- [44] C. Anastopoulos et al., *Observation of an excess of events in the search for the Standard Model Higgs boson in the $H \rightarrow ZZ^* \rightarrow 4l$ channel with the ATLAS detector*, Tech. Rep. ATLAS-COM-CONF-2012-204, CERN, Geneva, Dec, 2012.
- [45] C. Anastopoulos et al., *Measurements of the properties of the Higgs-like boson in the four lepton decay channel with the ATLAS detector using 25 fb⁻¹ of proton-proton collision data*, Tech. Rep. ATLAS-COM-CONF-2013-018, CERN, Geneva, Feb, 2013.
- [46] C. Anastopoulos et al., *Observation of a new particle in the search for the Standard Model Higgs boson in the $H \rightarrow ZZ^* \rightarrow 4l$ channel and its properties using 4.6 fb⁻¹ and 20.7 fb⁻¹ of proton-proton collisions at $\sqrt{s} = 7$ TeV and 8 TeV, respectively, recorded with the ATLAS detector.*, Tech. Rep. ATL-COM-PHYS-2013-146, CERN, Geneva, Oct, 2013.
- [47] C. Anastopoulos et al., *Observation of a new particle in the search for the Standard Model Higgs boson in the $H \rightarrow ZZ^* \rightarrow 4l$ channel : limits on the for VBF and VH production of the new particle and High mass search using 4.6 fb⁻¹ and 20.7 fb⁻¹ of proton-proton collisions at $\sqrt{s} = 7$ TeV and 8 TeV*,

respectively, recorded with the ATLAS detector., Tech. Rep.

ATL-COM-PHYS-2013-145, CERN, Geneva, Oct, 2013.

- [48] C. Anastopoulos et al., *Observation of a new particle in the search for the Standard Model Higgs boson in the $H \rightarrow ZZ^* \rightarrow 4l$ channel : mass and signal strength measurement using 4.6 fb $^{-1}$ and 20.7 fb $^{-1}$ of proton-proton collisions at $s = 7$ TeV and 8 TeV, respectively, recorded with the ATLAS detector.*, Tech. Rep. ATL-COM-PHYS-2013-144, CERN, Geneva, Oct, 2013.
- [49] S. Agostinelli et al., GEANT4, *a simulation toolkit*, Nucl. Instrum. Meth. **A 506** (2003) 250.
- [50] ATLAS, *The ATLAS simulation infrastructure*, Eur. Phys. J. **C 70** (2010) 823, arXiv:1005.4568 [hep-ph].
- [51] S. Alioli, P. Nason, C. Oleari, and E. Re, *NLO Higgs boson production via gluon fusion matched with shower in POWHEG*, JHEP **04** (2009) 002.
- [52] P. Nason and C. Oleari, *NLO Higgs boson production via vector-boson fusion matched with shower in POWHEG*, JHEP **02** (2010) 037.
- [53] G. Bozzi, S. Catani, D. de Florian, and M. Grazzini, *Transverse-momentum resummation and the spectrum of the Higgs boson at the LHC*, Nucl. Phys. **B 737** (2006) 73.
- [54] E. Bagnaschi, G. Degrassi, P. Slavich, and A. Vicini, *Higgs production via gluon fusion in the POWHEG approach in the SM and in the MSSM*, JHEP **1202** (2012) 88.

- [55] T. Sjostrand, S. Mrenna, and P. Z. Skands, *PYTHIA 6.4 physics and manual*, JHEP **0605** (2006) 026.
- [56] T. Sjostrand, S. Mrenna, and P. Z. Skands, *A Brief Introduction to PYTHIA 8.1*, Comput. Phys. Commun. **178** (2008) 852.
- [57] P. Golonka and Z. Was, *PHOTOS Monte Carlo: A Precision tool for QED corrections in Z and W decays*, Eur. Phys. J. C **45** (2006) 97.
- [58] N. Davidson, T. Przedzinski, and Z. Was, *PHOTOS interface in C++: technical and physics documentation*, arXiv:1011.0937 [hep-ph].
- [59] LHC Higgs Cross Section Working Group, S. Dittmaier, C. Mariotti, G. Passarino, and R. Tanaka (Eds.), *Handbook of LHC Higgs cross sections: 1. Inclusive observables*, CERN-2011-002 (2011) , arXiv:1101.0593 [hep-ph].
- [60] LHC Higgs Cross Section Working Group, S. Dittmaier, C. Mariotti, G. Passarino, and R. Tanaka (Eds.), *Handbook of LHC Higgs Cross Sections: 2. Differential Distributions*, CERN-2012-002 (CERN, Geneva, 2012) , arXiv:1201.3084 [hep-ph].
- [61] A. Djouadi, M. Spira, and P. M. Zerwas, *Production of Higgs bosons in proton colliders: QCD corrections*, Phys. Lett. B **264** (1991) 440.
- [62] S. Dawson, *Radiative corrections to Higgs boson production*, Nucl. Phys. B **359** (1991) 283.
- [63] M. Spira, A. Djouadi, D. Graudenz, and P. M. Zerwas, *Higgs boson production at the LHC*, Nucl. Phys. **B453** (1995) 17.

- [64] R. Harlander and W. B. Kilgore, *Next-to-next-to-leading order Higgs production at hadron colliders*, Phys. Rev. Lett. **88** (2002) 201801.
- [65] C. Anastasiou and K. Melnikov, *Higgs boson production at hadron colliders in NNLO QCD*, Nucl. Phys. **B646** (2002) 220.
- [66] V. Ravindran, J. Smith, and W. L. van Neerven, *NNLO corrections to the total cross section for Higgs boson production in hadron hadron collisions*, Nucl. Phys. **B665** (2003) 325.
- [67] S. Catani, D. de Florian, M. Grazzini, and P. Nason, *Soft-gluon re-summation for Higgs boson production at hadron colliders*, JHEP **0307** (2003) 028.
- [68] U. Aglietti, R. Bonciani, G. Degrassi, and A. Vicini, *Two-loop light fermion contribution to Higgs production and decays*, **595** (2004) 432, arXiv:hep-ph/0404071.
- [69] S. Actis, G. Passarino, C. Sturm, and S. Uccirati, *NLO electroweak corrections to Higgs boson production at hadron colliders*, Phys. Lett. B **670** (2008) 12.
- [70] D. de Florian and M. Grazzini, *Higgs production at the LHC: updated cross sections at $\sqrt{s} = 8$ TeV*, arXiv:1206.4133 [hep-ph].
- [71] C. Anastasiou, S. Buehler, F. Herzog, and A. Lazopoulos, *Inclusive Higgs boson cross-section for the LHC at 8 TeV*, JHEP **1204** (2012) 004.
- [72] J. Baglio and A. Djouadi, *Higgs production at the lHC*, JHEP **1103** (2011) 055.

- [73] M. Ciccolini, A. Denner, and S. Dittmaier, *Strong and electroweak corrections to the production of Higgs+2jets via weak interactions at the LHC*, Phys. Rev. Lett. **99** (2007) 161803.
- [74] M. Ciccolini, A. Denner, and S. Dittmaier, *Electroweak and QCD corrections to Higgs production via vector-boson fusion at the LHC*, Phys. Rev. **D 77** (2008) 013002.
- [75] K. Arnold, M. Bahr, G. Bozzi, F. Campanario, C. Englert, et al., *VBFNLO: A parton level Monte Carlo for processes with electroweak bosons*, Comput. Phys. Commun. **180** (2009) 1661.
- [76] T. Han and S. Willenbrock, *QCD correction to the $pp \rightarrow WH$ and ZH total cross sections*, Phys. Lett. **B 273** (1991) 167.
- [77] O. Brein, A. Djouadi, and R. Harlander, *NNLO QCD corrections to the Higgs-strahlung processes at hadron colliders*, Phys. Lett. **B 579** (2004) 149.
- [78] M. L. Ciccolini, S. Dittmaier, and M. Kramer, *Electroweak radiative corrections to associated WH and ZH production at hadron colliders*, Phys. Rev. **D 68** (2003) 073003.
- [79] W. Beenakker et al., *Higgs Radiation Off Top Quarks at the Tevatron and the LHC*, Phys. Rev. Lett. **87** (2001) 201805.
- [80] W. Beenakker et al., *NLO QCD corrections to $t\bar{t}H$ production in hadron collisions*, Nucl. Phys. **B 653** (2003) 151.

- [81] S. Dawson, L. H. Orr, L. Reina, and D. Wackerlo, *Next-to-leading order QCD corrections to $pp \rightarrow t\bar{t}h$ at the CERN Large Hadron Collider*, Phys. Rev. **D 67** (2003) 071503.
- [82] S. Dawson, C. Jackson, L. H. Orr, L. Reina, and D. Wackerlo, *Associated Higgs production with top quarks at the Large Hadron Collider: NLO QCD corrections*, Phys. Rev. **D 68** (2003) 034022.
- [83] A. Djouadi, J. Kalinowski, and M. Spira, *HDECAY: A program for Higgs boson decays in the standard model and its supersymmetric extension*, Comput. Phys. Commun. **108** (1998) 56.
- [84] A. Bredenstein, A. Denner, S. Dittmaier, and M. M. Weber, *Precise predictions for the Higgs-boson decay $H \rightarrow WW/ZZ \rightarrow 4$ leptons*, Phys. Rev. **D74** (2006) 013004, [arXiv:hep-ph/0604011](https://arxiv.org/abs/hep-ph/0604011).
- [85] A. Bredenstein, A. Denner, S. Dittmaier, and M. M. Weber, *Radiative corrections to the semileptonic and hadronic Higgs-boson decays $H \rightarrow WW/ZZ \rightarrow 4$ fermions*, JHEP **0702** (2007) 080.
- [86] M. Botje, J. Butterworth, A. Cooper-Sarkar, A. de Roeck, J. Feltesse, et al., *The PDF4LHC Working Group Interim Recommendations*, [arXiv:1101.0538 \[hep-ph\]](https://arxiv.org/abs/1101.0538).
- [87] H.-L. Lai et al., *New parton distributions for collider physics*, Phys. Rev. **D 82** (2010) 074024.
- [88] A. Martin, W. Stirling, R. Thorne, and G. Watt, *Parton distributions for the LHC*, Eur.Phys.J. **C63** (2009) 189.

- [89] R. D. Ball et al., *Impact of heavy quark masses on parton distributions and LHC phenomenology*, Nucl. Phys. **B** **849** (2011) 296, arXiv:1101.1300 [hep-ph].
- [90] LHC Higgs Cross Section Working Group, S. Dittmaier, C. Mariotti, G. Passarino, and R. Tanaka (Eds.), *Handbook of LHC Higgs Cross Sections: 2. Differential distributions*, CERN-2012-002 (CERN, Geneva, 2012) , arXiv:1201.3084 [hep-ph].
- [91] G. Passarino, *Higgs interference effects in $gg \rightarrow ZZ$ and their uncertainty*, JHEP **1208** (2012) 146, arXiv:1206.3824 [hep-ph].
- [92] N. Kauer and G. Passarino, *Inadequacy of zero-width approximation for a light Higgs boson signal*, JHEP **1208** (2012) 116, arXiv:1206.4803 [hep-ph].
- [93] J. M. Campbell, R. K. Ellis, and C. Williams, *Vector boson pair production at the LHC*, JHEP **07** (2011) 018, arXiv:1105.0020 [hep-ph].
- [94] T. Gleisberg et al., *Event generation with SHERPA 1.1*, JHEP **02** (2009) 007, arXiv:0811.4622 [hep-ph].
- [95] S. Jadach, Z. Was, R. Decker, and J. H. Kuhn, *The tau decay library TAUOLA: Version 2.4*, Comput. Phys. Commun. **76** (1993) 361.
- [96] P. Golonka et al., *The tauola-photos-F environment for the TAUOLA and PHOTOS packages, release II*, Comput. Phys. Commun. **174** (2006) 818.
- [97] M. L. Mangano et al., *ALPGEN, a generator for hard multiparton processes in hadronic collisions*, JHEP **07** (2003) 001, arXiv:hep-ph/0206293.

- [98] M. L. Mangano, M. Moretti, F. Piccinini, and M. Treccani, *Matching matrix elements and shower evolution for top-quark production in hadronic collisions*, JHEP **01** (2007) 013, arXiv:hep-ph/0611129 [hep-ph].
- [99] K. Melnikov and F. Petriello, *Electroweak gauge boson production at hadron colliders through $O(\alpha_s^2)$* , Phys. Rev. **D 74** (2006) 114017, arXiv:hep-ph/0609070.
- [100] C. Anastasiou, L. J. Dixon, K. Melnikov, and F. Petriello, *High precision QCD at hadron colliders: Electroweak gauge boson rapidity distributions at NNLO*, Phys. Rev. **D 69** (2004) 094008.
- [101] S. Frixione, P. Nason, and B. R. Webber, *Matching NLO QCD and parton showers in heavy flavour production*, JHEP **08** (2003) 007.
- [102] M. Aliev et al., *HATHOR: HAdronic Top and Heavy quarks crOss section calculatoR*, Comput. Phys. Commun. **182** (2011) 1034, arXiv:1007.1327 [hep-ph].
- [103] G. Corcella et al., *HERWIG 6: An event generator for hadron emission reactions with interfering gluons (including super-symmetric processes)*, JHEP **01** (2001) 010.
- [104] J. M. Butterworth, J. R. Forshaw, and M. H. Seymour, *Multiparton interactions in photoproduction at HERA*, Z. Phys. **C 72** (1996) 637.
- [105] T. Sjostrand, S. Mrenna, and P. Z. Skands, *PYTHIA 6.4 physics and manual*, JHEP **0605** (2006) 026.

- [106] T. Sjostrand, S. Mrenna, and P. Z. Skands, *A brief introduction to PYTHIA 8.1*, Comput. Phys. Commun. **178** (2008) 852–867, arXiv:0710.3820 [hep-ph].
- [107] ATLAS Collaboration, *Electron performance measurements with the ATLAS detector using the 2010 LHC proton-proton collision data*, Eur. Phys. J. C **72** (2012) 1909, arXiv:1110.3174 [hep-ex].
- [108] ATLAS Collaboration, *Improved electron reconstruction in ATLAS using the Gaussian Sum Filter-based model for bremsstrahlung*, ATLAS-CONF-2012-047 (2012) .
<http://cdsweb.cern.ch/record/1449796>.
- [109] ATLAS Collaboration, *Measurement of the $W \rightarrow l\nu$ and $Z/\gamma \rightarrow ll$ production cross sections in proton-proton collisions at $\sqrt{s} = 7$ TeV with the ATLAS detector*, JHEP **1012** (2010) 060, arXiv:1010.2130 [hep-ex].
- [110] W. Lampl, S. Laplace, D. Lelas, P. Loch, H. Ma, S. Menke, S. Rajagopalan, D. Rousseau, S. Snyder, and G. Unal, *Calorimeter Clustering Algorithms: Description and Performance*, ATL-LARG-PUB-2008-002 (2008) .
<http://cdsweb.cern.ch/record/1099735>.
- [111] M. Cacciari, G. P. Salam, and G. Soyez, *Anti- k_t jet clustering algorithm*, JHEP **04** (2008) 063.
- [112] ATLAS Collaboration, *Measurement of the ZZ Production Cross Section and Limits on Anomalous Neutral Triple Gauge Couplings in Proton-Proton Collisions at $\sqrt{s} = 7$ TeV with the ATLAS Detector*, Phys.

- Rev. Lett. **108** (Jan, 2012) 041804.
[http://link.aps.org/doi/10.1103/PhysRevLett.108.041804.](http://link.aps.org/doi/10.1103/PhysRevLett.108.041804)
- [113] A. Read, *Linear interpolation of histograms*, Nuclear Instruments and Methods in Physics Research Section A: Accelerators, Spectrometers, Detectors and Associated Equipment **425** (1999) no. 12, 357 – 360. <http://www.sciencedirect.com/science/article/pii/S0168900298013473>.
- [114] K. Cranmer, G. Lewis, L. Moneta, A. Shibata, and W. Verkerke, *HistFactory: A tool for creating statistical models for use with RooFit and RooStats*, CERN-OPEN-2012-016 (Jan, 2012) .
<http://cdsweb.cern.ch/record/1456844>.
- [115] ATLAS Collaboration, *Observation of a new particle in the search for the Standard Model Higgs boson with the ATLAS detector at the LHC*, Phys. Lett. **B 716** (2012) 1, arXiv:1207.7214 [hep-ex].
- [116] K. S. Cranmer, *Kernel estimation in high-energy physics*, Comput.Phys.Commun. **136** (2001) 198–207, arXiv:hep-ex/0011057 [hep-ex].
- [117] M. P. Wand and M. C. Jones, *Kernel Smoothing (Chapman & Hall/CRC Monographs on Statistics & Applied Probability)*. Chapman and Hall/CRC, 1 ed., Dec., 1994.
- [118] K. Cranmer, *Statistics for the LHC: Progress, Challenges and Future*, PHYSTAT-LHC Workshop on Statistical Issues for LHC Physics (2008) . oai:cds.cern.ch:1021125.

- [119] ATLAS Collaboration Collaboration, *An update to the combined search for the Standard Model Higgs boson with the ATLAS detector at the LHC using up to 4.9 fb⁻¹ of pp collision data at $\sqrt{s} = 7$ TeV*, Tech. Rep. ATLAS-CONF-2012-019, CERN, Geneva, Mar, 2012.
- [120] ATLAS Collaboration, *Observation of an Excess of Events in the Search for the Standard Model Higgs boson with the ATLAS detector at the LHC*, ATLAS-CONF-2012-093, ATLAS-COM-CONF-2012-120 (2012) .
- [121] ATLAS Collaboration, G. Aad et al., *A particle consistent with the Higgs Boson observed with the ATLAS Detector at the Large Hadron Collider*, Science **338** (2012) 1576–1582.
- [122] ATLAS Collaboration, *Combined search for the Standard Model Higgs boson using up to 4.9 fb⁻¹ of pp collision data at $\sqrt{s} = 7$ TeV with the ATLAS detector at the LHC*, Phys. Lett. **B 710** (2012) 49, arXiv:1202.1408 [hep-ex].
- [123] S. Kreiss, *Standard Model Higgs Combination and Properties*, Tech. Rep. ATL-COM-PHYS-2012-1412, CERN, Geneva, Sep, 2012.
- [124] G. Cowan, K. Cranmer, E. Gross, and O. Vitells, *Asymptotic formulae for likelihood-based tests of new physics*, Eur. Phys. J. **C 71** (2011) 1554.
- [125] A. L. Read, *Presentation of search results: The CL_s technique*, J. Phys. G **28** (2002) 2693.
- [126] E. Gross and O. Vitells, *Trial factors for the look elsewhere effect in high energy physics*, Eur. Phys. J. **C 70** (2010) 525.

- [127] L. J. Dixon and M. S. Siu, *Resonance continuum interference in the diphoton Higgs signal at the LHC*, Phys. Rev. Lett. **90** (2003) 252001.
- [128] J. Gaiser, *Ph.D. thesis*, SLAC-R-0255 (1982) Appendix F.
- [129] A. J. Barr, B. Gripaios, and C. G. Lester, *Measuring the Higgs boson mass in dileptonic W-boson decays at hadron colliders*, JHEP **0907** (2009) 072.
- [130] M. Dittmar and H. Dreiner, *How to find a Higgs boson with a mass between 155 and 180 GeV at the CERN LHC*, Phys. Rev. D **55** (Jan, 1997) 167–172. <http://link.aps.org/doi/10.1103/PhysRevD.55.167>.
- [131] ATLAS Collaboration, *Commissioning of the ATLAS high-performance b-tagging algorithms in the 7 TeV collision data*, ATLAS-CONF-2011-102 (2011) . <http://cds.cern.ch/record/1369219>.
- [132] ATLAS Collaboration, *Jet energy measurement with the ATLAS detector in proton-proton collisions at $\sqrt{s} = 7$ TeV*, Eur. Phys. J. C **73** (2013) 2304, [arXiv:1112.6426 \[hep-ex\]](https://arxiv.org/abs/1112.6426).
- [133] ATLAS Collaboration, *Observation of an excess of events in the search for the Standard Model Higgs boson in the $H \rightarrow ZZ^{(*)} \rightarrow 4\ell$ channel with the ATLAS detector*, ATLAS-CONF-2012-092 (Jul, 2012) . <http://cdsweb.cern.ch/record/1460411>.
- [134] ATLAS Collaboration, *Search for a Standard Model Higgs boson in the $H \rightarrow ZZ \rightarrow ll\nu\nu$ decay channel using 4.7 fb^{-1} of $\sqrt{s} = 7$ TeV data with the ATLAS detector*, submitted to Phys. Lett. B (2012) , [arXiv:1205.6744 \[hep-ex\]](https://arxiv.org/abs/1205.6744).

- [135] ATLAS Collaboration, *Search for a Standard Model Higgs boson in the mass range 200-600 GeV in the $H \rightarrow ZZ \rightarrow llqq$ decay channel*, submitted to Phys. Lett. **B** (2012) , arXiv:1206.2443 [hep-ex].
- [136] ATLAS Collaboration, *Observation of an excess of events in the search for the Standard Model Higgs boson in the gamma-gamma channel with the ATLAS detector*, ATLAS-CONF-2012-091 (Jul, 2012) .
<http://cdsweb.cern.ch/record/1460410>.
- [137] ATLAS Collaboration, *Search for the Standard Model Higgs boson in the $H \rightarrow WW^{(*)} \rightarrow \ell\nu\ell\nu$ decay mode with 4.7 fb^{-1} of ATLAS data at $\sqrt{s} = 7 \text{ TeV}$* , Phys. Lett. **B** **716** (2012) 62, arXiv:1206.0756 [hep-ex].
- [138] ATLAS Collaboration, *Search for the Higgs boson in the $H \rightarrow WW \rightarrow \ell\nu jj$ decay channel at $\sqrt{s} = 7 \text{ TeV}$ with the ATLAS detector*, submitted to Phys. Lett. **B** (2012) , arXiv:1206.6074 [hep-ex].
- [139] ATLAS Collaboration, *Search for the Standard Model Higgs boson in the $H \rightarrow \tau^+\tau^-$ decay mode in $\sqrt{s} = 7 \text{ TeV}$ pp collisions with ATLAS*, JHEP **09** (2012) 079.
- [140] ATLAS Collaboration, *Search for the Standard Model Higgs boson produced in association with a vector boson and decaying to a b-quark pair with the ATLAS detector*, submitted to Phys. Lett. **B** (2012) , arXiv:1207.0210 [hep-ex].
- [141] ATLAS Collaboration, *Observation of an Excess of Events in the Search for the Standard Model Higgs Boson in the $H \rightarrow WW^{(*)} \rightarrow \ell\nu\ell\nu$ Channel with*

- the ATLAS Detector*, ATLAS-CONF-2012-098 (Jul, 2012) .
<http://cdsweb.cern.ch/record/1462530>.
- [142] ATLAS Collaboration, *Luminosity Determination in pp Collisions at $\sqrt{s} = 7 \text{ TeV}$ using the ATLAS Detector in 2011*, ATLAS-CONF-2011-116 (2011) . <http://cdsweb.cern.ch/record/1376384>.
- [143] ATLAS Collaboration, *Improved luminosity determination in pp collisions at $\sqrt{s} = 7 \text{ TeV}$ using the ATLAS detector at the LHC*, arXiv:1302.4393 [hep-ex].
- [144] M. Leadbetter, *On Crossings of Levels and Curves by a Wide Class of Stochastic Processes*, Ann. Math. Statist. **37** (1965) no. 1, 260.
- [145] F. Feroz and M. Hobson, *Multimodal nested sampling: an efficient and robust alternative to MCMC methods for astronomical data analysis*, Mon.Not.Roy.Astron.Soc. **384** (2008) 449, arXiv:0704.3704 [astro-ph].
- [146] F. Feroz, M. Hobson, and M. Bridges, *MultiNest: an efficient and robust Bayesian inference tool for cosmology and particle physics*, Mon.Not.Roy.Astron.Soc. **398** (2009) 1601–1614, arXiv:0809.3437 [astro-ph].
- [147] ATLAS Collaboration, *An update of combined measurements of the new Higgs-like boson with high mass resolution channels*, ATLAS-CONF-2012-170, ATLAS-COM-CONF-2012-206 (2012) .
- [148] ATLAS Collaboration, *Combined measurements of the mass and signal strength of the Higgs-like boson with the ATLAS detector using up to 25*

- fb^{-1} of proton-proton collision data, ATLAS-CONF-2013-014,
 ATLAS-COM-CONF-2013-025 (2013) .
- [149] HSG7 group, *Higgs boson coupling and mass measurements from combination of all decay channels*, ATL-COM-PHYS-2013-187 (Feb, 2013) .
- [150] *Updated coupling measurements of the Higgs boson with the ATLAS detector using up to 25 fb^{-1} of proton-proton collision data*, Tech. Rep. ATLAS-CONF-2014-009, CERN, Geneva, Mar, 2014.
- [151] ATLAS Collaboration, *Coupling properties of the new Higgs-like boson observed with the ATLAS detector at the LHC*, ATLAS-CONF-2012-127, ATLAS-COM-CONF-2012-161 (2012) .
- [152] HSG7, *Updated coupling measurements of the Higgs boson with the ATLAS detector using up to 25/fb of proton-proton collision data*, Tech. Rep. ATL-COM-PHYS-2013-1576, CERN, Geneva, Nov, 2013.
- [153] ATLAS Collaboration, G. Aad et al., *Evidence for the spin-0 nature of the Higgs boson using ATLAS data*, Phys.Lett. **B726** (2013) 120–144, arXiv:1307.1432 [hep-ex].
- [154] ATLAS Collaboration, *Combined coupling measurements of the Higgs-like boson with the ATLAS detector using up to 25 fb^{-1} of proton-proton collision data*, .
- [155] HSG7, T. Adye, A. Armbruster, F. Cerutti, K. Cranmer, M. Duehrssen-Debling, E. Feng, H. Ji, and S. Kreiss, *Details for the coupling properties determination for the excess at 126 GeV with the*

ATLAS detector at the LHC, Tech. Rep. ATL-COM-PHYS-2012-1279, CERN, Geneva, Aug, 2012.

- [156] ATLAS Collaboration, *Updated coupling measurements of the Higgs boson with the ATLAS detector using up to 25 fb^{-1} of proton-proton collision data*, Tech. Rep. ATLAS-COM-CONF-2014-013, CERN, Geneva, Mar, 2014.
- [157] M. Duehrssen, E. Feng, S. Gadatsch, H. Ji, S. Kreiss, B. Mansoulie, H. Yang, and F. Zhang, *Higgs Boson Coupling Measurements from the Combination of All Decay Channels*, Tech. Rep. ATL-COM-PHYS-2014-092, CERN, Geneva, Feb, 2014.
- [158] HSG7, *Higgs boson coupling and mass measurements from combination of all decay channels: nuisance parameter cross-checks*, Tech. Rep. ATL-COM-PHYS-2013-617, CERN, Geneva, May, 2013.
- [159] T. Adye, N. Berger, L. Castillo, M. Duehrssen, E. Feng, F. Gianotti, H. Gray, H. Ji, S. Kreiss, C. Mills, and T. Vickey, *Measurements of Higgs boson production and couplings with the ATLAS detector at the LHC*, Tech. Rep. ATL-COM-PHYS-2013-607, CERN, Geneva, May, 2013.
- [160] ATLAS Collaboration, *Measurements of Higgs boson production and couplings in diboson final states with the ATLAS detector at the LHC*, Phys. Lett. **B** **726** (2013) 88–119, arXiv:1307.1427 [hep-ex].
- [161] ATLAS Collaboration, *Search for the $b\bar{b}$ decay of the Standard Model Higgs boson in associated W/ZH production with the ATLAS detector*, ATLAS-CONF-2013-079 (2013) .

- [162] ATLAS Collaboration, *Evidence for Higgs Boson Decays to the $\tau^+\tau^-$ Final State with the ATLAS Detector*, ATLAS-CONF-2013-108 (2013) .
- [163] LHC Higgs Cross Section Working Group, S. Heinemeyer, C. Mariotti, G. Passarino, and R. Tanaka (Eds.), *Handbook of LHC Higgs Cross Sections: 3. Higgs Properties*, arXiv:1307.1347 [hep-ph].
- [164] K. Cranmer, S. Kreiss, D. Lopez-Val, and T. Plehn, *A Novel Approach to Higgs Coupling Measurements*, arXiv:1401.0080 [hep-ph].
- [165] L. Lyons, D. Gibaut, and P. Clifford, *How to combine correlated estimates of a single physical quantity*, Nuclear Instruments and Methods in Physics Research Section A: Accelerators, Spectrometers, Detectors and Associated Equipment **270** (1988) no. 1, 110 – 117.
- [166] A. Valassi, *Combining correlated measurements of several different physical quantities*, Nuclear Instruments and Methods in Physics Research Section A: Accelerators, Spectrometers, Detectors and Associated Equipment **500** (2003) no. 13, 391 – 405.